THE CONTRIBUTIONS OF DYNAMICAL AND DIABATIC PROCESSES PRECEDING AND ACCOMPANYING MAJOR GREENLAND ICE-MELT EVENTS

By

Scott W. Feldman

A Thesis

Submitted to the University at Albany, State University of New York

In Partial Fulfillment of

The Requirements for the Degree of

Master of Science

College of Arts & Sciences

Department of Atmospheric and Environmental Sciences

December 2021

ABSTRACT

Extratropical cyclones and/or short-wave disturbances can reinforce Greenland blocking through upper-level flow amplification and can increase poleward heat and moisture transport into the Arctic. Increased poleward heat and moisture transport into the Arctic may enhance Greenland ice melt during the spring, summer, and fall months. The need to better understand the underlying dynamical and diabatic processes that may contribute to Greenland ice melt motivates this thesis. The purpose of this thesis is to investigate: 1) the role of advective warming due to poleward heat and moisture transport into the Arctic in facilitating Greenland ice melt, 2) the role of adiabatic warming due to synoptic-scale descent associated with Greenland blocking in facilitating ice melt, and 3) the role of diabatic warming due to condensation and latent heating over Greenland in facilitating ice melt. Self-organizing maps (SOMs) are utilized to construct a synoptic climatology of Greenland ice-melt events during the April–October 1979–2019 time period. The SOMs identify three main types of synoptic-scale flow patterns during Greenland ice-melt events: 1) a blocking pattern over Greenland, 2) a positively tilted trough upstream of Greenland, and 3) a high-amplitude negatively tilted trough upstream of Greenland.

During late July–early August 2019, 60% (i.e., ~984,000 km^2) of the Greenland ice sheet experienced melting, which is the largest ice melt event over Greenland since at least 2012. Ice melt over Greenland was associated with a blocking anticyclone over Scandinavia that subsequently shifted westward toward Greenland and permitted anomalously warm air of Saharan origin to reach Greenland. Upper-level flow amplification from eastern North America to western Europe resulted in ridge amplification over northwest Africa, which occurred in conjunction with the formation of an atmospheric river (AR) over the North Atlantic Ocean that was associated with a large poleward-directed moisture transport. Anomalously warm air of Saharan origin reached western Europe and Scandinavia, resulting in a record-breaking heat wave as the ridge over northwest Africa extended poleward and subsequently evolved into the blocking anticyclone over Scandinavia. The AR subsequently transitioned into a westward-directed moisture transport toward Greenland in conjunction with a westward shift of the blocking anticyclone over Scandinavia toward Greenland.

Air parcel trajectories were computed to analyze the modifications of the air masses that contributed to the late July–early August 2019 ice-melt event and to identify their origins. Air parcels initialized in the AR over the North Atlantic Ocean at 1200 UTC 25 July 2019 first moved poleward in conjunction with the poleward extension of the ridge over northwest Africa toward Scandinavia and then moved westward toward Greenland in conjunction with the westward shift of the blocking anticyclone over Scandinavia toward Greenland. Moist ascending air parcels initialized in the AR over the North Atlantic Ocean experienced a median specific humidity decrease from ~8 g kg^{-1} to ~1 g kg^{-1} and a median potential temperature increase from ~298 K to ~315 K as these air parcels ascended from ~850 hPa to ~480 hPa during the 72-h period ending on 1200 UTC 28 July 2019. These respective changes in median specific humidity and median potential temperature are indicative of condensation and latent heat release over Greenland, such that the associated diabatic warming may have contributed to Greenland ice melt during this event.

ACKNOWLEDGEMENTS

I would like to thank my co-advisors, Drs. Lance Bosart and Dan Keyser, for their endless mentorship, support, and patience during my graduate student experience at UAlbany. They are both remarkable scientists that have made major contributions to our field for decades. I appreciate that they have taken the time in their retirement from teaching to continue to mentor myself and other graduate students. Lance and Dan have both challenged me at every turn regarding my research, which has made me a better scientist and communicator. I also greatly appreciate the opportunities they gave me to travel and present at numerous conferences. I look forward in continuing to work with them on submitting my Master's thesis work for publication in the coming months.

I would also like to thank all of the faculty members and colleagues I have had the privilege to work with in the Department of Atmospheric and Environmental Sciences at UAlbany. A special thanks to Barbara Zampella, Carolyn DeLuise, and Chaina Porter for their administrative support and being so helpful with all the questions I had over these past few years. I would also like to thank Kevin Tyle for all of the computing support you do for our department, which was vital for this thesis. A special thanks to Drs. Brian Rose, Liming Zhou, Rob Fovell, Andrea Lang, and Ryan Torn for teaching graduate-level courses that were vital for my research and growth as an atmospheric scientist. I would also like to thank Drs. Vincent Idone and Junhong Wang, and Ross Lazear for being a pleasure to work with as a teaching assistant for their classes.

I would like to thank all of my fellow graduate students that I have worked with and had the pleasure to become friends with over the past few years. A special thanks to Matthew Jenkins, Alejandro Ayala, Brennan Stutsrim, Adam Sisco, Matthew Seymour, Kevin Biernat, Tyler Leicht, Alex Tomoff, and Alex Mitchell for all of the research/programming help you provided, but most importantly for making my graduate school experience enjoyable. I hope we can continue our friendship into the future. A special thanks to Adam Sisco from UAlbany for helping me utilize self-organizing maps in my research, and Mauro Hermann from ETH Zurich for assisting me in running air parcel trajectories and providing me sample code for data processing and visualization of those trajectories.

A special thanks to my family, long-time friends, and girlfriend for supporting me every step of the way. Despite being a long distance away from each other, they were always available to give me encouragement and empathize with me during challenging times. Being a graduate student, especially during the COVID-19 pandemic, was not always easy so I really appreciate them always being there for me.

This research was supported by the Office of Naval Research (ONR) grant N00014-18-1-2200, awarded to the University at Albany, SUNY.

Scott Feldman

Albany, NY

December 2021

TABLE OF CONTENTS

LIST OF FIGURES

m^{-1} s^{-1}; shaded) are overlaid and are valid at 1200 UTC 25 July. (b) As in (a), except the 10-d forward air parcel trajectories are initialized north of the AR and the jet core at 500 hPa.

FIG. 4.12. Time series of (a) pressure (hPa), (b) potential temperature (K), and specific humidity (g kg^{-1}) for the 10-d forward air parcel trajectories for the North Atlantic Ocean domain initialized at 925, 850, and 700 hPa and at 1200 UTC 25 July 2019. The red lines represent the median of each variable for the forward air parcel trajectories initialized over the AR and south of the jet core at 500 hPa from Fig. 4.11a, and the black lines represent the median of each variable for the forward air parcel trajectories initialized north of the AR and the jet core at 500 hPa from Fig. 4.11b. The black and red dots represent the median of each variable for the forward air parcel trajectories at 12-h intervals. The red shading indicates the interquartile range of each variable for the forward air parcel trajectories over the AR and south of the jet core at 500 hPa, and the gray shading indicates the interquartile range of each variable for the forward air parcel trajectories initialized north of the AR and the jet core at 500 hPa.

FIG. 4.13. 10-d backward air parcel trajectories (light black lines) for the Greenland domain initialized at 925, 850, 700, 600, and 500 hPa and at 1800 UTC 31 July 2019. Backward air parcel trajectories of interest are initialized at 1800 UTC 31 July 2019 and originate from Alaska (black line and circles), Quebec (blue line and triangles), the eastern North Atlantic Ocean (red line and squares), and northwest Africa (green line and squares), respectively. Each symbol (i.e., circle, square, triangle) delineates the backward air parcel trajectories of interest at 12-h intervals.

FIG. 4.14. Time series of (a) pressure (hPa), (b) potential temperature (K), and equivalent potential temperature (K) for the 10-d backward air parcel trajectories of interest from Fig. 4.13 for the Greenland domain initialized at 1800 UTC 31 July 2019. The black lines represent the backward air parcel trajectory originating from Alaska, the blue lines represent the backward air parcel trajectory originating from Quebec, the red lines represent the backward air parcel trajectory originating from the eastern North Atlantic Ocean, and the green lines represent the backward air parcel trajectory originating from northwest Africa. Each symbol (i.e., circle, square, triangle) delineates the backward parcel trajectories of interest at 12-h intervals.

FIG. 4.15. The sum of the (a) adiabatic temperature change (°C), (b) diabatic temperature change (°C), and (c) temperature change (°C) for every backward air parcel trajectory arriving every 6 h over 2 d at 700 hPa over the Greenland domain during 0000 UTC 28–1800 UTC 29 July 2019. Summit Station and the South Dome are denoted by large and small triangles, respectively. Panels (d), (e), and (f) are the same as (a), (b), and (c) except during 0000 UTC 30–1800 UTC 31 July 2019.

1. Introduction

1.1 Motivation

The Earth's rapidly changing climate is resulting in significant changes to the Greenland ice sheet. The Greenland ice sheet is losing mass at an accelerating rate (e.g., Mote 2007; Rignot et al. 2011; Seo et al. 2015). Seo et al. (2015) used Earth gravity satellites and regional climate model data to show that the acceleration rate of Greenland ice mass loss from 2003 to 2012 was -13.9 ± 2.0 Gt yr^{-2}, and the mean ice discharge from 2003 to 2012 was 587.5 ± 30.8 Gt yr^{-1}. Sasgen et al. (2020) used satellite data to determine that Greenland set a new record for ice loss in 2019, in which 532 billion tons of ice melted. The areal coverage of ice melt has expanded to higher elevations of the Greenland ice sheet during the summer months (e.g., Mote 2007; Fitzpatrick et al. 2014). The Greenland ice-melt season has lengthened by more than a month over lower elevations of the Greenland ice sheet since the early 1970s (e.g., Mernild et al. 2017).

The melting of the Greenland ice sheet, glacial ice, and small ice caps along the coastal regions of Greenland is a major contributor to sea level rise. Van den Broeke et al. (2016) found that the Greenland ice sheet had an average annual mass loss of $\sim 0.47 \pm 0.23$ mm sea level equivalent during the 1991–2015 period and a maximum sea level equivalent of 1.2 mm in 2012. Price et al. (2011) estimated a maximum of 45 mm of sea level rise from Greenland ice sheet dynamics by 2100. Approximately 40% of the global population lives along coastal areas that may be susceptible to societal impacts from sea level rise. The societal impacts from sea level rise may include an increased risk of flooding, shoreline erosion, damage to infrastructure, and stress on coastal ecosystems.

Changes in the large-scale atmospheric circulation over Greenland may be becoming more conducive to Greenland ice melt. Increased poleward moisture transport has played a major role in record Greenland ice melt in recent years (e.g., Neff et al. 2014; Mattingly et al. 2016). Large poleward moisture transport may facilitate Greenland ice melt through the formation of clouds in regions of midtropospheric ascent that may increase downwelling longwave radiation (e.g., Mattingly et al. 2016). Strong blocking patterns over Greenland may be becoming more frequent (e.g., Fettweis et al. 2011, 2013; Overland et al. 2012). These strong blocking patterns over Greenland facilitate Greenland ice melt through large-scale subsidence that is often

associated with clear skies and anomalously warm temperatures. A blocking pattern with a ridge axis centered to the east of Greenland may also facilitate Greenland ice melt due to a mild and moist southeasterly flow across the Greenland ice sheet.

The need to better understand the mechanisms for the underlying dynamical and diabatic processes that may contribute to Greenland ice melt motivates this research. In this study, we investigate the role of poleward moisture transport and warm-air advection (WAA) into the Arctic on Greenland blocking and the formation of warm anomalies over Greenland. We also investigate the role of strong cyclones that track poleward and west of Greenland and that transport anomalously warm and moist air on their eastern sides toward Greenland. Sprenger et al. (2017) constructed a climatology of Arctic cyclones (ACs), and El Riachy (2021) adapted this climatology to identify four corridors of high track frequencies (i.e., Pacific, West of Greenland, Atlantic, and Asian). The West of Greenland track is likely to lead to the most rapid Greenland ice melt because warm and moist air on the eastern sides of these cyclones along this track is typically directed toward Greenland. Case studies of events with poleward-moving cyclones located in the West of Greenland sector identified by El Riachy (2021) are needed to better understand the synoptic-dynamic linkages between ACs and Greenland ice-melt events. Lastly, we investigate the role of adiabatic warming due to large-scale subsidence associated with Greenland blocking and the role of diabatic heating due to latent heating resulting from the condensation of water vapor.

1.2 Literature Review

1.2.1 Climatology of Greenland Ice-Melt Events

Previous studies have constructed climatologies of the synoptic flow patterns that may be conducive to Greenland ice melt (e.g., Mote 1998; Fettweis et al. 2011, 2013; Mattingly et al. 2016; Mioduszewski et al. 2016). Mote (1998) extracted nine common synoptic flow patterns over Greenland by performing cluster analysis of daily 700-hPa geopotential height from May 1979 to June 1989 (not shown). These nine common synoptic flow patterns show patterns that are both favorable and unfavorable for Greenland ice melt. Synoptic flow patterns that produce

southwesterly onshore flow along the west coast of Greenland are associated with higher spatial extent of ice melt in the northern and eastern regions of Greenland. The strength and location of a North American trough and a North Atlantic trough have major impacts on the synoptic flow patterns over Greenland, and thus the extent of Greenland ice melt. The North American trough, the axis of which is located west of Greenland, is associated with increased ice melting, while the North Atlantic trough, the axis of which is located over or east of Greenland, is associated with reduced ice melting. The North American trough is associated with increased ice melting due to WAA over Greenland, while the North Atlantic trough is associated with reduced ice melting due to cold air- advection over Greenland.

Fettweis et al. (2011, 2013) utilized an automatic circulation type classification (CTC) based on 500-hPa geopotential height (obtained from ERA-40 and NCEP–NCAR reanalysis for the 1958–2009 period) in order to assess the impact of midtropospheric circulations on Greenland ice melt. Record Greenland ice-melt events are linked to the exceptional persistence of atmospheric circulations favoring WAA over Greenland. The CTC revealed that the frequency of summer 500-hPa anticyclones over Greenland has doubled since the end of the 1990, which is partially responsible for the recent warming over Greenland and thus increases in Greenland ice melt.

Mioduszewski et al. (2016) identified synoptic flow anomaly patterns conducive to Greenland ice melt by creating an Arctic synoptic climatology of 500-hPa geopotential height anomalies (obtained from MERRA reanalysis data for the 1979–2014 period) using self-organizing maps (SOMs) (Kohonen 1995, 106–109). Positive 500-hPa geopotential height anomalies near Greenland (Fig. 1.1), associated with strong meridional transport of heat and moisture coincide with the largest positive ice-melt anomalies near Greenland (Fig. 1.2). The opposite is true for negative ice-melt anomalies, which largely occur in conjunction with negative 500-hPa geopotential height anomalies over Greenland and Baffin Bay. Examples of characteristic synoptic flow anomaly and melt patterns identified in Figs. 1.1 and 1.2 are as follows: (i.) node (1,3) shows positive 500-hPa geopotential height anomalies over Greenland (Fig. 1.1), which coincide with large positive ice-melt anomalies over western Greenland (Fig. 1.2); (ii.) node (6,4) shows negative 500-hPa geopotential height anomalies west of and over Greenland (Fig. 1.1), which coincide with weak negative ice-melt anomalies over southern

Greenland (Fig. 1.2); and (iii.) node (2,5) shows positive 500-hPa geopotential height anomalies north of Greenland (Fig. 1.1), which coincide with weak positive ice-melt anomalies over western and southern Greenland (Fig. 1.2). The SOM node frequency and trends analysis shows that ridging over Greenland is becoming more frequent, which coincides with an increase in Greenland ice melt, with 75% of ice melt attributed to thermodynamics, 17% to dynamics, and 8% to a combination of thermodynamics and dynamics.

Mattingly et al. (2016) used SOMs to classify integrated water vapor transport (IVT) data from the ERA-Interim reanalysis to determine if increases in Greenland ice melt are linked to increases in moisture transport to Greenland between the 1979–1994 and 2000–2015 periods. The common pathways for moisture transport into the Arctic are identified from a 5 × 4 SOM (Fig. 1.3). Nodes 1 and 3 have strong IVT over Greenland, where node 1 has IVT along the west coast of Greenland, while node 3 has IVT along the east coast of Greenland. Node 5 is the most frequently occurring node, with strong moisture transport from the Greenland Sea into the Arctic Ocean. The IVT patterns shown in nodes 1 and 5 (Fig. 1.3) are statistically significantly more common during 2000–2015 compared to 1979–1994 at the 95% confidence level (Fig. 1.4).

The location of high IVT over Greenland may be directly related to the location of the negative 500-hPa geopotential height anomalies with respect to Greenland and the sign of the ice-melt anomalies over Greenland. High IVT that is located over the west coast of Greenland (e.g., node 1) (Fig. 1.3) is associated with negative 500-hPa geopotential height anomalies west of Greenland (e.g., node (3,5)) (Fig. 1.1) and weak positive ice-melt anomalies over Greenland (e.g., node (3,5)) (Fig. 1.2). High IVT that is located over the east coast of Greenland (e.g., node 3) (Fig. 1.3) is associated with negative 500-hPa geopotential height anomalies directly over or east of Greenland (e.g., node (6,1)) (Fig. 1.1) and weak-to-moderate negative ice-melt anomalies over Greenland (e.g., node (6,1)) (Fig. 1.2).

1.2.2 Greenland Blocking and Poleward Transport from Lower Latitudes into the Arctic

There are various physical and dynamical processes and mechanisms that may contribute to Greenland blocking and the transport of warm, moist air from lower latitudes poleward into

the Arctic. Greenland blocking may be generated by Rossby wave breaking (RWB), which may result in the poleward advection of warm, moist air (e.g., Liu and Barnes 2015; Baggett et al. 2016). Liu and Barnes (2015) composited atmospheric variables for extreme transient poleward moisture transport (Fig. 1.5). Extreme transient poleward moisture transport southwest of Greenland is associated with cyclonic wave breaking (CWB) over the northwest Atlantic and Davis Strait (Fig. 1.5a). Extreme transient poleward moisture transport over the Norwegian Sea is associated with anticyclonic wave breaking (AWB) over the northeast Atlantic and Greenland Sea (Fig. 1.5b). CWB-related moisture transport is most frequent in late autumn and least frequent in early summer, while AWB-related moisture transport is most frequent in early autumn and least frequent in spring. RWB occurrence is closely linked to the latitude of the midlatitude jet, where AWB tends to occur more frequently in association with a poleward-shifted midlatitude jet, while CWB tends to occur more frequently in association with an equatorward-shifted midlatitude jet (Rivière 2011; Barnes and Hartmann 2012). There tends to be a poleward-shifted midlatitude jet in autumn, while there tends to be a slightly equatorward-shifted midlatitude jet in early summer [Fig. 8 from Liu and Barnes (2015)] (not shown). AWB tends to occur on the anticyclonically sheared flank corresponding to the equatorward region of the jet, while CWB tends to occur on the cyclonically sheared flank corresponding to the poleward region of the jet (e.g., Thorncroft et al. 1993; Peters and Waugh 1996).

The IVT patterns shown in Fig. 1.3 may be directly related to the type of RWB (i.e., CWB or AWB) near Greenland. Nodes 1–3 and 6–7 in Fig. 1.3 may be associated with CWB since there is large poleward moisture transport over southwest Greenland. Nodes 4–5 and 8–10 in Fig. 1.3 may be associated with AWB since there is large poleward moisture transport over the Norwegian Sea.

Greenland blocking can displace the polar jet stream equatorward and may enable extratropical cyclones and/or short-wave disturbances to move toward higher latitudes (e.g., Overland et al. 2015). Precursor extratropical cyclones and/or short-wave disturbances can further intensify Greenland blocking through upper-level flow amplification and enhance advection of warm, moist air into the Arctic (e.g., McLeod and Mote 2015). McLeod and Mote (2015) composited extreme Greenland blocking events (GBEs) that do and do not occur in conjunction with a precursor cyclone, or precursor cyclones, in order to investigate whether a

precursor cyclone, or precursor cyclones can lead to downstream upper-level flow amplification (Fig. 1.6). Only extreme GBEs that occur during the extended summer season (i.e., May through September) are considered in order to lessen the effect of the seasonal cycle in 500-hPa geopotential height over the North Atlantic region. Extreme GBEs that occur in conjunction with a precursor cyclone, or precursor cyclones produce a 500-hPa geopotential height pattern that resembles an omega block (Fig. 1.6a), while extreme GBEs without a precursor cyclone, or precursor cyclones produce a 500-hPa geopotential height pattern that resembles a Rex block (Fig. 1.6b). The 500-hPa geopotential height values for extreme GBEs that occur in conjunction with a precursor cyclone, or precursor cyclones are greater (60–120 m) over the North Atlantic Ocean and northwest of Greenland, and lower (0–40 m) over eastern Canada and southeast of Greenland (Fig. 1.6c).

Advection of warm, moist air into the Arctic may be associated with Greenland blocking since upstream latent heating may help establish and maintain negative potential vorticity (PV) anomalies in the upper troposphere (e.g., Zschenderlein et al. 2020). Zschenderlein et al. (2020) analyzed the contribution of latent heating to the formation and persistence of upper-tropospheric anticyclones associated with heat waves in different parts of Europe by identifying three airstreams that contribute to the formation and persistence of upper-tropospheric anticyclones using backward air parcel trajectory analysis. Approximately 25–45% of the airstreams that originate off the coast of northwest Africa and over the North Atlantic are diabatically heated (i.e., the change in potential temperature with time along the airstreams is positive) during the 3 days prior to their arrival in upper-tropospheric anticyclones (Fig. 1.7). The aforementioned diabatically heated airstreams experience a positive change in potential temperature ranging from just above 0°C to as high as 40°C [Fig. 5 of Zschenderlein et al. (2020)] (not shown). Zschenderlein et al. (2020) inferred that extratropical cyclone activity and warm conveyor belts in the North Atlantic associated with latent heat release is important to the formation and persistence of upper-tropospheric anticyclones. Zschenderlein et al. (2020) concluded that longer-lasting heat waves often cannot be sustained without the transport of low-PV air to the upper troposphere within extratropical cyclones.

Poleward transport of warmer air masses from lower latitudes can result in lower-tropospheric warm anomalies in the Arctic (e.g., Hermann et al. 2020; Papritz 2020). Papritz

(2020) found that, for approximately 60% of air masses in the winter and 90% of air masses in the summer, the formation of warm anomalies in the Arctic is dominated by the vertical and horizontal transport of air parcels from regions with a higher climatological potential temperature [Fig. 3 from Papritz (2020)] (not shown). Adiabatic warming associated with midtropospheric subsidence has been shown to help sustain lower-tropospheric warm anomalies in the Arctic (e.g., Ding et al. 2017; Papritz 2020). Climatological summer adiabatic temperature changes (i.e., the average adiabatic temperature change of all air parcel trajectories during JJA 1979–2017) over Greenland are strongly dependent on elevation (Hermann et al. 2020). Climatological summer air masses over Greenland start at a median initial temperature of ~−3.8°C (Fig. 1.8a). Climatological summer air masses that reach central Greenland tend to ascend and cool adiabatically, while climatological summer air masses that reach coastal Greenland tend to descend and warm adiabatically (Fig. 1.8b). The descent of climatological summer air masses that reach coastal Greenland may be due to katabatic drainage flows that are prevalent over the Greenland ice sheet (e.g., Heinemann and Klein 2002).

Large poleward moisture transport into the Arctic can enhance Greenland ice melt through diabatic processes. Climatological summer air masses that reach Greenland experience diabatic cooling of ~0.5–1°C d^{-1} (Fig. 1.8c) due to outgoing longwave radiation (Hermann et al. 2020). Diabatic cooling is dominant at higher elevations of Greenland, while adiabatic warming compensates for much of the radiative cooling at lower elevations (Fig. 1.8d). Air masses that reach Greenland prior to and during summer Greenland ice-melt events may experience enhanced diabatic heating compared to climatological summer air masses [Fig. 11 from Hermann et al. (2020)] (not shown). Diabatic heating may be enhanced during Greenland ice-melt events that are associated with large poleward moisture transport since latent heat release occurs in regions of midtropospheric ascent, resulting in the formation of clouds that may increase downwelling longwave radiation (e.g., Mattingly et al. 2016). Turbulent fluxes of sensible and latent heat may also enhance Greenland ice melt through the mixing of anomalously warm and moist lower-tropospheric air downward onto the Greenland ice sheet (e.g., Neff et al. 2014; Fausto et al. 2016; Mattingly et al. 2020).

1.2.3 Early July 2012 Greenland Ice-Melt Event

The early July 2012 Greenland ice-melt event still holds the highest Greenland ice-melt extent on record, in which 1,418,000 km^2 of Greenland's area experienced ice melt on 11 July 2012 according to the National Snow and Ice Data Center (NSIDC) (https://nsidc.org/greenland-today/greenland-surface-melt-extent-interactive-chart/). Previous studies have linked the transport of anomalously warm air toward Greenland during this event to the record July 2012 North American heat wave using air parcel trajectory analysis (e.g., Neff et al. 2014; Hermann et al. 2020). Air parcel trajectory analysis shows that anomalously warm air at 925 hPa over the southern U.S. was able to reach Greenland (Figs. 1.9a,b). Air parcels at ~950 hPa over the southern U.S. at 0000 UTC 1 July had a temperature of 29°C [Table 1 of Neff et al. (2014)] (not shown). The initial temperature above Summit Station (~688 hPa elevation) at 0000 UTC 1 July was ~−13°C at 600 hPa. The air parcels over the southern U.S. reached Summit Station at 0000 UTC 11 July, with a temperature of −7°C above Summit Station at ~600 hPa. If the air parcels were lowered adiabatically to surface (i.e., ~688 hPa) they would warm to 1°C. Hermann et al. (2020) found that even though the air parcels over Greenland originated from the North American heat wave, a warm anomaly over Greenland could not be directly related to the temperature anomaly near the origin of the parcel trajectories. Latent heating due to the condensation of water vapor may have compensated for some of the adiabatic cooling associated with ascent as the air parcels moved poleward and contributed to the warm anomaly over Greenland. Air parcels over the U.S. during the heat wave had a median specific humidity of ~8 g kg^{-1} [Fig. 6 of Hermann et al. (2020)] (not shown). The median specific humidity of the air parcels decreased to ~3.5 g kg^{-1} as the air parcels ascended and moved poleward toward Greenland, which is indicative of latent heating due to the condensation of water vapor.

There was large poleward moisture transport within an atmospheric river (AR) directed toward western Greenland that preceded the peak Greenland ice melt extent that occurred on 11 July 2012 (Fig. 1.10). A deep trough over Newfoundland and a strong ridge off the coast of southeast Greenland helped facilitate the transport of warm, moist air over the Atlantic poleward toward western Greenland (Figs. 1.10a,b). For example, node (1,3) in Figs. 1.1 and 1.2 is consistent with the synoptic setup of the early July Greenland ice-melt event, since node (1,3) implies a strong ridge over Greenland in the summer months (Fig. 1.1), which coincides with

large positive Greenland ice-melt anomalies over western Greenland (Fig. 1.2). The AR directed toward western Greenland during the early July 2012 Greenland ice-melt (Fig. 1.10a) event may be associated with CWB over the western North Atlantic (Fig. 1.10b), which is consistent with the composite of extreme transient poleward moisture transport toward western Greenland in Fig. 1.5a.

1.3 Research Goals and Thesis Structure

1.3.1 Research Goals

1. Identify and analyze the synoptic flow patterns that may contribute to anomalous ice melt on daily to weekly time scales by creating a climatology of Greenland ice-melt events during 1979–2019 using SOMs.
2. Explore seasonal variations in the synoptic flow patterns that may contribute to anomalous ice melt by comparing summer and fall/spring Greenland ice-melt events using SOM node identification.
3. Improve understanding of how extratropical cyclones and/or short-wave disturbances may contribute to Greenland blocking through upper-level flow amplification and upstream latent heating using case studies.
4. Identify and analyze the source of air masses that may contribute to Greenland ice-melt events using air parcel trajectory analysis.
5. Quantify the contribution of adiabatic warming due to large-scale subsidence during Greenland ice-melt events using air parcel trajectory analysis.
6. Quantify the contribution of diabatic heating due to latent heating during Greenland ice-melt events that are characterized by high poleward moisture transport into the Arctic diagnosed using air parcel trajectory analysis.

1.3.2 Thesis organization

- Data and methodology

- Climatology
- Case studies and air parcel trajectory analysis
- Discussion, conclusions, and suggestions for future work

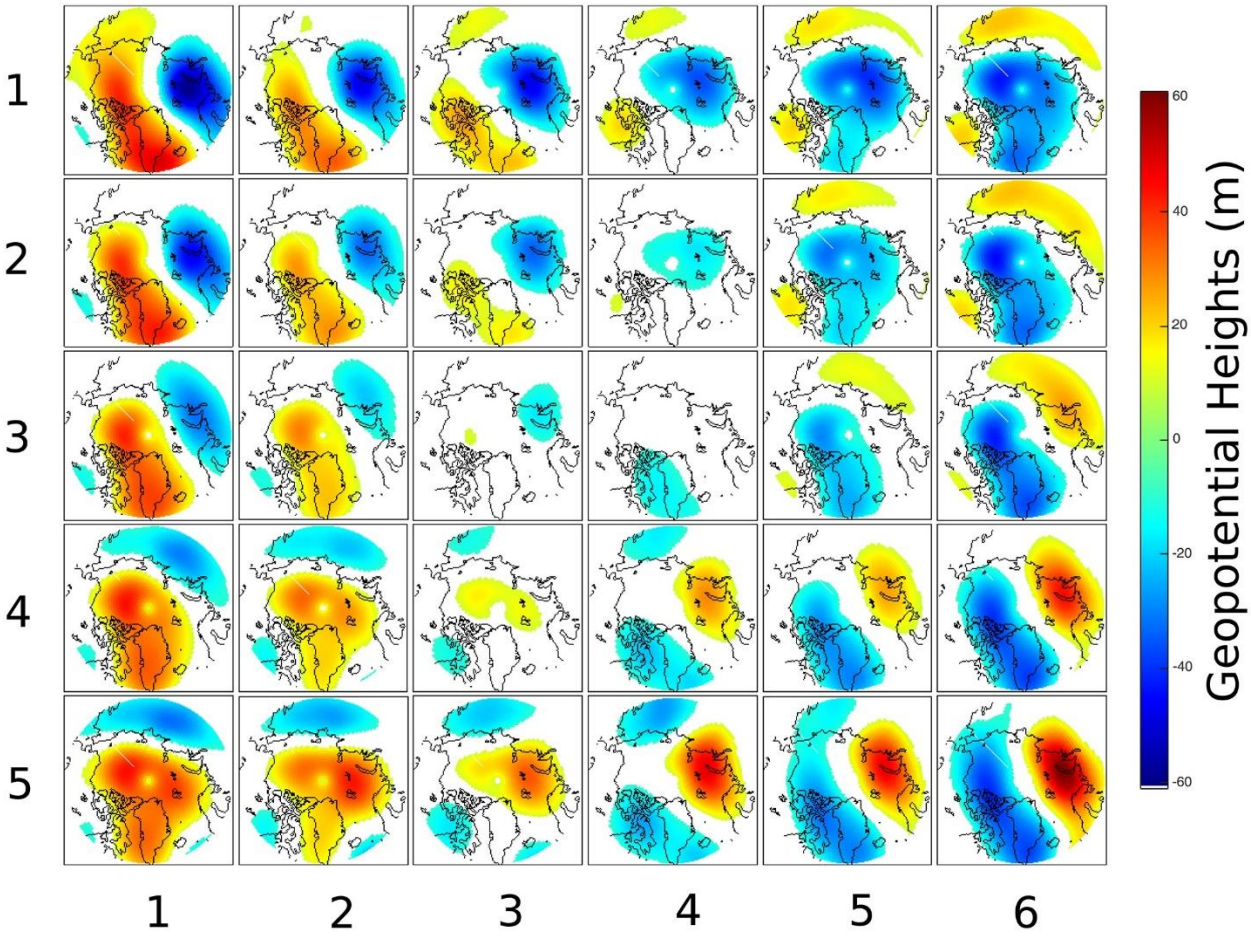

FIG. 1.1. Composite maps of daily JJA 500-hPa geopotential height anomalies for each node identified by the 6 × 5 SOM for the 1979–2014 period. [Figure 1 and adapted caption from Mioduszewski et al. (2016).]

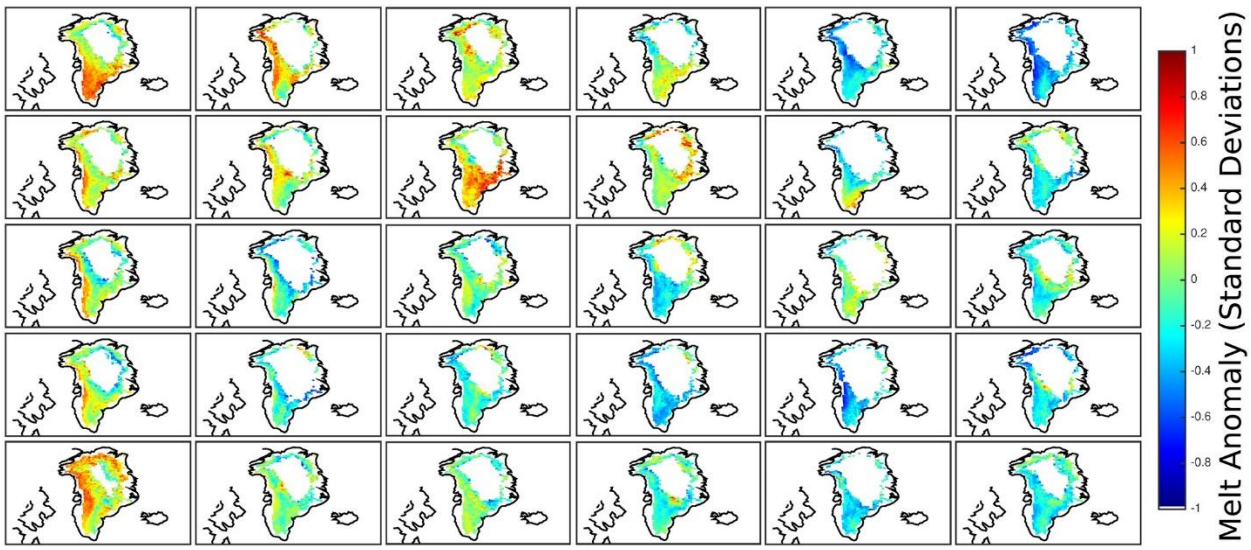

FIG. 1.2. Composite maps of daily standardized meltwater production anomalies averaged over all dates and placed into each node from Fig. 1.1. Grid cells where there are fewer than 10 nonzero melt water production values are masked. [Figure 4 and adapted caption from Mioduszewski et al. (2016).]

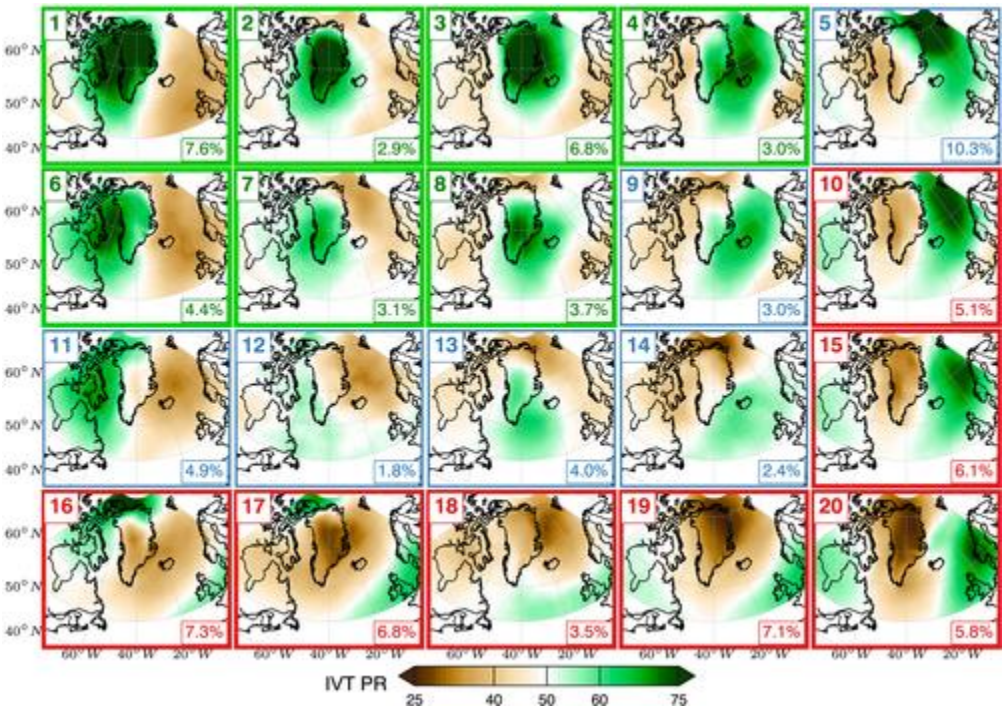

FIG. 1.3. Composite maps of daily mean IVT percentile rank for each node identified by a 5 × 4 SOM. The moist nodes are outlined in green, neutral nodes in blue, and dry nodes in red. The percentage of days during the 1979–2015 period mapped to each node is given in the bottom right-hand corner of each panel. [Figure 2 and adapted caption from Mattingly et al. (2016).]

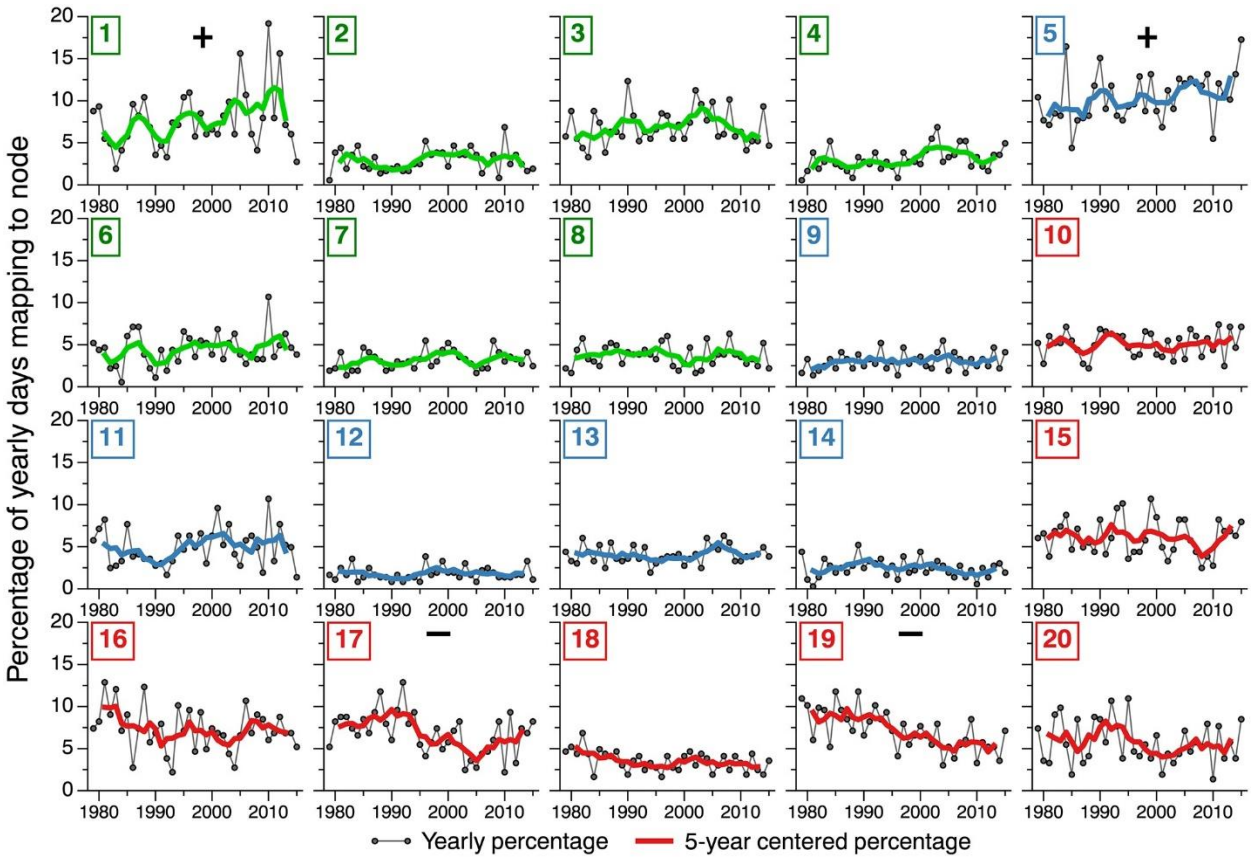

FIG. 1.4. Time series of the percentage of days in each year mapping to each SOM node. Thin gray lines show the percentage of node days for each year and thick lines show 5-year centered means. Lines are color coded according to node grouping using the same colors as in Fig. 1.3, and nodes with statistically significant increases (decreases) in frequency at the 95% confidence level during 2000–2015 relative to 1979–1994 are marked with plus (minus) symbols. [Figure 3 and caption from Mattingly et al. (2016).]

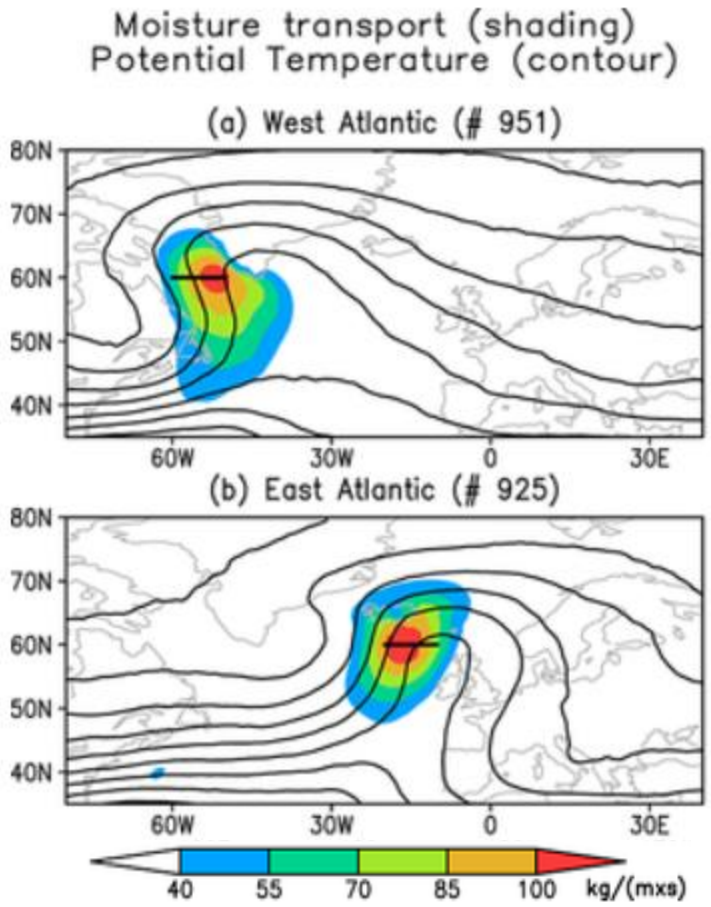

FIG. 1.5. Composite variables for extreme (greater than the 90th percentile) transient poleward moisture transport across 10° longitude bins at 60°N indicated by the black straight lines for the (a) West Atlantic (60°W–50°W), and (b) East Atlantic (20°W–10°W). The moisture transport is denoted by shading and potential temperature on the 2-PVU surface is denoted by contours. The number of 6-h time steps in each composite is denoted in the title of each panel. [Figure 4 and caption adapted from Liu and Barnes (2015).]

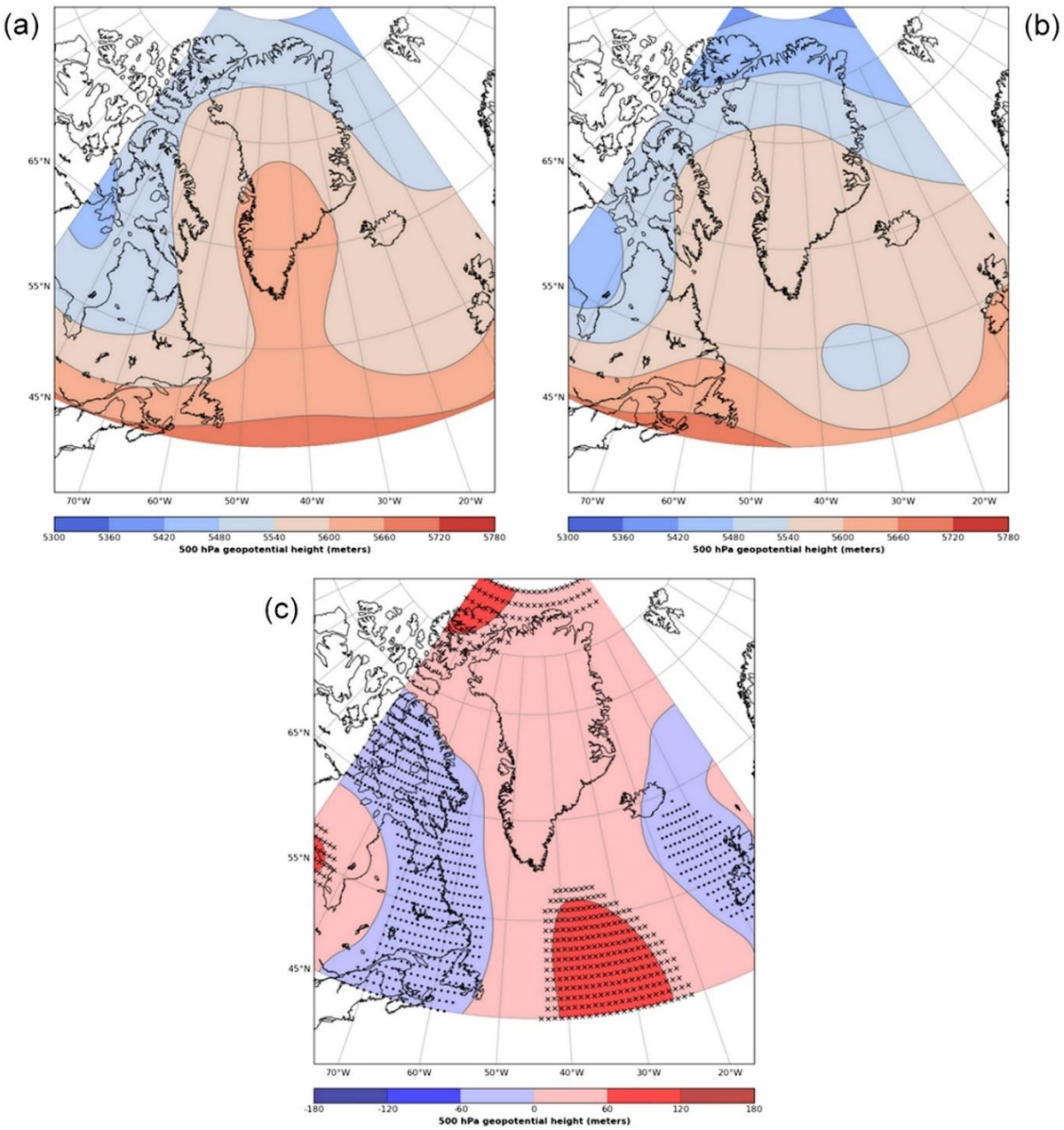

FIG. 1.6. Composite map of 500-hPa geopotential height associated with extreme GBEs (defined as a sequence of 5 consective days in which the mean 500-hPa geopotential height over the Greenland region equals or exceeds the 97th percentile compared to climatology) that (a) do and (b) do not occur in conjunction with a precursor cyclone, or precursor cyclones, during the extended summer season (i.e., May through September). A composite difference map of plots in panels (a) and (b) is shown in panel (c), with cross hatching representing 500-hPa geopotential height differences that are at least 1 standard deviation greater (less) than the sample mean. [Figure 3 and adapted caption from McLeod and Mote (2015).]

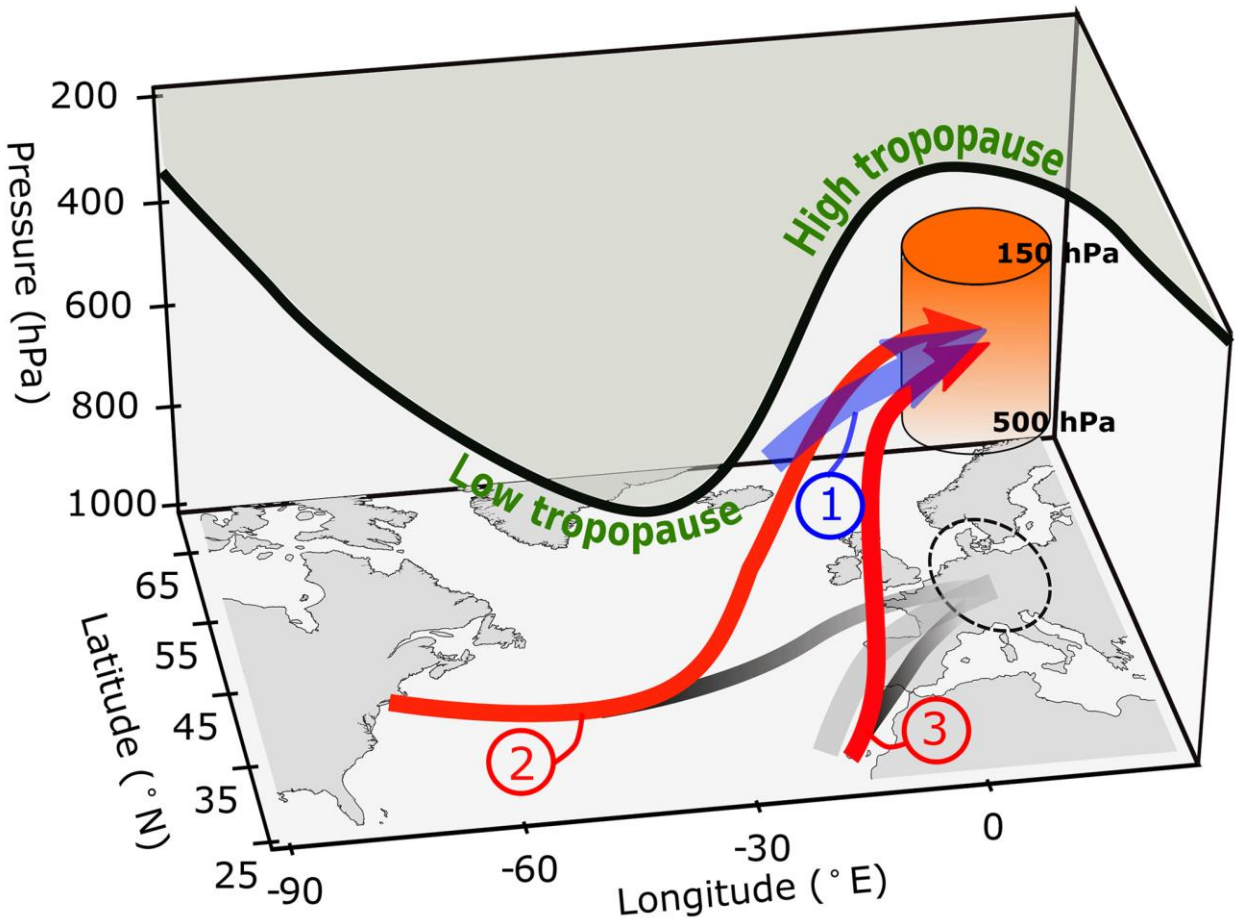

FIG. 1.7. Schematic illustrating the pathways of the three airstreams contributing to the upper-tropospheric anticyclone (red cylinder) above the heat wave in central Europe (black dashed circle) during the 3 days prior to the arrival of the airstreams. Airstream 1 denotes the cooling branch and airstreams 2 and 3 denote the North Atlantic and northwest Africa heating branches. Gray-marked lines at the surface illustrate the projections of the arrows (lighter gray indicates a higher altitude of the associated airstream). The bold black line represents the dynamic tropopause. The arrow of airstream 1 is wider because this branch is less spatially coherent compared to airstreams 2 and 3. [Figure 11 and adapted caption from Zschenderlein et al. (2020).]

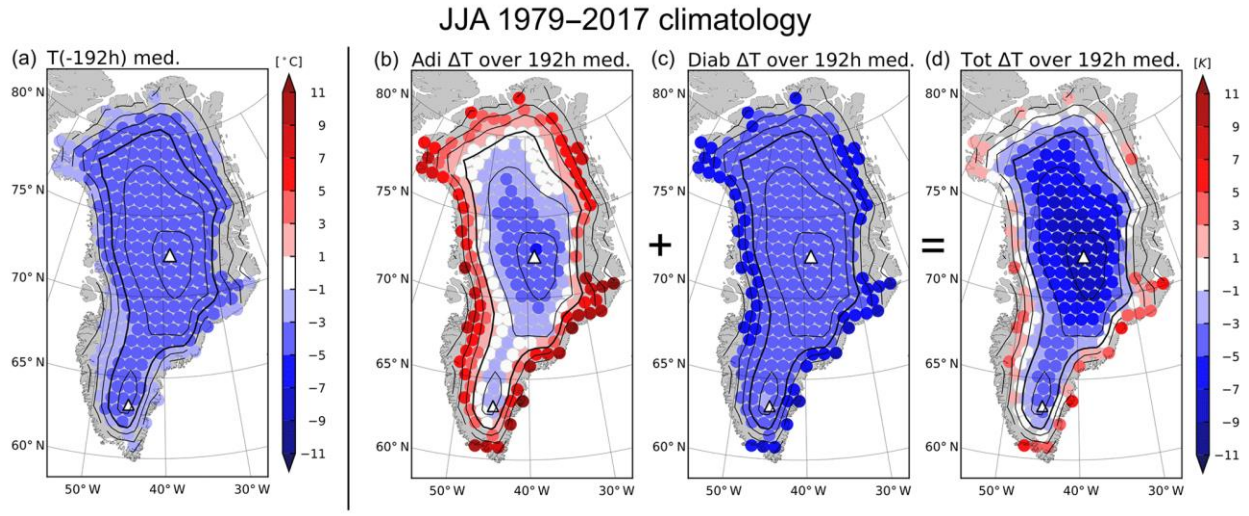

FIG. 1.8. Lagrangian forward projection scatter maps of (a) median initial temperature at t = 192 h, (b) median adiabatic, (c) median diabatic, and (d) median total temperature change over 8 days for JJA 1979–2017 climatological summer air masses. The contours indicate terrain elevation in 500 m intervals with the 2000 m isoline in bold contours. [Figure 4 and adapted caption from Hermann et al. (2020).]

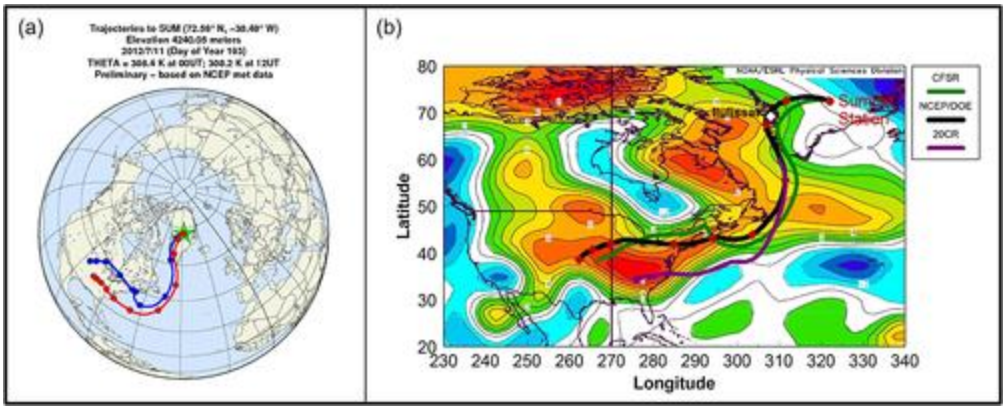

FIG. 1.9. Trajectory analysis for the 11 July 2012 Greenland ice-melt event. (a) Backward trajectories from 1 km above Summit Station for air parcels arriving over Greenland on 11 July. Trajectory paths are marked in daily increments starting from the central U.S. at 0000 UTC (blue) and 1200 UTC (red) on 1 July. (b) 925-hPa temperature anomaly (colored) over the U.S. on 1 July. 700-hPa backward trajectories are shown, and the NCEP/DOE reanalysis is in black, the CFSR is in green, and the 20CR is in purple. [Figure 1 and adapted caption from Neff et al. (2014).]

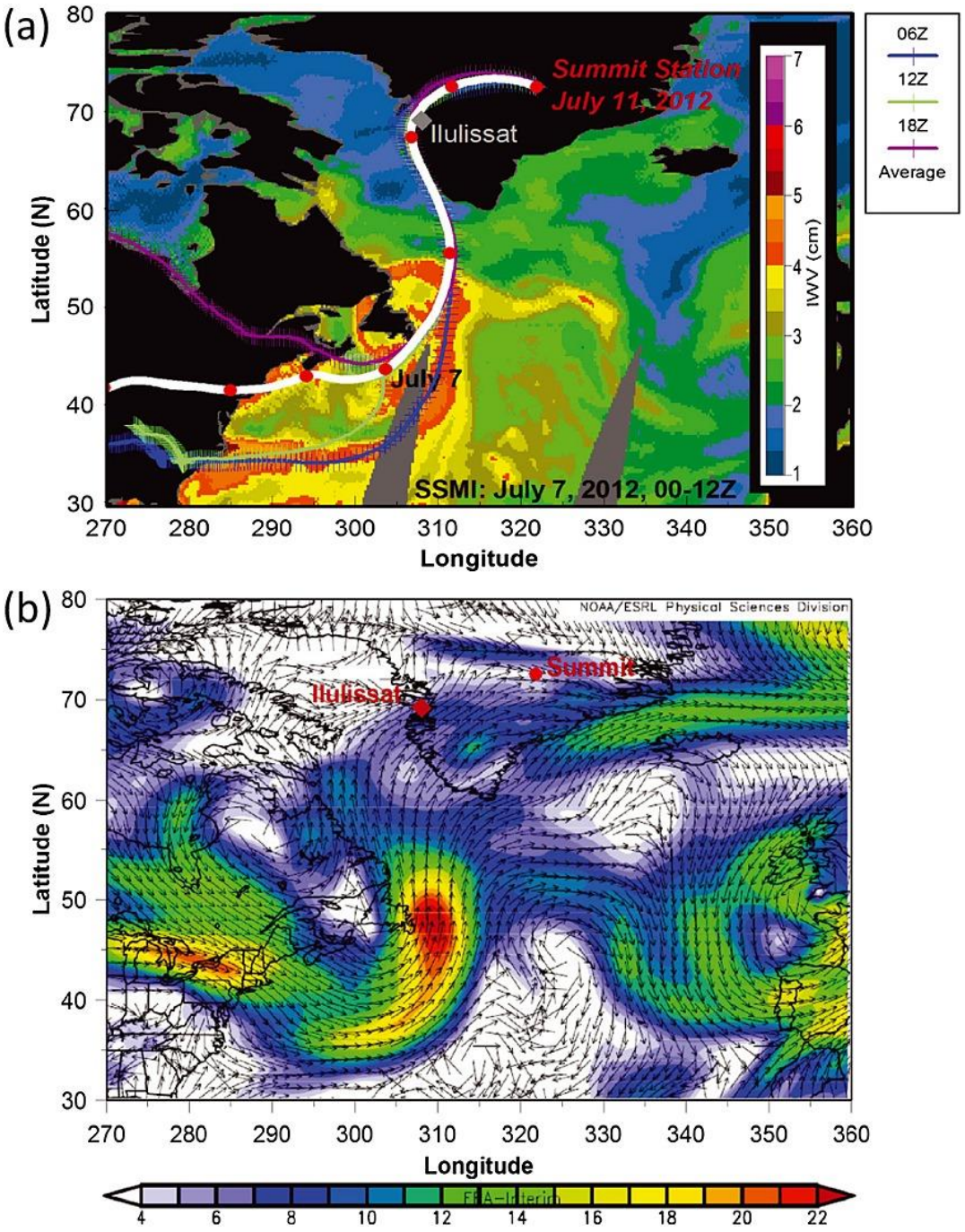

FIG. 1.10. (a) Spectral sensor microwave imagery showing the developing AR and associated integrated water vapor (colored) extending from the eastern U.S. to the southwest coast of Greenland on 7 July 2012. Backward trajectories from the NCEP/DOE reanalysis start from Summit Station at 0600 (blue), 1200 (light green), and 1800 (purple) UTC 11 July. The average of the three trajectories is shown in white (daily interval is denoted by the red circles). (b) ERA-Interim 700-hPa wind vectors and wind speed (m s^{-1}) for 7 July. [Figure 2 and adapted caption from Neff et al. (2014).]

2. Data and Methodology

2.1 SOMs Climatology

SOMs are a type of artificial neural network that clusters data points into various nodes according to the similarity between the values of the data points (Kohonen 1995, 106–109). SOMs can be useful for identifying synoptic flow patterns because they allow for objective classification of these patterns over a large dataset. The number of nodes that are mapped during the training process (i.e., the clustering of data points into various nodes) is subjectively chosen by the user. If the number of nodes chosen is too large, this choice can result in the erroneous classification of closely related synoptic flow patterns as independent synoptic flow patterns. If the number of nodes chosen is too small, this choice can result in the failure to identify important synoptic flow patterns. Therefore, the number of nodes needs to be large enough to display the full range of variability in the synoptic flow patterns, but small enough to prevent too many closely similar synoptic flow patterns. The user has the option to input a single variable or multiple variables into a SOMs algorithm for mapping during the training process. Single-variable SOMs analyses are useful for identifying characteristic synoptic flow patterns in the dataset, but do not provide information on multiple meteorological variables. Multivariate SOMs analyses provide information on multiple meteorological variables in the dataset, but may be more difficult to interpret than single-variable SOMs.

This thesis utilizes SOMs in order to classify synoptic flow patterns that contribute to Greenland ice-melt events. A synoptic climatology of Greenland ice-melt events is constructed using ERA5 reanalysis data at 0.25° resolution for the April–October 1979–2019 time period. The ERA5 reanalysis data are regridded to 1° resolution to render the data compatible with the SOMs algorithm used in this thesis. Greenland ice-melt events are defined as days during the April–October 1979–2019 time period where the Greenland ice-melt extent is at or above the 90th percentile compared to the climatology developed by the NSIDC. 500-hPa geopotential height and sea level pressure (SLP) are chosen as SOMs variables in order to determine the characteristic synoptic flow patterns during Greenland ice-melt events. 500-hPa geopotential height and SLP data are entered into the SOMs algorithm separately where the Greenland ice-melt event criterion is met to construct single-variable SOMs analyses. 700-hPa geopotential

height and IVT data, as well as SLP and 1000–500-hPa thickness data, are entered into the SOMs algorithm together where the Greenland ice-melt criterion is met to construct multivariate SOMs analyses. A 4 × 3 (i.e., 4 columns × 3 rows) SOMs size is chosen with the expectation that the selected size displays the full range of variability in the synoptic flow patterns. The average of the aforementioned variables is computed for the Greenland ice-melt events placed into each node produced by the SOMs algorithm over a Greenland domain.

2.2 Event and Air Parcel Trajectory Analysis

Gridded 0.5° CFSR analyses are used to construct analyses of the synoptic flow patterns for the late July–early August 2019 Greenland ice-melt event. The late July–early August 2019 Greenland ice-melt event is chosen for analysis in order to investigate a record-breaking summer Greenland ice-melt event that is associated with an AR over the North Atlantic Ocean and a strong blocking anticyclone over Greenland.

Air parcel trajectories are utilized in this thesis in order to identify the sources and diagnose the modifications of air masses that contribute to the late July–early August 2019 Greenland ice-melt event. The software package LAGRANTO, which was developed by Huw Davies, Michael Sprenger, and Heini Wernli (Wernli and Davies 1997a,b; Sprenger and Wernli 2015), is used to compute air parcel trajectories in this thesis. LAGRANTO has been used to identify warm conveyor belts in extratropical cyclones, to delineate long-range transport pathways of moisture and trace substances, and to diagnose stratosphere–troposphere exchange events as summarized by Sprenger and Wernli (2015). LAGRANTO was initially developed to be compatible with ECMWF analysis and forecast data, but has also been used in conjunction with the COSMO nonhydrostatic regional model, the UK Met Office Unified Model, the Weather Research and Forecasting Model, and the 20CR reanalysis in numerous studies that are summarized in Sprenger and Wernli (2015). Uncertainties in the computation of air parcel trajectories between these aforementioned datasets may arise since the datasets differ with respect to the model grid specification and resolution. Other sources of error in the computation of air parcel trajectories include truncation errors, interpolation errors, wind field errors, starting

position errors, and amplification of errors (Stohl 1998). Stohl (1998) summarized numerous studies that showed air parcel trajectories computed from analyzed wind fields typically have average position errors of 20% of the air parcel trajectory distance traveled between different air parcel trajectory models under a variety of meteorological conditions.

Mauro Hermann, a graduate student at ETH Zurich, assisted with running LAGRANTO to compute air parcel trajectories for the late July–early August 2019 Greenland ice-melt event. Forward air parcel trajectories are computed for 10 days every 3 h from European, North Atlantic, and African domains starting at 10, 30, and 50 hPa above ground level (AGL) and separated equidistantly every 80 km horizontally. Forward air parcel trajectories are initialized in the European domain in order to investigate the connection between the late July–early August 2019 Greenland ice-melt event and a preceding late July 2019 European heat wave. Forward air parcel trajectories are initialized in the North Atlantic domain in order to trace the pathways of air parcels moving through ARs and to quantify the contribution of diabatic heating due to latent heating within these ARs. Forward air parcel trajectories are initialized in the African domain to determine whether anomalously warm air over northwest Africa on 21–24 July 2019 subsequently reaches Greenland.

Backward air parcel trajectories are computed from a Greenland domain for 10 days every 3 h starting at 925, 850, 700, 600, and 500 hPa and separated equidistantly every 80 km horizontally. Backward air parcel trajectories are computed to identify the sources and diagnose the modifications of air masses that contribute to the late July–early August 2019 Greenland ice-melt event. There are 986 backward air parcel trajectories starting at 925 hPa (Fig. 2.1a) and 1060 backward air parcel trajectories starting at 850 hPa (Fig. 2.1b) over the Greenland domain, while there are 1275 backward air parcel trajectories for each pressure level starting at 700, 600, and 500 hPa over the Greenland domain (Fig. 2.1c). The differences in the number of air parcel trajectories at the respective pressure levels is determined by what percentage of the area of each grid box is below ground. Backward air parcel trajectories starting at 925 and 850 hPa will be used to analyze air parcels that start over coastal Greenland and offshore of Greenland, while backward air parcel trajectories starting at 700, 600, and 500 hPa will be used to analyze air parcels that start over inland regions of Greenland. Selected ERA-Interim variables (i.e.,

pressure, temperature, potential temperature, and specific humidity) are traced along the air parcel trajectories.

A Lagrangian evaluation of the thermodynamic energy equation (adopted from Hermann et al. 2020) is utilized in this thesis in order to quantify the respective contributions of adiabatic and diabatic processes to temperature changes along the backward air parcel trajectories. The thermodynamic energy equation may be expressed as follows:

$$\frac{DT}{Dt} = \frac{\kappa T \omega}{p} + H\left(\frac{p_0}{p}\right)^{-\kappa} \quad (1)$$

where T is the temperature, $p_0 = 1000$ hPa is the reference pressure, p is the pressure, $\kappa = \frac{R}{C_p} = 0.286$ is a constant, R is the gas constant for dry air, C_p is the specific heat of dry air at constant pressure, $H = \frac{D\theta}{Dt}$ is the Lagrangian rate of change of potential temperature, θ is the potential temperature, and $\omega = \frac{Dp}{Dt}$ is the vertical velocity.

The temperature change along the backward air parcel trajectories can be separated into adiabatic and diabatic contributions:

$$\triangle T = \triangle T_{adiab} + \triangle T_{diab} \quad (2)$$

where $\frac{D}{Dt}T_{adiab} = \frac{\kappa T \omega}{p}$ and $\frac{D}{Dt}T_{diab} = H\left(\frac{p_0}{p}\right)^{-\kappa}$ from Eq. (1). The diabatic temperature change every 3 h along the backward air parcel trajectories is computed from θ and p using the following numerical approximation:

$$\triangle T_{diab} = \sum_{dt=3\ h} \left[(\theta_t - \theta_{t-dt})\left(\frac{2p_0}{p_t + p_{t-dt}}\right)^{-\kappa}\right] \quad (3)$$

The adiabatic temperature change every 3 h along the backward air parcel trajectories is computed by subtracting the diabatic temperature change from Eq. (3) from the temperature change along the air parcel trajectories determined from the left-hand side of Eq. (2) for every 3 h interval. The temperatures changes, along with their adiabatic and diabatic contributions, are then summed up over the previous 4 days for every backward air parcel trajectory arriving every 6 h at 925, 850, 700, 600, and 500 hPa over the Greenland domain.

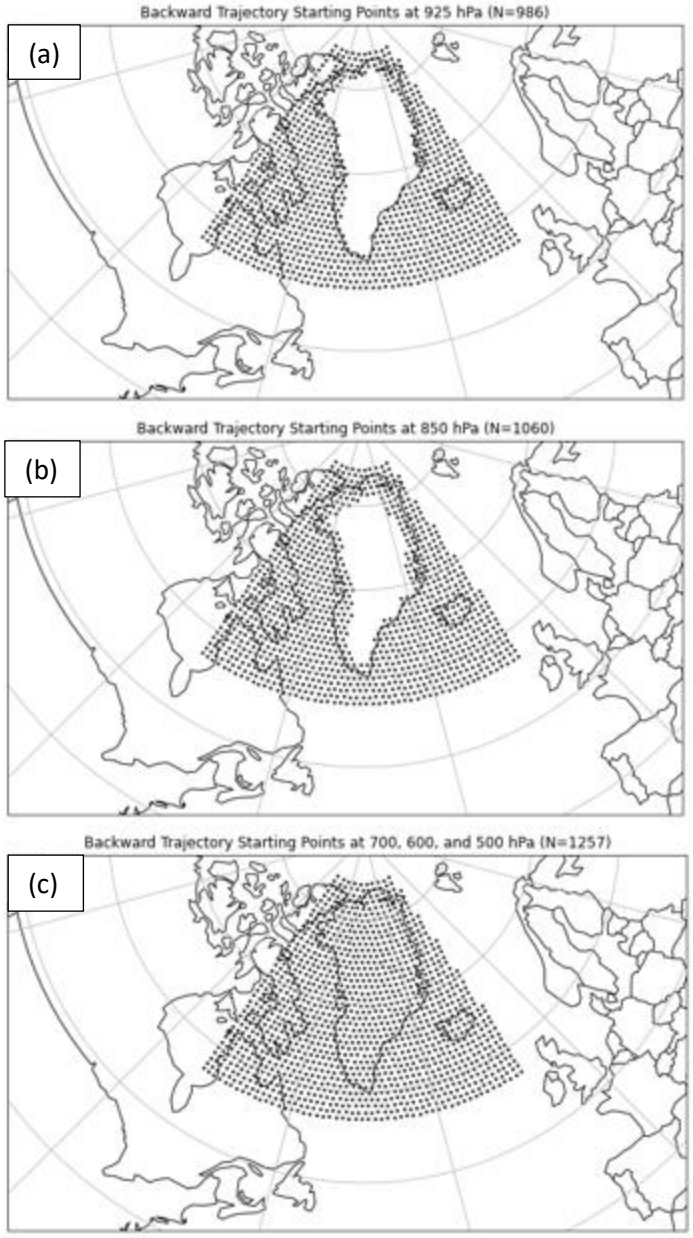

FIG. 2.1. Backward air parcel trajectory starting points (black dots) over the Greenland domain at (a) 925 hPa, (b) 850 hPa, and (c) 700, 600, and 500 hPa.

3. Climatology

3.1 Climatological Breakdown of Greenland Ice-Melt Events

Greenland ice-melt events are defined as days during the April–October 1979–2019 time period where the Greenland ice melt extent is at or above the 90th percentile compared to climatology according to the NSIDC (https://nsidc.org/greenland-today/greenland-surface-melt-extent-interactive-chart/). There are 966 Greenland ice-melt events that occur during the April–October 1979–2019 time period, which are broken down by year (Fig. 3.1) and by month (Fig. 3.2). There are 930 Greenland ice-melt events that occur during the April–October 1979–2018 time period, which are broken down into a histogram by decade (Fig. 3.3).

Figure 3.1 exhibits an increase in frequency of Greenland ice-melt events with time. For example, there are 42 Greenland ice-melt events (i.e., 4.3% frequency of occurrence) during 1979–1988, while there are 439 Greenland ice-melt events (i.e., 45.4% frequency of occurrence) during 2010–2019. The top 3 years with the highest frequency of Greenland ice-melt events (i.e., 2012, 2010, and 2016) occur in the most recent decade in the climatology. The year 2012 has 84 Greenland ice-melt events (i.e., 8.7% frequency of occurrence), 2010 has 78 Greenland ice-melt events (i.e., 8.1% frequency of occurrence), and 2016 has 65 Greenland ice-melt events (i.e., 6.7% frequency of occurrence).

The top 3 months with the highest frequency of Greenland ice-melt events (i.e., July, June, and August) all occur during the summer ice-melt season (Fig. 3.2). April has more Greenland ice-melt events than May for the spring ice-melt season, while October has more Greenland ice-melt events than September for the fall ice-melt season. This trend is unexpected since April and October tend to be colder months climatologically than May and September. However, the upper-level flow in the middle latitudes tends to be more amplified in April and October compared to May and September, which may be associated with a higher occurrence of strong poleward WAA and moisture transport toward Greenland in April and October compared to May and September.

Figure 3.3 exhibits how the distribution of Greenland ice-melt events changes by decade. From 1979–1988 (Fig. 3.3a) to 1989–1998 (Fig. 3.3b), the right tail of the histogram becomes

longer (i.e., there are more years that have a higher number of Greenland ice-melt events during 1989–1998 than during 1979–1988). From 1989–1998 (Fig. 3.3b) to 1999–2008 (Fig. 3.3c), both tails of the histogram become longer and Fig. 3.3c corresponds more closely to a normal distribution. From 1999–2008 (Fig. 3.3c) to 2009–2018 (Fig. 3.3d), the distribution shifts further to the right (i.e., there are no years that have fewer than 12 Greenland ice-melt events).

3.2 Single Variable SOMs

3.2.1 500-hPa Geopotential Height

A common flow signature during Greenland ice-melt events is an upper-level ridge axis that can be located west of, over, or east of Greenland (Fig. 3.4). A large percentage of Greenland ice-melt events occur with a strong ridge over Greenland that is part of an omega block irrespective of whether the upstream and downstream troughs are strong or weak. The 500-hPa geopotential height SOMs transition from a strong blocking pattern over Greenland in the top-left corner, to a ridge over Greenland and a trough upstream of Greenland in the second row, to a negatively tilted trough upstream of Greenland in the bottom right-hand corner (Fig. 3.4).

Examples of characteristic 500-hPa geopotential height and standardized 500-hPa geopotential height anomaly patterns shown in Fig. 3.4 are as follows: (i.) node 0 exhibits a strong blocking pattern with strong positive standardized 500-hPa geopotential height anomalies over Greenland; (ii.) node 3 exhibits a trough–ridge–trough pattern with positive standardized 500-hPa geopotential height anomalies over far southern Greenland and negative standardized 500-hPa geopotential height anomalies over far northeastern Greenland; (iii.) node 4 exhibits a trough–ridge pattern with positive standardized 500-hPa geopotential height anomalies over Greenland; (iv.) node 7 exhibits a trough–ridge pattern with negative standardized 500-hPa geopotential height anomalies over Greenland; (v.) node 8 exhibits a negatively tilted trough upstream of Greenland with weak negative to weak positive standardized 500-hPa geopotential height anomalies over Greenland; (vi.) node 11 exhibits a negatively tilted trough upstream of Greenland with strong negative standardized 500-hPa geopotential height anomalies over Greenland. The 500-hPa geopotential height patterns tend to vary more between rows and vary less between columns within each row. The standardized 500-hPa geopotential height anomalies

tend to decrease in magnitude of from positive to negative between columns from left to right in each row.

The seasonality of the aforementioned 500-hPa geopotential height and standardized 500-hPa geopotential height anomaly patterns in the climatology are analyzed by showing the number of cases mapped to each node per month (Fig. 3.5). Summer Greenland ice-melt events often occur in conjunction with 500-hPa geopotential height patterns consisting of a strong blocking pattern (e.g., node 0) and a trough–ridge pattern (e.g., node 4), with positive standardized 500-hPa geopotential height anomalies over Greenland. Spring and fall Greenland ice-melt events often occur in conjunction with 500-hPa geopotential height patterns consisting of a negatively tilted trough upstream of Greenland (e.g., node 11), with negative standardized 500-hPa geopotential height anomalies over Greenland. Nodes 3, 7, and 11 have maxima of Greenland ice-melt events in April and October, which is consistent with the typical occurrence of stronger flow and lower 500-hPa geopotential heights during the transition seasons than during the summer.

3.2.2 SLP

Greenland ice-melt events can be associated with both high and low SLP over Greenland, as well as semipermanent climatological SLP patterns that are located west (e.g., the Beaufort high) and east (e.g., the Icelandic low and the Azores high) of Greenland (Fig. 3.6). The SLP SOMs transition from high SLP with positive standardized SLP anomalies over Greenland in the top left-hand corner to low SLP with negative standardized SLP anomalies over Greenland in the bottom right-hand corner (Fig. 3.6). The SLP over Greenland is as high as 1032 hPa in the top left-hand corner and is as low as 1008 hPa in the bottom right-hand corner, with SLP gradients between 4–8 hPa over Greenland.

Examples of characteristic SLP and standardized SLP anomaly patterns identified in Fig. 3.6 are as follows: (i.) node 0 exhibits high SLP over Baffin Bay and Greenland with positive standardized SLP anomalies, and low SLP over Europe with negative standardized SLP anomalies; (ii.) node 3 exhibits low SLP and strong negative SLP anomalies near southeastern

Greenland and Iceland; (iii.) node 5 exhibits high SLP over Greenland with positive standardized SLP anomalies, and low SLP over North America and Europe with neutral to negative SLP anomalies; (iv.) node 8 exhibits low SLP with strong negative standardized SLP anomalies over far northeastern North America, and high SLP with strong positive SLP anomalies over the north-central U.S., Greenland and the eastern North Atlantic Ocean; (v.) node 11 exhibits low SLP over Baffin Bay and Greenland with negative standardized SLP anomalies, and high SLP over the North Atlantic Ocean and Europe with positive standardized SLP anomalies.

The seasonality of the SLP and standardized SLP anomaly patterns in the climatology are analyzed by showing the number of cases mapped to each node per month (Fig. 3.7). Spring Greenland ice-melt events often occur in conjunction with high SLP and positive standardized SLP anomalies west of and over Greenland (e.g., nodes 0, 4, and 8). These SLP and standardized SLP anomaly patterns may be a manifestation of the Beaufort high, which often extends eastward over Baffin Bay and the Canadian Archipelago in the spring. Summer Greenland ice-melt events often occur in conjunction with high SLP and positive standardized SLP anomalies over the North Atlantic Ocean (e.g., nodes 6, 10, and 11). These SLP and standardized SLP anomaly patterns may be a manifestation of the Azores high, which often extends northward over the North Atlantic Ocean in the summer. Fall Greenland ice-melt events often occur in conjunction with low SLP and strong negative SLP anomalies near southeastern Greenland and Iceland (e.g., nodes 2 and 3). These SLP and standardized SLP anomaly patterns may be a manifestation of the Icelandic low, which can begin to develop in the fall and is often strongest in the winter. A strong west to east SLP gradient with low SLP south and west of Greenland and high SLP south and east of Greenland (e.g., nodes 8 and 9) can induce ice melt via a strong southerly surface flow that may be associated with the transport of warm and moist air from the lower latitudes toward Greenland. This SLP pattern can occur in conjunction with spring, summer, and fall Greenland ice-melt events (e.g., nodes 8 and 9).

3.3 Multivariate SOMs

3.3.1 700-hPa Geopotential Height and IVT

Greenland ice-melt events can be associated with both strong blocking anticyclones and low IVT over Greenland, and with deep troughs upstream of Greenland and high IVT over Greenland (Fig. 3.8). Strong blocking anticyclones can induce Greenland ice melt due to warm and dry air over Greenland that is associated with large-scale subsidence. Deep troughs upstream of Greenland can induce Greenland ice melt due to warm and moist air over Greenland that is associated with WAA via southerly flow downstream of the trough axis.

Examples of characteristic 700-hPa geopotential height and IVT patterns identified in Fig. 3.8 are as follows: (i.) node 0 exhibits a short-wave trough upstream of Greenland with highest IVT south of Greenland; (ii.) node 3 exhibits a negatively tilted trough over the eastern North Atlantic Ocean with highest IVT over the eastern North Atlantic Ocean and Europe; (iii.) node 6 exhibits a negatively tilted trough over eastern North America and the western North Atlantic Ocean with high IVT over southern Greenland; (iv.) node 8 exhibits a strong blocking anticyclone over Greenland with low IVT over Greenland; (v.) node 11 exhibits a positively tilted trough over eastern North America with high IVT southwest of Greenland.

The seasonality of the 700-hPa geopotential height and IVT patterns in the climatology are analyzed by showing the number of cases mapped to each node per month (Fig. 3.9). Summer Greenland ice-melt events often occur in conjunction with a strong blocking anticyclone over Greenland with low IVT over Greenland (e.g., node 8 and 9). Spring and fall Greenland ice-melt events often occur in conjunction with a negatively tilted trough over eastern North America and the western North Atlantic Ocean with high IVT over southern Greenland (e.g., node 6), or a positively tilted trough over eastern North America with high IVT southeast of Greenland (e.g., node 11). The seasonality of these patterns is consistent with Figs. 3.4 and 3.5, which show that summer Greenland ice-melt events often occur in conjunction with strong blocking patterns over Greenland (e.g., node 0) (Figs. 3.4 and 3.5), while spring and fall Greenland ice-melt events often occur in conjunction with a negatively tilted trough upstream of Greenland (e.g., node 11) (Figs. 3.4 and 3.5).

3.3.2 SLP and 1000–500-hPa Thickness

Greenland ice-melt events are associated with thickness troughs upstream and downstream of Greenland, with varying SLP patterns over Greenland (Fig. 3.10). The SLP pattern transitions from higher SLP over Greenland in the first row to lower SLP over Greenland in the last row, with little variation in SLP between columns within a given row. The 1000–500-hPa thickness increases over Greenland from left to right within a given row, indicating a warmer air mass for a similar SLP pattern. The 540-dam thickness contour can be used as a proxy to distinguish between where snow or rain is most likely at lower elevations along the boundaries of the Greenland ice sheet.

Examples of characteristic SLP and 1000–500-hPa thickness patterns identified in Fig. 3.10 are as follows: (i.) node 0 exhibits high SLP over Greenland and a strong 1000–500-hPa thickness gradient over Greenland, with the 540-dam thickness contour over southern Greenland and the 516-dam thickness contour over northern Greenland; (ii.) node 8 exhibits low SLP over southeastern Greenland, with the 540-dam thickness contour over eastern North America and extending eastward over the North Atlantic Ocean; (iii.) node 11 exhibits low SLP over Baffin Bay and western Greenland, with the 540-dam thickness contour over northern Greenland.

The seasonality of the SLP and 1000–500-hPa thickness patterns in the climatology are analyzed by showing the number of cases mapped to each node per month (Fig. 3.11). Summer Greenland ice-melt events occur in conjunction with high and low SLP over Greenland, with the 540-dam thickness contour located north of Greenland in the warmest nodes (e.g., nodes 3, 7, and 11). Spring and fall Greenland ice-melt events occur in conjunction with high and low SLP over Greenland, with the 540-dam thickness contour over southern Greenland, as well as eastern North America and extending eastward over the North Atlantic Ocean in the coldest nodes (e.g., nodes 0, 4, and 8).

3.4 Linkages Between the SOMs

Greenland ice-melt events are most likely (i.e., the nodes with the highest number of Greenland ice-melt events for each of the SOMs) when the patterns of 500-hPa geopotential height, SLP, 700-hPa geopotential height and IVT, as well as SLP and 1000–500-hPa thickness,

favor a strong blocking pattern over Greenland (i.e., node 0) (Fig. 3.4), low SLP over Baffin Bay and Greenland, (i.e., node 11) (Fig. 3.6), a strong blocking anticyclone and low IVT over Greenland (i.e., node 8) (Fig. 3.8), and low SLP and a thickness trough upstream and downstream of Greenland with the 540-dam thickness contour over northern Greenland (i.e., node 11) (Fig. 3.10). Greenland ice-melt events are least likely (i.e., the nodes with the lowest number of Greenland ice-melt events for each of the SOMs) when the same patterns favor a negatively tilted trough upstream of Greenland (i.e., node 10) (Fig. 3.4), low SLP west of, over, and east of Greenland (i.e., node 7) (Fig. 3.6), a short-wave trough upstream of Greenland and high IVT over the eastern North Atlantic Ocean (i.e., node 2) (Fig. 3.8), and high SLP and a thickness trough upstream and downstream of Greenland with the 540-dam thickness contour over eastern North America and extending eastward over the North Atlantic Ocean, (i.e., node 4) (Fig. 3.10).

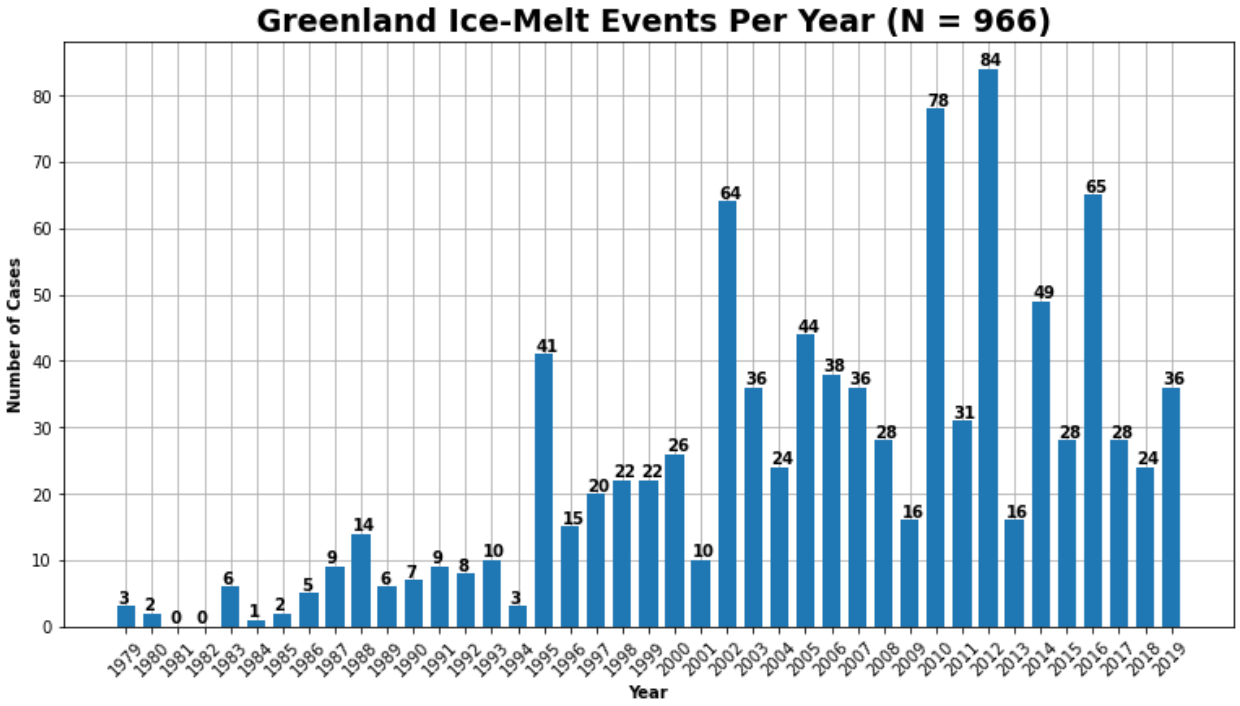

FIG. 3.1. Greenland ice-melt events per year for the April–October 1979–2019 period.

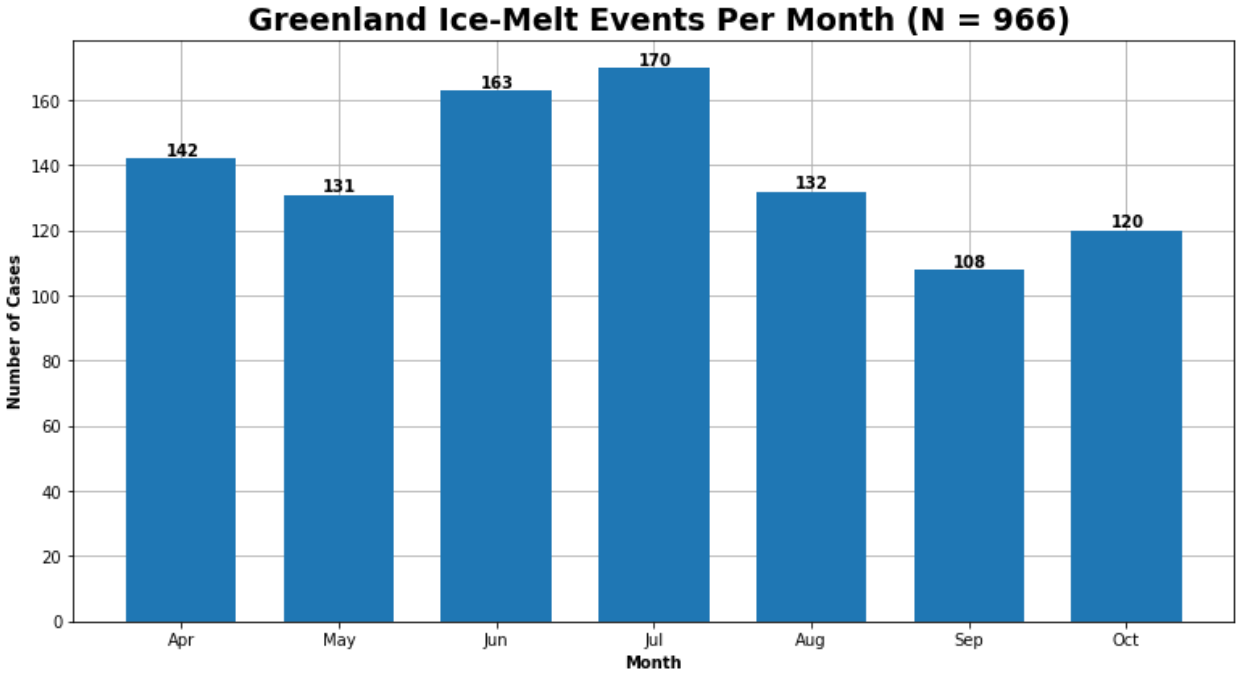

FIG. 3.2. Greenland ice-melt events per month for the April–October 1979–2019 period.

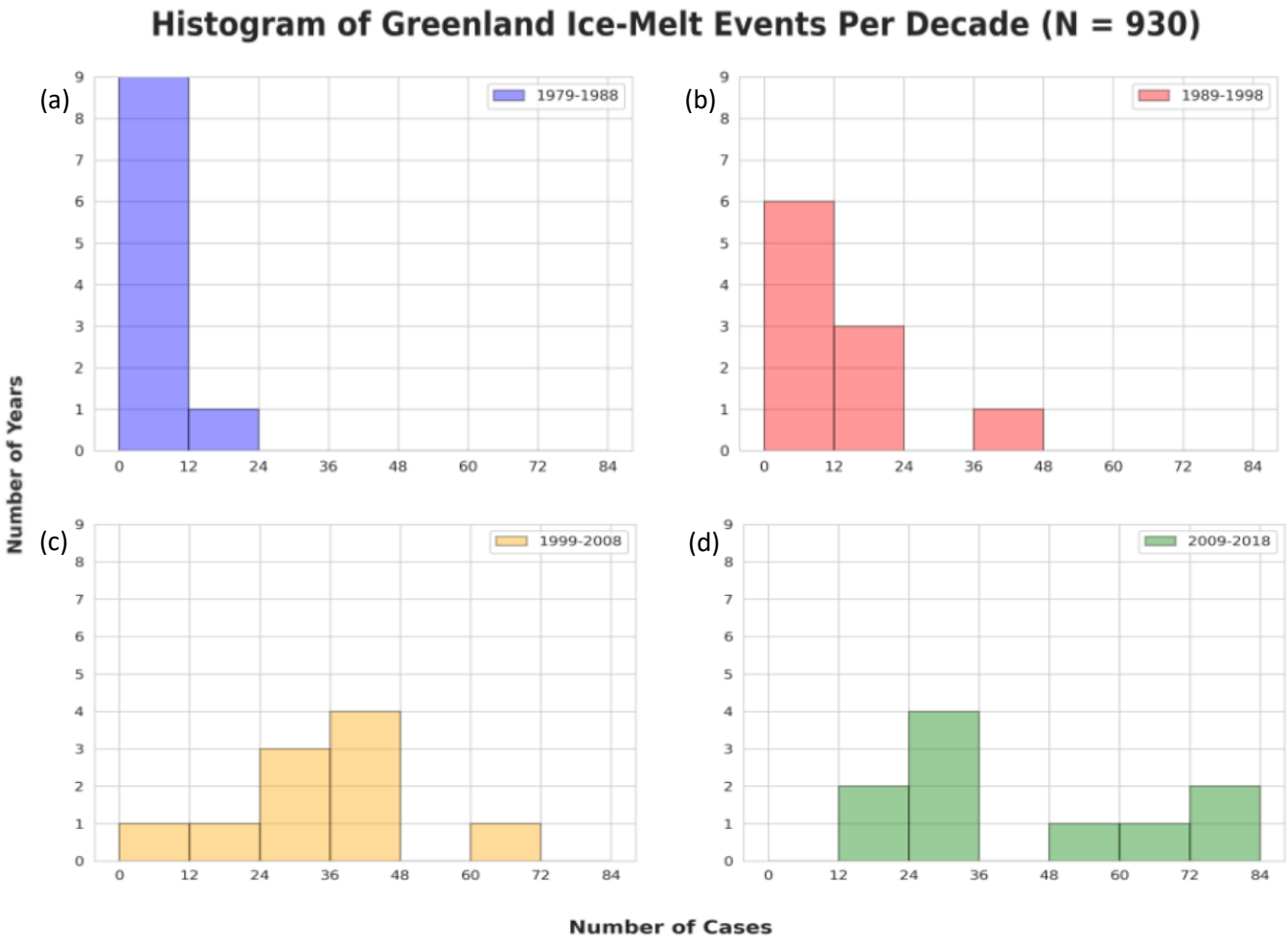

FIG. 3.3. Histogram of Greenland ice-melt events per decade for the April–October 1979–2018 period.

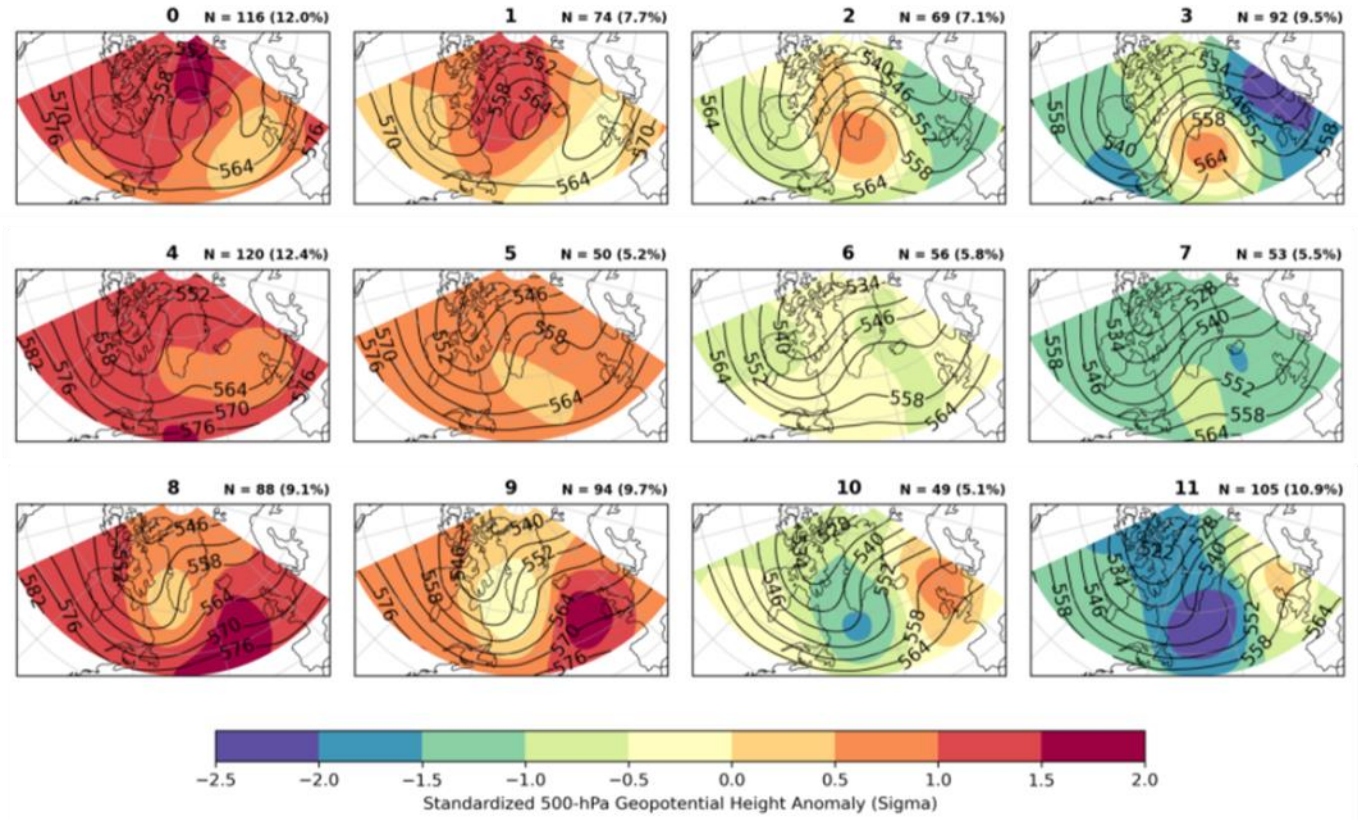

FIG. 3.4. 4 × 3, single-variable SOMs of 500-hPa geopotential height (dam; black) and standardized 500-hPa geopotential height anomaly (σ, shaded) for the April–October 1979–2019 period during Greenland ice-melt events. The number of Greenland ice-melt events and the percent frequency of occurrence mapped to each node are given in the top right-hand corner of each panel.

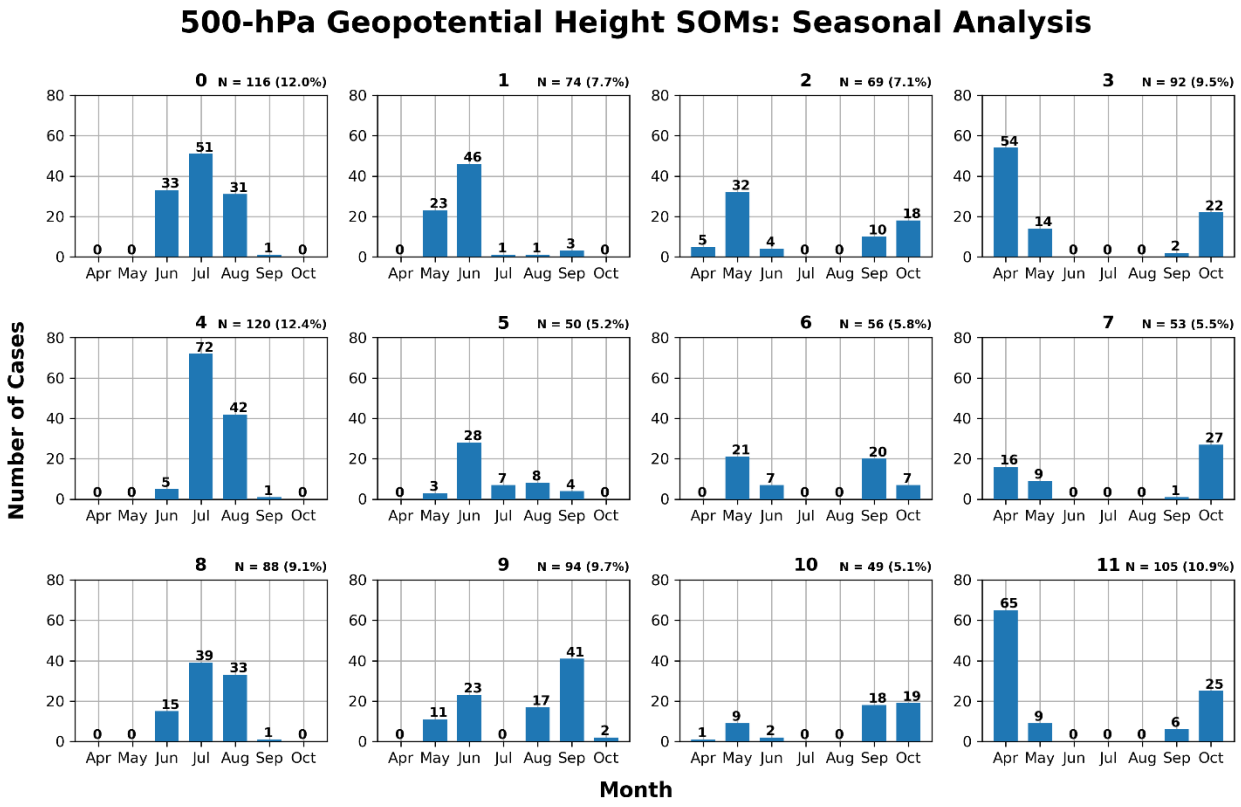

FIG. 3.5. Greenland ice-melt events per month for each node identified by the 500-hPa geopotential height SOMs. The number of Greenland ice-melt events and the percent frequency of occurrence mapped to each node are given in the top right-hand corner of each panel.

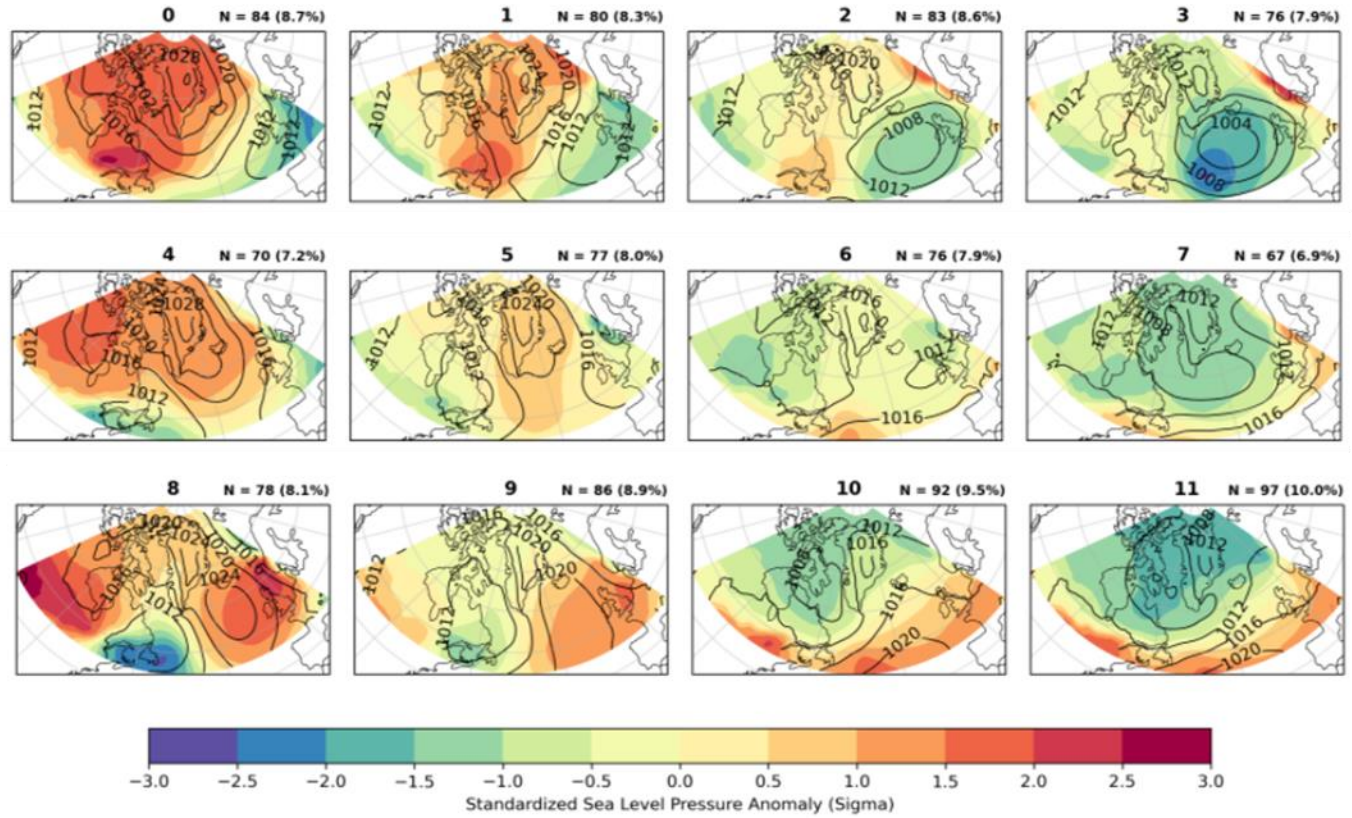

FIG. 3.6. 4 × 3, single-variable SOMs of SLP (hPa; black) and standardized SLP anomaly (σ, shaded) for the April–October 1979–2019 period during Greenland ice-melt events. The number of Greenland ice-melt events and the percent frequency of occurrence mapped to each node are given in the top right-hand corner of each panel.

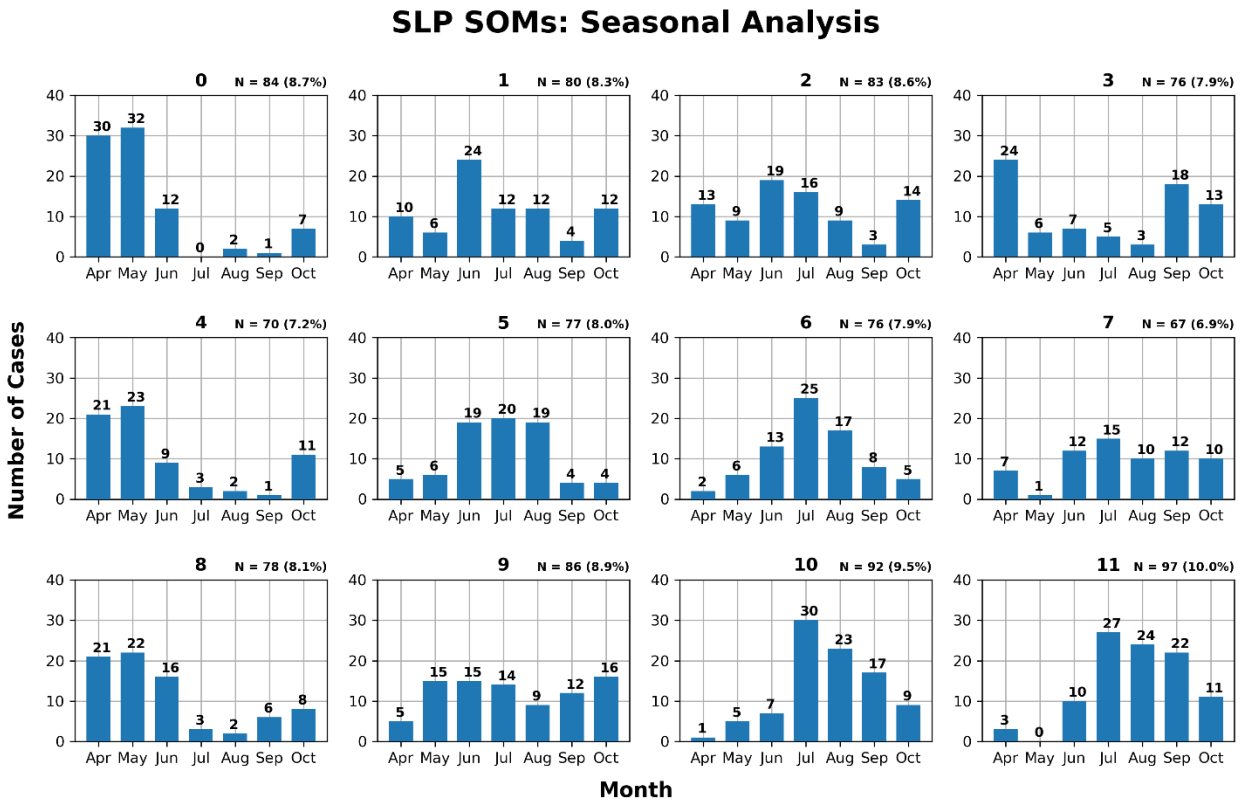

FIG. 3.7. Greenland ice-melt events per month for each node identified by the SLP SOMs. The number of Greenland ice-melt events and the percent frequency of occurrence mapped to each node are given in the top right-hand corner of each panel.

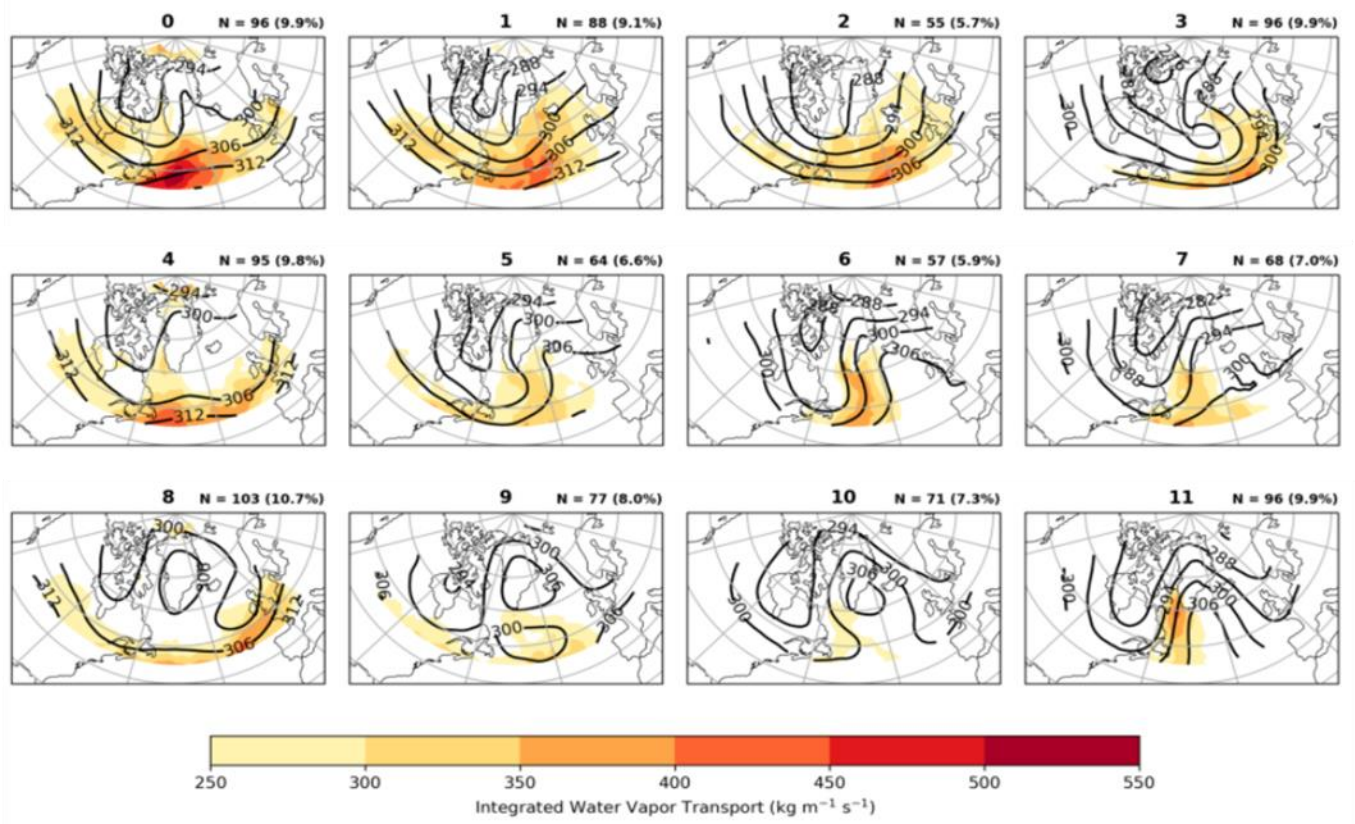

FIG. 3.8. 4 × 3, multivariate SOMs of 700-hPa geopotential height (dam; black) and IVT (kg m^{-1} s^{-1}; shaded) for the April–October 1979–2019 period during Greenland ice-melt events. The number of Greenland ice-melt events and the percent frequency of occurrence mapped to each node are given in the top right-hand corner of each panel.

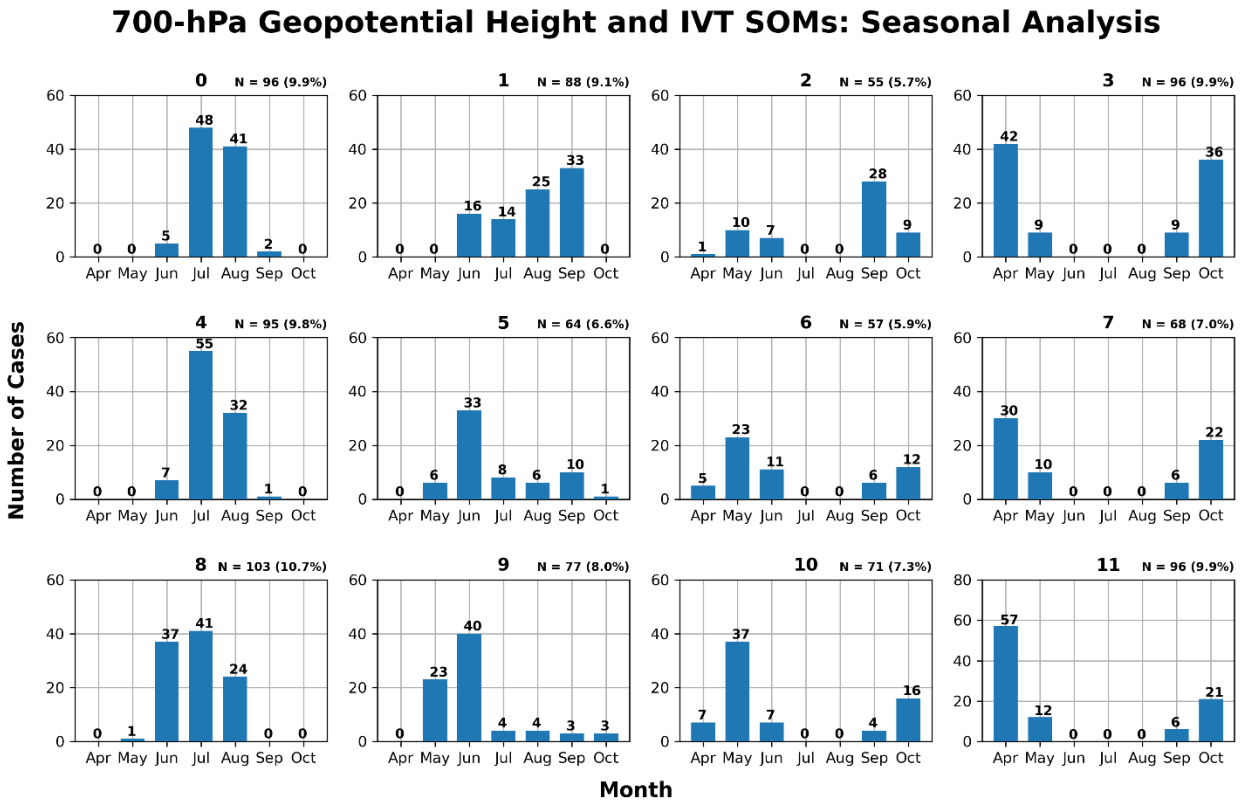

FIG. 3.9. Greenland ice-melt events per month for each node identified by the 700-hPa geopotential height and IVT SOMs. The number of Greenland ice-melt events and the percent frequency of occurrence mapped to each node are given in the top right-hand corner of each panel.

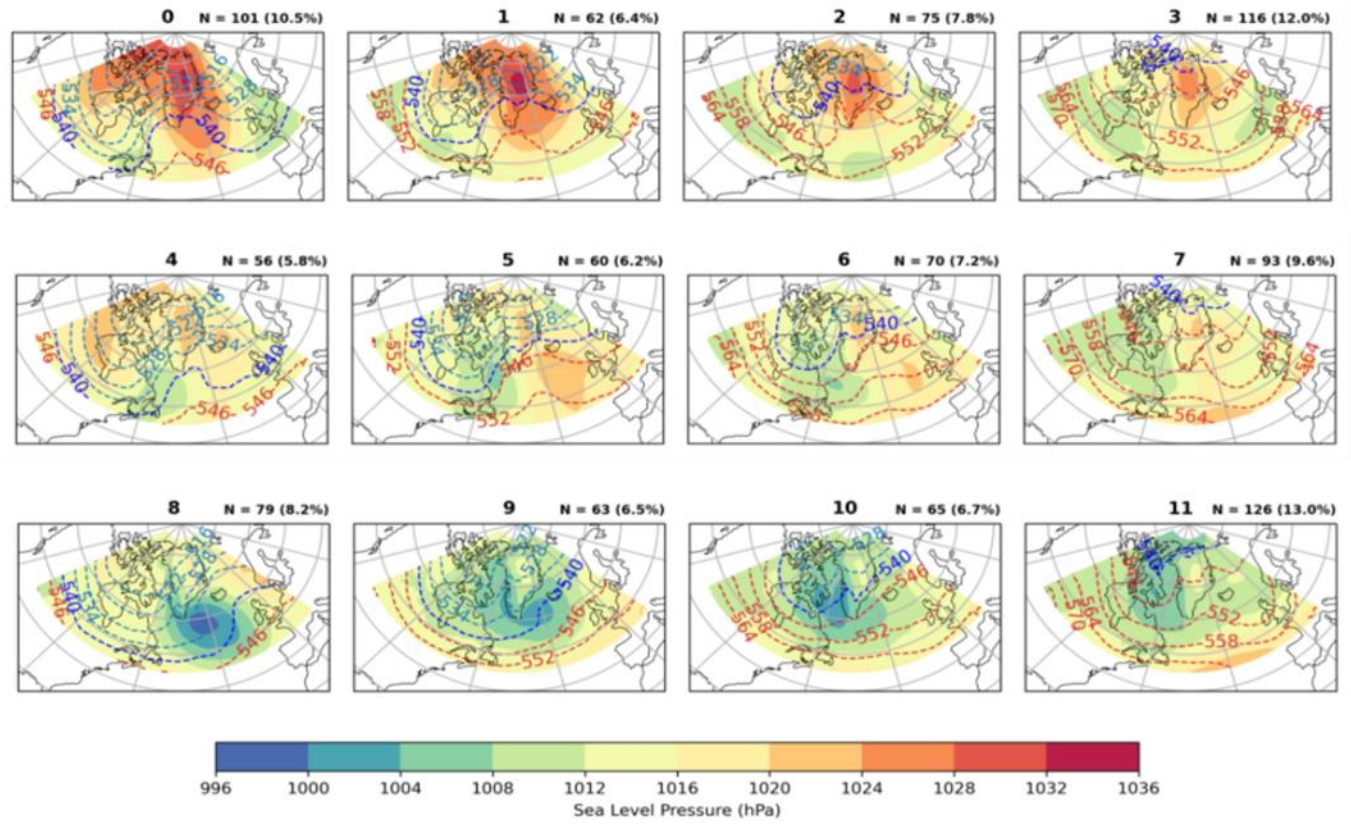

FIG. 3.10. 4 × 3, multivariate SOMs of SLP (hPa; shaded) and 1000–500-hPa thickness (< 540 dam; light blue, 540 dam; dark blue, and > 540 dam; red) for the April–October 1979–2019 period during Greenland ice-melt events. The number of Greenland ice-melt events and the percent frequency of occurrence mapped to each node are given in the top right-hand corner of each panel.

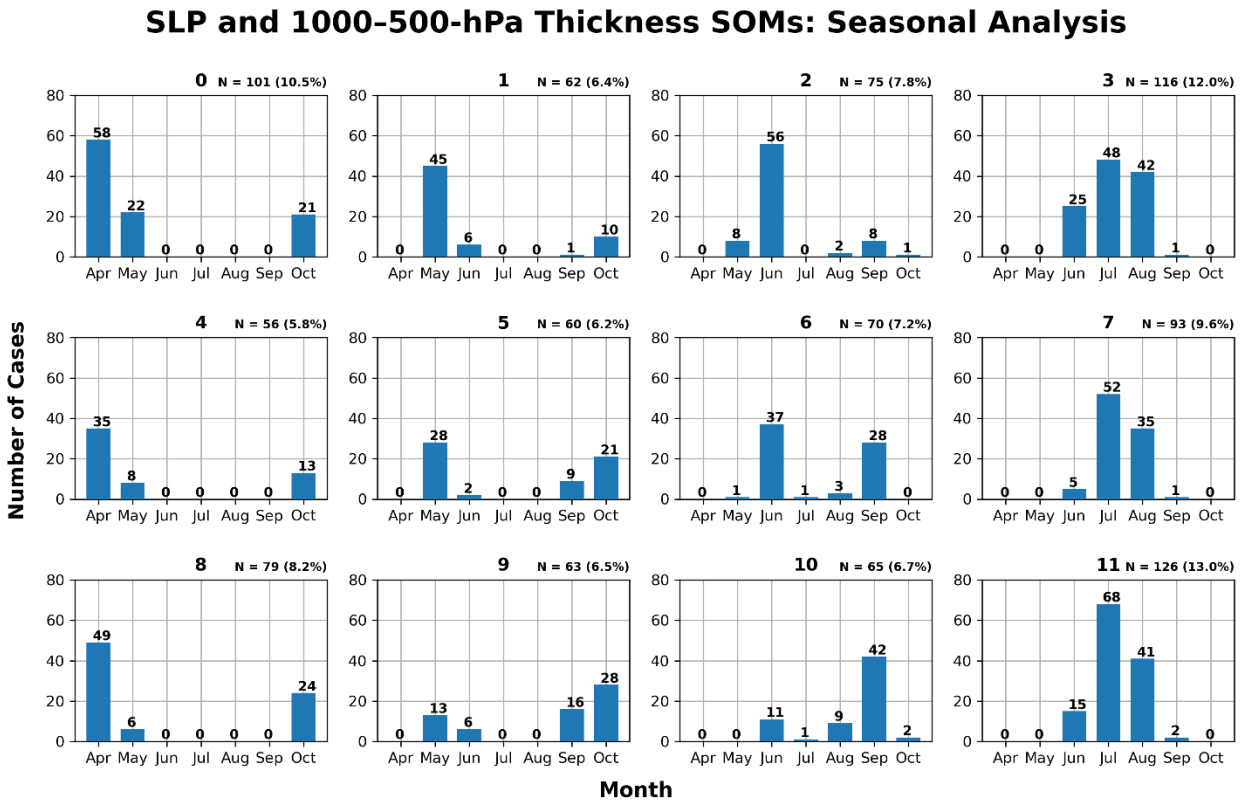

FIG. 3.11. Greenland ice-melt events per month for each node identified by the SLP and 1000–500-hPa thickness SOMs. The number of Greenland ice-melt events and the percent frequency of occurrence mapped to each node are given in the top right-hand corner of each panel.

4. Case Study

4.1 The Late July–Early August 2019 Greenland Ice-Melt Event

4.1.1 Event Overview and Large-Scale Flow Evolution

During late July–early August 2019, Greenland experienced the largest ice melt since at least 2012, in which 60 percent of the ice sheet saw one millimeter or more of melting (Fig. 4.1) (open source). The NSIDC estimated that 12.5 billion tons of ice melted on 1 August 2019, which is the largest single-day ice-volume loss on record (https://www.washingtonpost.com/weather/2019/08/01/greenland-ice-sheet-poured-billion-tons-water-into-north-atlantic-july-alone/). Both coastal regions (i.e., low elevations) and inland regions (i.e., high elevations) of the Greenland ice sheet experienced ice melt on 31 July 2019 (Fig. 4.2a). A sounding from Ittoqqortoormiit, Greenland (location denoted by a yellow star in Fig. 4.2a), at 0000 UTC 1 August 2019 shows an 850-hPa temperature of 13.2°C with a temperature above 0°C up to ~660 hPa (Fig. 4.2b), which indicates an air mass warm enough to melt ice in coastal and inland regions of Greenland.

The antecedent evolution of the large-scale flow pattern contributed to the record-breaking ice melt over Greenland during late July–early August 2019. A strong zonally oriented jet streak over eastern North America and the western North Atlantic Ocean enabled a series of short-wave troughs to progress eastward in conjunction with amplification of the upper-level flow from eastern North America to western Europe during 23–24 July 2019 (Figs. 4.3a,c). As the upper-level flow across the North Atlantic Ocean amplified, a 594-dam ridge was located downstream over northwest Africa during 23–24 July 2019 (Figs. 4.3b,d). A progressive short-wave trough over the western North Atlantic Ocean became increasingly negatively tilted and more amplified as it approached the eastern North Atlantic Ocean during 25–26 July 2019 (Figs. 4.4a,c). A strengthening southeasterly flow ahead of this negatively tilted trough facilitated downstream ridge amplification from northwest Africa to western Europe during 25–26 July 2019 (Figs. 4.4a,c). Strong positive standardized 850-hPa temperature anomalies as high as 4–5σ compared to climatology occurred downstream of the negatively tilted trough over Europe during 25–26 July 2019 (Figs. 4.4b,d). The merger of an

upper-level anticyclone over the Arctic Circle and a blocking anticyclone that formed over Scandinavia helped facilitate strong easterly flow across Greenland and Scandinavia during 27–28 July 2019 (Figs. 4.5a,c). The strong easterly flow across Greenland and Scandinavia permitted anomalously warm air over Scandinavia to move westward toward Greenland during 27–28 July 2019 (Figs. 4.5b,d). The blocking anticyclone that formed over Scandinavia subsequently moved westward toward Greenland during 29 July–1 August 2019 in conjunction with the breakdown of the aforementioned negatively tilted trough into a series of cutoff cyclones equatorward of 60°N. As the blocking anticyclone moved westward, strong positive standardized 850-hPa temperature anomalies as large as 3–4σ compared to climatology (Figs. 4.6a,c and 4.7a,c) and strong positive standardized precipitable water anomalies as large as 3–4σ compared to climatology (Figs. 4.6b,d and 4.7b,d) occurred over Greenland.

4.1.2 Air Parcel Trajectories

Forward air parcel trajectories are initialized in an African domain to determine whether anomalously warm air over northwest Africa during 21–24 July 2019 subsequently reaches Greenland (Fig. 4.8). The air parcels initialized at 1200 UTC 21 July 2019 do not reach Greenland and instead move northeastward toward eastern Europe or southwestward toward the western North Atlantic Ocean (Fig. 4.8a). As a thickness ridge amplifies over northwest Africa and Europe a greater proportion of the air parcels initialized during 1200 UTC 22–24 July 2019 compared to the proportion of air parcels initialized at 1200 UTC 21 July 2019 move northwestward toward western Europe and Greenland (Figs. 4.8b,c,d). Air parcels initialized during 1200 UTC 22–24 July 2019 on the northern part of the northwest African domain tend to move northward due to southerly flow downstream of a trough over the eastern North Atlantic Ocean (Figs. 4.3b,d). Air parcels initialized during 1200 UTC 22–24 July 2019 on the southern part of the domain tend to move southward and westward due to northwesterly flow associated with a ridge over the central North Atlantic Ocean (Figs. 4.3b,d).

Forward air parcel trajectories are initialized in a European domain in order to investigate the connection between the July–early August 2019 Greenland ice-melt event and a preceding late July 2019 European heat wave. Maximum temperatures over Europe during the late July 2019 European heat wave exceeded 40°C (Fig. 4.9) (open source) and set all-time high temperature records in Belgium, France, Germany, Luxembourg, the Netherlands, and the United Kingdom (https://www.insider.com/europe-heat-wave-record-temperatures-deaths-uk-2019-7). Anomalously warm air over Europe during the peak of the late July 2019 European heat wave on 25 July 2019 was able to reach Greenland in subsequent days (Fig. 4.10a). An air parcel initialized over Spain at 1200 UTC 25 July 2019 ascends from ~910 hPa to ~400 hPa as it first reaches Greenland at approximately 1200 UTC 28 July 2019 (Figs. 4.10a,b). This air parcel then moves anticyclonically east of Greenland, moves southward over the Greenland Sea, and then moves eastward across Europe. An air parcel initialized over France at 1200 UTC 25 July 2019 ascends from ~960 hPa to ~600 hPa as it first reaches Greenland at approximately 0000 UTC 29 July 2019 (Figs. 4.10a,b). This air parcel then moves anticyclonically over the Greenland Sea and then southward toward the North Atlantic Ocean. An air parcel initialized over the United Kingdom ascends from ~1000 hPa to ~725 hPa as it first reaches Greenland at approximately 0600 UTC 29 July 2019 (Figs. 4.10a,b). This air parcel then moves westward over Greenland and then northward over Baffin Bay.

Forward air parcel trajectories are initialized at 1200 UTC 25 July 2019 in a North Atlantic Ocean domain in order to trace the pathways of air parcels moving through an AR over the North Atlantic Ocean and to quantify the contribution of diabatic warming due to latent heating within this AR. Air parcels initialized at 1200 UTC 25 July 2019 over this AR (Fig. 4.11a) and south of a jet core at 500 hPa are located just downstream of a ridge axis over the western North Atlantic Ocean during 25–26 July 2019 (Figs. 4.4a,c). These air parcels then move cyclonically around the negatively tilted trough over the eastern North Atlantic Ocean, move northward toward eastern Greenland, and then move anticyclonically westward around the blocking anticyclone over Scandinavia. These air parcels ascend from ~850 hPa to ~480 hPa (Fig. 4.12a), and experience a median potential temperature increase from ~298 K to ~315 K (Fig. 4.12b) and a median specific humidity decrease from ~8 g kg^{-1} to ~1 g kg^{-1} (Fig. 4.12c) during the 72-h period ending on 1200 UTC 28 July 2019. These respective changes in median potential temperature and median specific humidity are

indicative of condensation and latent heating. Air parcels initialized north of the AR (Fig. 4.11b) and the jet core at 500 hPa, and just upstream of the negatively tilted trough over the eastern North Atlantic Ocean (Figs. 4.4a,c) do not reach Greenland. Instead these air parcels move southward before moving westward and dispersing over the central North Atlantic Ocean. These air parcels descend from ~850 hPa to ~975 hPa (Fig. 4.12a), and experience a median potential temperature increase from ~290 K to ~300 K (Fig. 4.12b) and a median specific humidity increase from ~5.5 g kg^{-1} to ~15 g kg^{-1} (Fig. 4.12c) during the 10-d period ending on 1200 UTC 4 August 2019. These respective changes in median potential temperature and median specific humidity are indicative of sensible and latent heat fluxes from the surface due to moistening from below over the North Atlantic Ocean. Figures 4.11a,b show that pathways of forward air parcel trajectories are sensitive to the location of the domain.

Backward air parcel trajectories are initialized in a Greenland domain in order to identify the sources and diagnose the modifications of air masses that contribute to the late July–early August 2019 Greenland ice-melt event. Air parcels originating from Alaska, Quebec, the eastern North Atlantic Ocean, and northwest Africa reach Greenland during peak ice melt at 1800 UTC 31 July 2019 (Fig. 4.13). The air parcel originating from Alaska first moves eastward and cyclonically around the Arctic Circle. This air parcel then moves southeastward over the Arctic Circle and then anticyclonically over the Greenland Sea toward north-central Greenland. During 1800 UTC 28–31 July 2019, this air parcel descends from ~600 hPa to ~700 hPa (Fig. 4.14a), experiences a potential temperature decrease from ~307 K to ~303 K (Fig. 4.14b), and experiences an equivalent potential temperature decrease from ~312 K to ~308 K (Fig. 4.14c). The air parcel originating from Quebec first moves eastward over the North Atlantic Ocean and then moves northward and westward toward the Greenland Sea. This air parcel then moves anticyclonically over the Greenland Sea toward east-central Greenland. During 1800 UTC 28–31 July 2019, this air parcel descends from ~475 hPa to ~600 hPa (Fig. 4.14a), experiences a potential temperature decrease from ~313 K to ~308 K (Fig. 4.14b), and experiences an equivalent potential temperature decrease from ~315 K to ~313 K (Fig. 4.14c). The air parcel originating from the eastern North Atlantic Ocean moves northward and westward toward northwest Greenland. During 1800 UTC 28–31 July 2019, this air parcel descends from ~675 hPa to ~925 hPa (Fig. 4.14a), experiences a potential

temperature decrease from ~295 K to ~288 K (Fig. 4.14b), and experiences an equivalent potential temperature decrease from ~307 K to ~301 K (Fig. 4.14c). The air parcel originating from northwest Africa (Fig. 4.13) at 1200 UTC 22 July 2019 has a potential temperature of ~320 K (Fig. 4.14b) and an equivalent potential temperature of ~341 K (Fig. 4.14c) at ~850 hPa (Fig. 4.14a), which is indicative of a very warm and moist lower-tropospheric air mass over northwest Africa. This air parcel moves northward and westward toward northeastern Greenland. During 1800 UTC 28–31 July 2019, this air parcel ascends from ~675 hPa to ~610 hPa and then descends from ~610 hPa to ~700 hPa (Fig. 4.14a), experiences a potential temperature decrease from ~309 K to ~305 K (Fig. 4.14b), and experiences an equivalent potential temperature decrease from ~325 K to ~317 K (Fig. 4.14c).

A Lagrangian evaluation of the thermodynamic equation is utilized in order to quantify the respective contributions of adiabatic and diabatic processes to temperature changes along the backward air parcel trajectories initialized in the Greenland domain from Fig. 4.13. Orographic ascent and descent contribute to adiabatic temperature changes of air parcels. It will be shown that air parcels that move from lower elevations to higher elevations of Greenland experience orographic ascent due to upslope flow, which enhances adiabatic cooling where there is synoptic-scale ascent. It also will be shown that air parcels that move from higher elevations to lower elevations of Greenland experience orographic descent due to downslope flow, which enhances adiabatic warming where there is synoptic-scale descent.

The adiabatic temperature change (Figs. 4.15a,d) and the diabatic temperature change (Figs. 4.15b,e) sum to the temperature change (Figs. 4.15c,f). During 0000 UTC 28–1800 UTC 29 July 2019, there is strong adiabatic cooling over central and eastern Greenland, and strong adiabatic warming over northern Greenland (Fig. 4.15a). The strong adiabatic cooling over central and eastern Greenland may be indicative of orographic ascent (Fig. 4.5c) and synoptic-scale ascent due to this region being downstream of the negatively tilted trough over the eastern North Atlantic Ocean (Fig. 4.5c). During 0000 UTC 28–1800 UTC 29 July 2019, there is diabatic warming over central Greenland that is maximized near Summit Station, and there is diabatic cooling over northern Greenland (Fig. 4.15b). The diabatic warming over central Greenland may be indicative of condensation and latent heating that is shown in Figs.

4.12a,b,c. During 0000 UTC 28–1800 UTC 29 July 2019, the temperature change (Fig. 4.15c) shows a similar pattern to that shown in Fig. 4.15a because the adiabatic contribution is dominant. During 0000 UTC 30–1800 UTC 31 July 2019, there is strong adiabatic cooling over western and southern Greenland that is maximized near South Dome, and weak-to-moderate adiabatic warming over eastern Greenland (Fig. 4.15d). The weak-to-moderate adiabatic warming over eastern Greenland may be indicative of synoptic-scale descent associated with the blocking anticyclone that formed over Scandinavia and subsequently moved westward toward Greenland during 29 July–1 August. During 0000 UTC 30–1800 UTC 31 July 2019, there is diabatic cooling over north-central and eastern Greenland, and diabatic warming over southwestern Greenland (Fig. 4.15e). During 0000 UTC 30–1800 UTC 31 July 2019, the temperature change (Fig. 4.15f) shows a similar pattern to that shown in Fig. 4.15d because the adiabatic contribution is dominant. Greenland ice melt may have been enhanced by diabatic warming over central Greenland during 0000 UTC 28–1800 UTC 29 July 2019 due to condensation and latent heating associated with the AR that originated over the North Atlantic Ocean on 25 July 2019. Greenland ice melt may have been enhanced by adiabatic warming over eastern Greenland during 0000 UTC 30–1800 UTC 31 July 2019 due to synoptic-scale descent associated with the blocking anticyclone that formed over Scandinavia and subsequently moved westward toward Greenland during 29 July–1 August 2019.

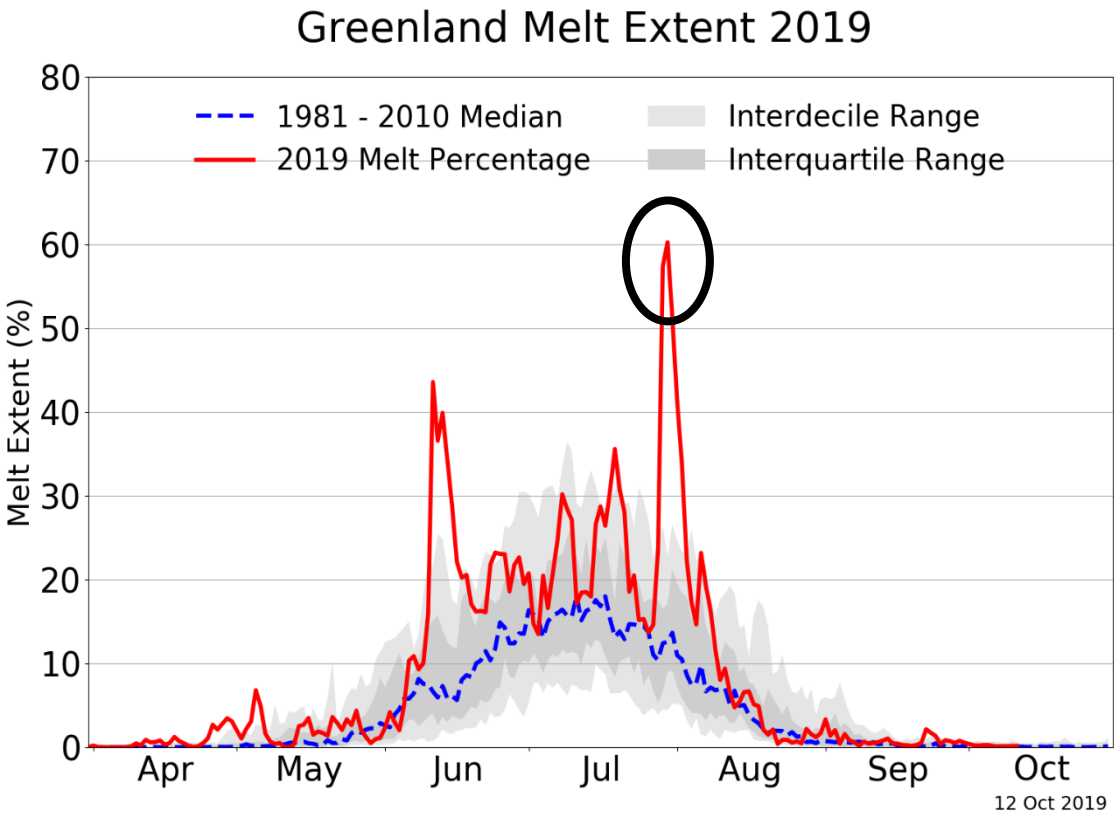

FIG. 4.1. Greenland ice melt extent (%) in 2019 (red solid line). Median (blue dashed line), interdecile range (light gray shading), and interquartile range (medium gray shading) for 1981–2010 climatology of Greenland ice-melt extent. The black circle denotes the late July–early August 2019 Greenland ice-melt event. Image source: NSIDC/Thomas Mote, University of Georgia; https://nsidc.org/greenland-today/greenland-surface-melt-extent-interactive-chart/.

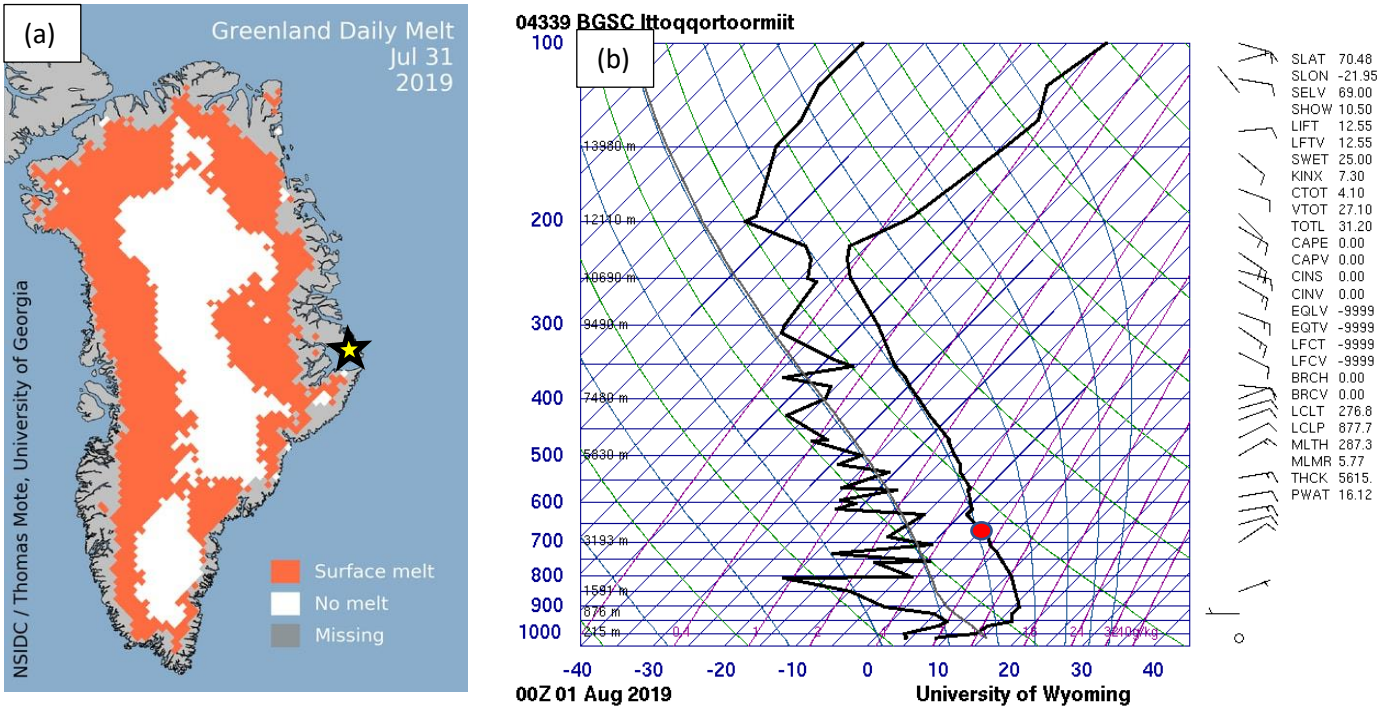

FIG. 4.2. (a) Greenland ice melt on 31 July 2019. The orange shading indicates where there was ice melt, and the white shading indicates where there was no ice melt. The yellow star indicates the location of Ittoqqortoormiit, Greenland. Image modified from NSIDC/Thomas Mote, University of Georgia; https://greenland-measures.labs.nsidc.org/. (b) Sounding from Ittoqqortoormiit, Greenland, at 0000 UTC 1 August 2019. The red dot indicates the pressure level where the temperature is 0°C. Image modified from University of Wyoming: http://weather.uwyo.edu/upperair/sounding.html.

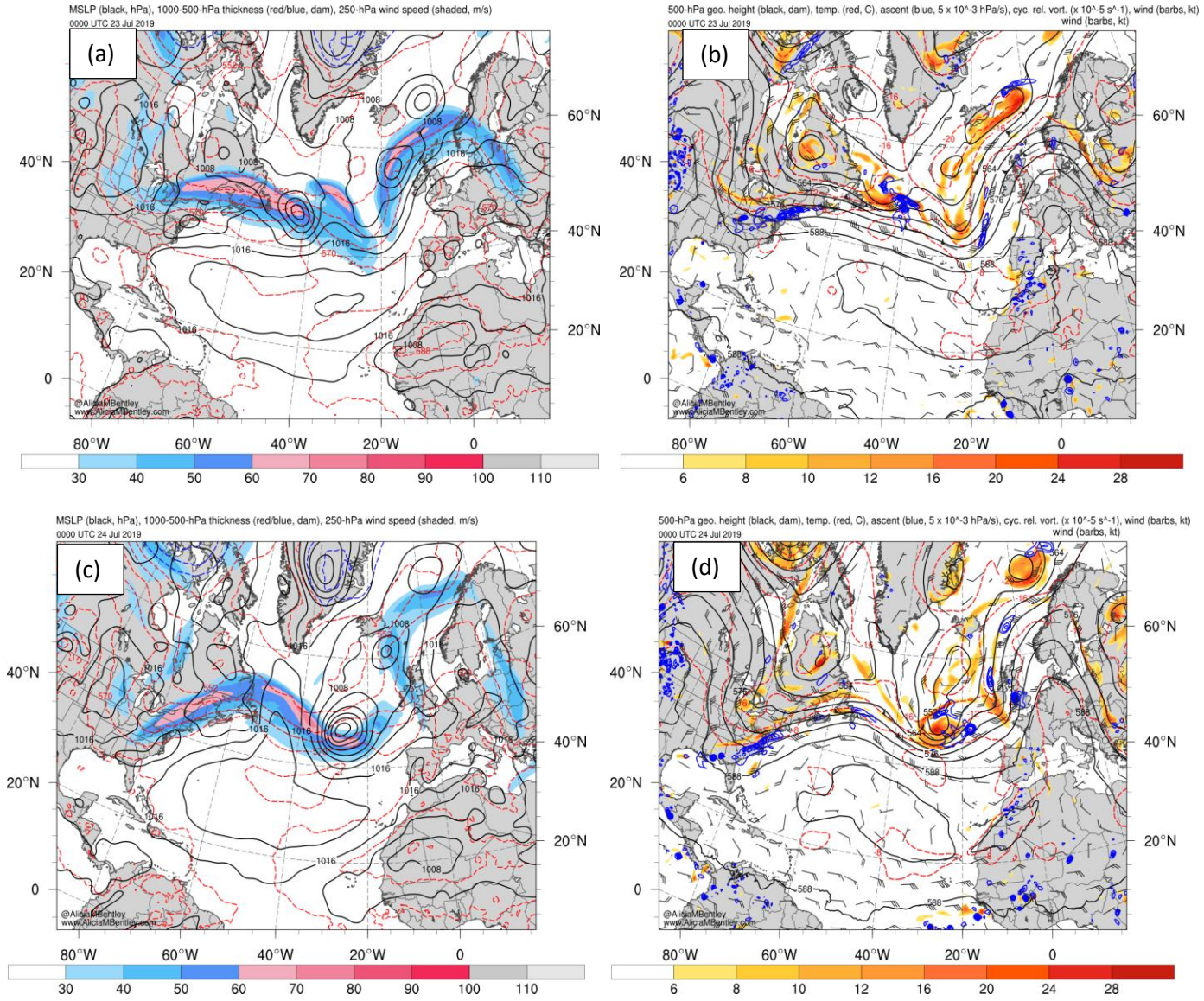

FIG. 4.3. (a) MSLP (hPa; black), 1000–500-hPa thickness (<540 dam; blue and >540 dam; red), and 250-hPa wind speed (m s^{-1}, shaded) at 0000 UTC 23 July 2019. (b) 500-hPa geopotential height (dam; black), temperature (°C; red), ascent (5×10^{-3} hPa s^{-1}; blue), cyclonic relative vorticity (10^{-5} s^{-1}, shaded), and wind (kt, barbs) at 0000 UTC 23 July 2019. (c) As in (a), except at 0000 UTC 24 July 2019. (d) As in (b), except at 0000 UTC 24 July 2019.

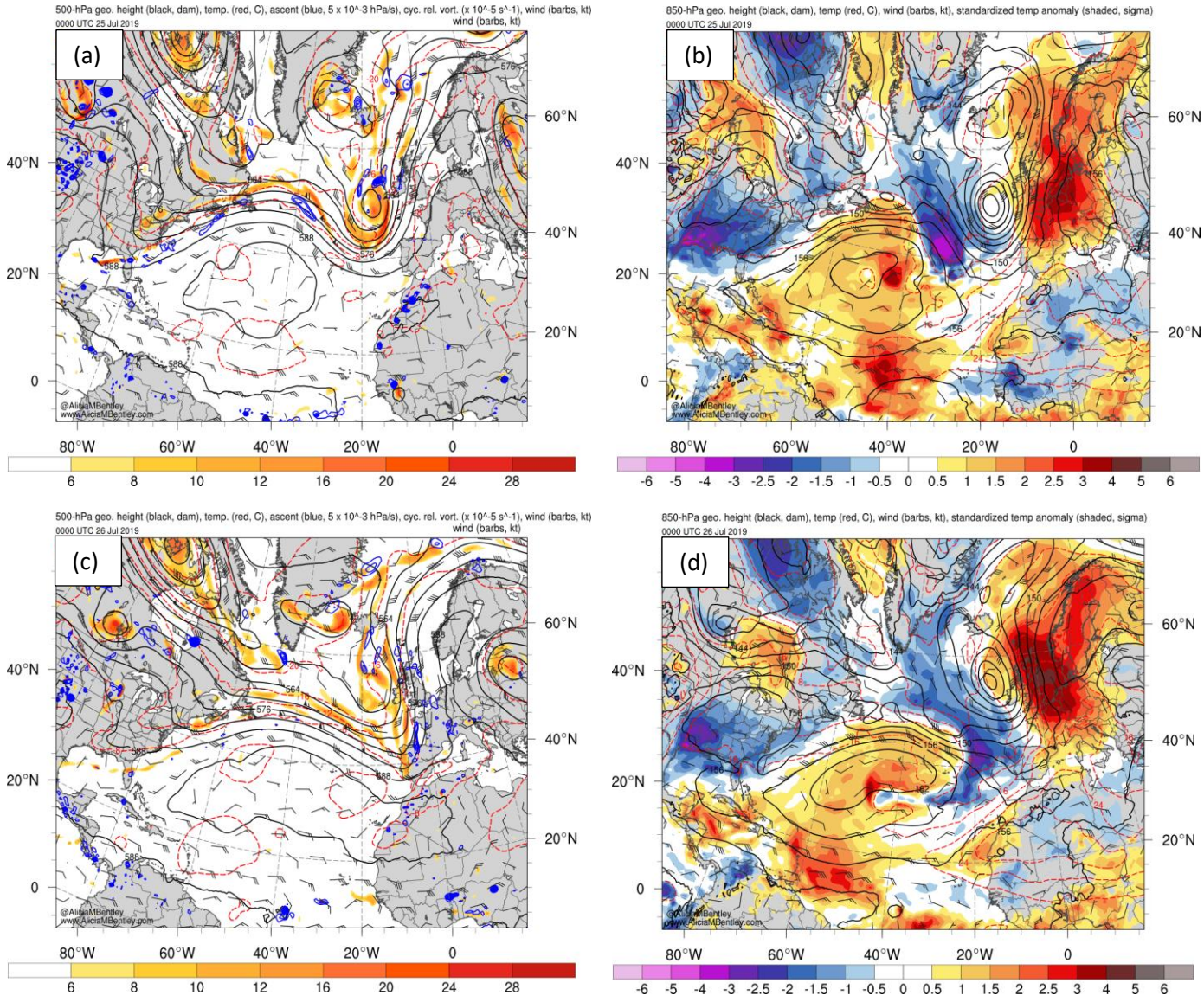

FIG. 4.4. (a) 500-hPa geopotential height (dam; black), temperature (°C; red), ascent (5×10^{-3} hPa s^{-1}; blue), cyclonic relative vorticity (10^{-5} s^{-1}, shaded), and wind (kt, barbs) at 0000 UTC 25 July 2019. (b) 850-hPa geopotential height (dam; black), temperature (°C; red), wind (kt, barbs), and standardized temperature anomaly (σ, shaded) at 0000 UTC 25 July 2019. (c) As in (a), except at 0000 UTC 26 July 2019. (d) As in (c), except at 0000 UTC 26 July 2019.

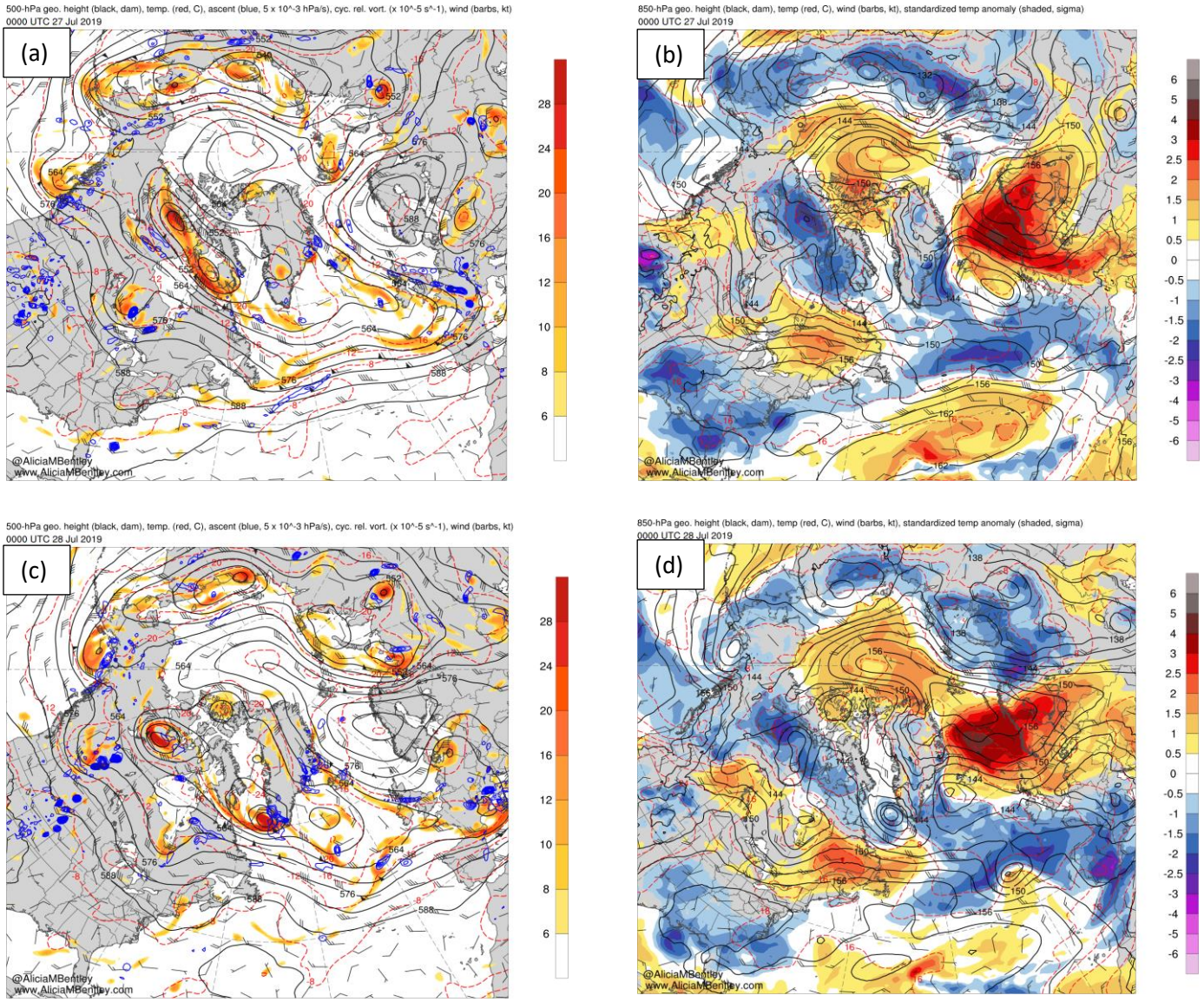

FIG. 4.5. (a) 500-hPa geopotential height (dam; black), temperature (°C; red), ascent (5×10^{-3} hPa s^{-1}; blue), cyclonic relative vorticity (10^{-5} s^{-1}, shaded), and wind (kt, barbs) at 0000 UTC 27 July 2019. (b) 850-hPa geopotential height (dam; black), temperature (°C; red), wind (kt, barbs), and standardized temperature anomaly (σ, shaded) at 0000 UTC 27 July 2019. (c) As in (a), except at 0000 UTC 28 July 2019. (d) As in (c), except at 0000 UTC 28 July 2019.

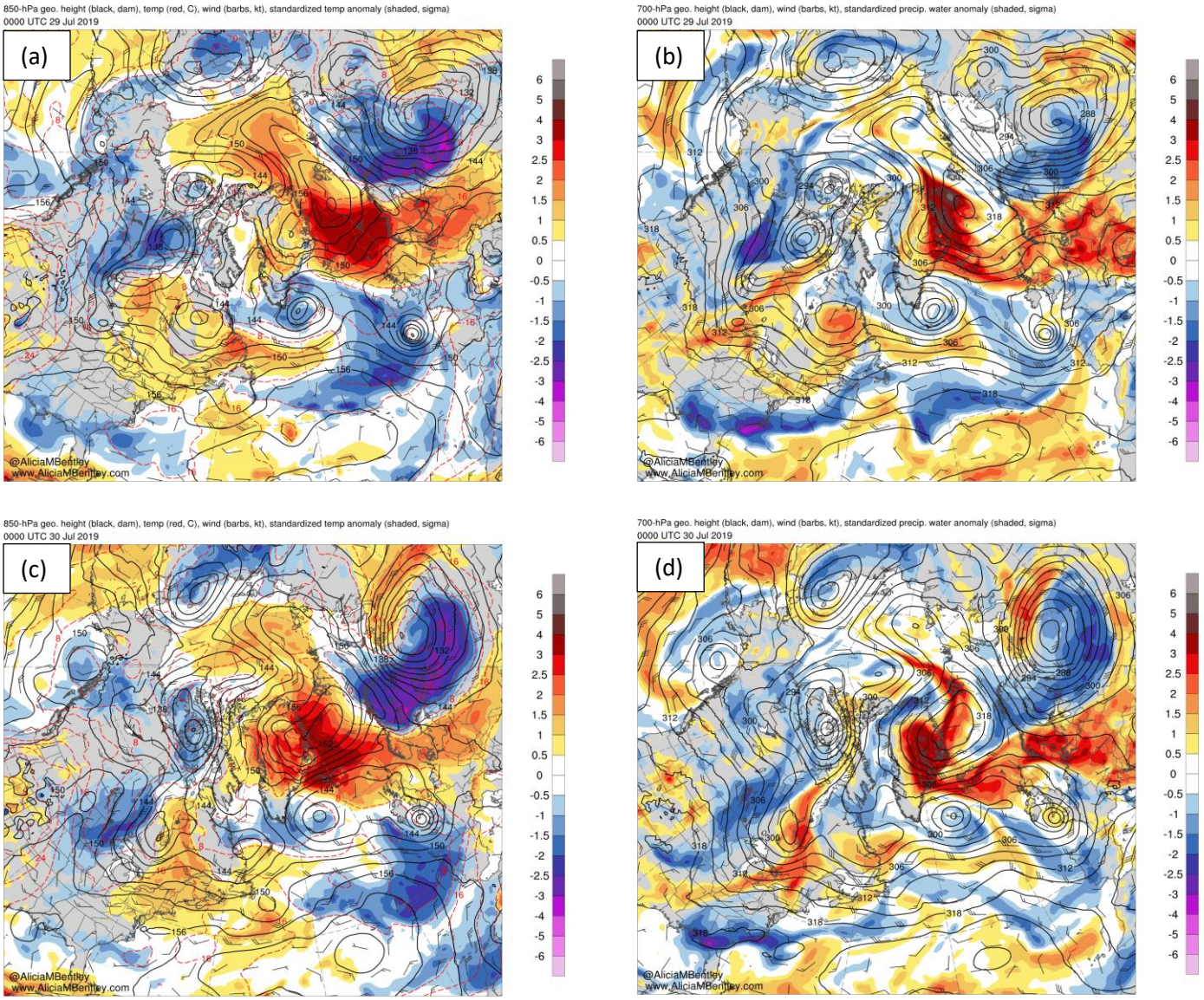

FIG. 4.6. (a) 850-hPa geopotential height (dam; black), temperature (°C; red), wind (kt, barbs), and standardized temperature anomaly (σ, shaded) at 0000 UTC 29 July 2019. (b) 700-hPa geopotential height (dam; black), wind (kt, barbs), and standardized precipitable water anomaly (σ, shaded) at 0000 UTC 29 July 2019. (c) As in (a), except at 0000 UTC 30 July 2019. (d) As in (c), except at 0000 UTC 30 July 2019.

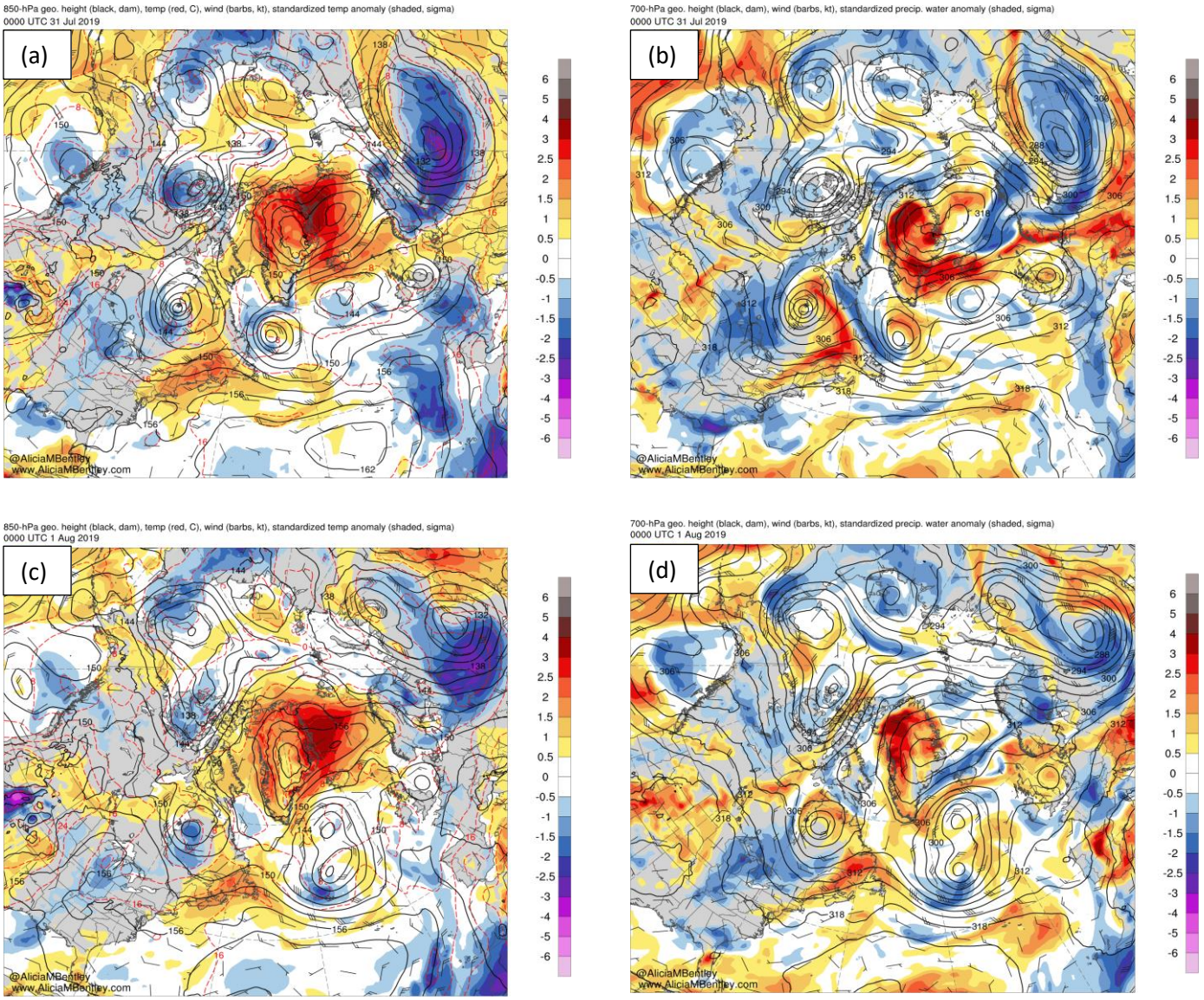

FIG. 4.7. (a) 850-hPa geopotential height (dam; black), temperature (°C; red), wind (kt, barbs), and standardized temperature anomaly (σ, shaded) at 0000 UTC 31 July 2019. (b) 700-hPa geopotential height (dam; black), wind (kt, barbs), and standardized precipitable water anomaly (σ, shaded) at 0000 UTC 31 July 2019. (c) As in (a), except at 0000 UTC 1 August 2019. (d) As in (c), except at 0000 UTC 1 August 2019.

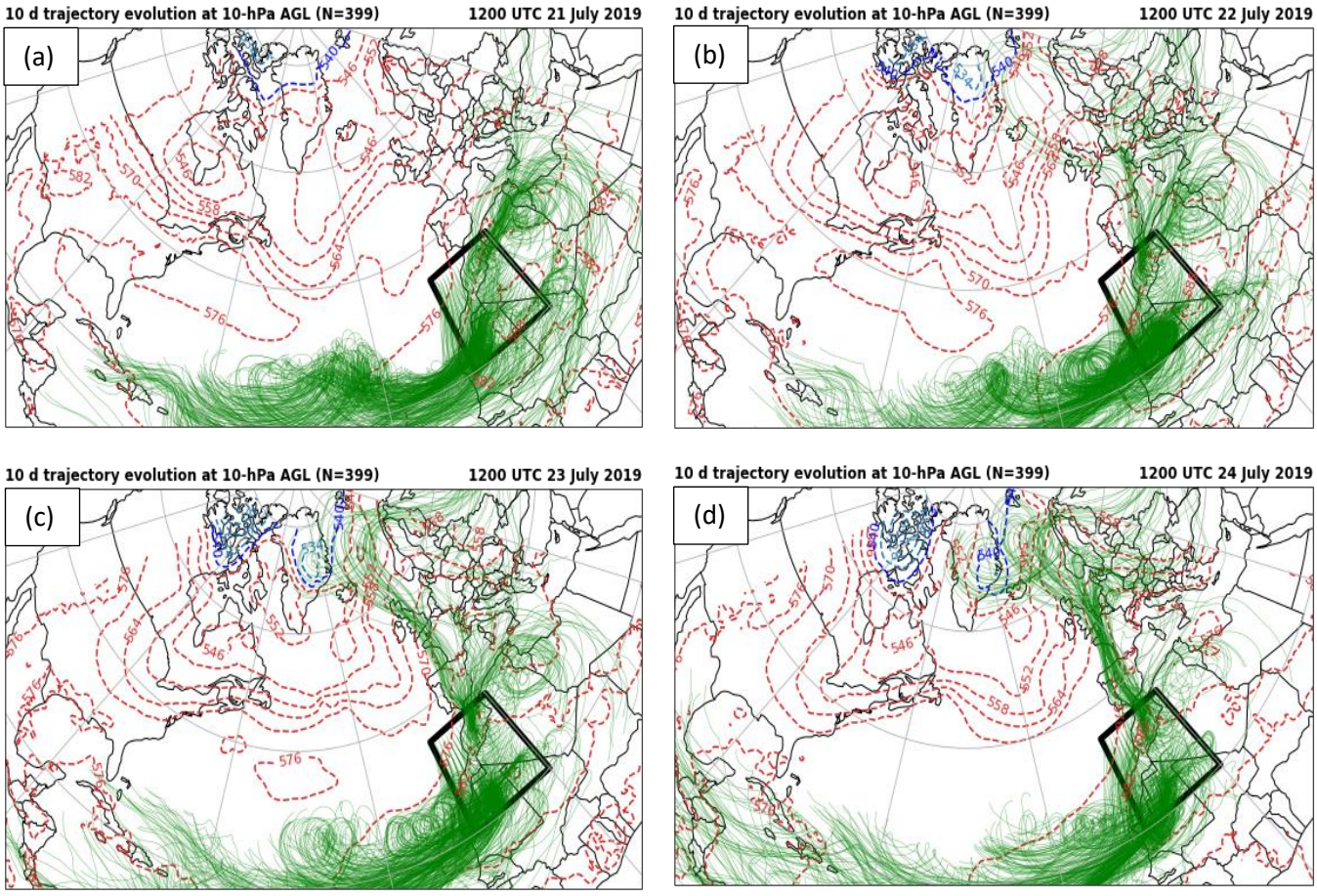

FIG. 4.8. (a) 10-d forward air parcel trajectories (green lines) for the African domain (black polygon) initialized at 10-hPa AGL and at 1200 UTC 21 July 2019. 1000–500-hPa thickness (<540 dam; light blue; 540 dam; dark blue and >540 dam; red) is overlaid and is valid at 1200 UTC 21 July 2019. (b) As in (a), except at 1200 UTC 22 July 2019. (c) As in (a), except at 1200 UTC 23 July 2019. (d) As in (a), except at 1200 UTC 24 July 2019.

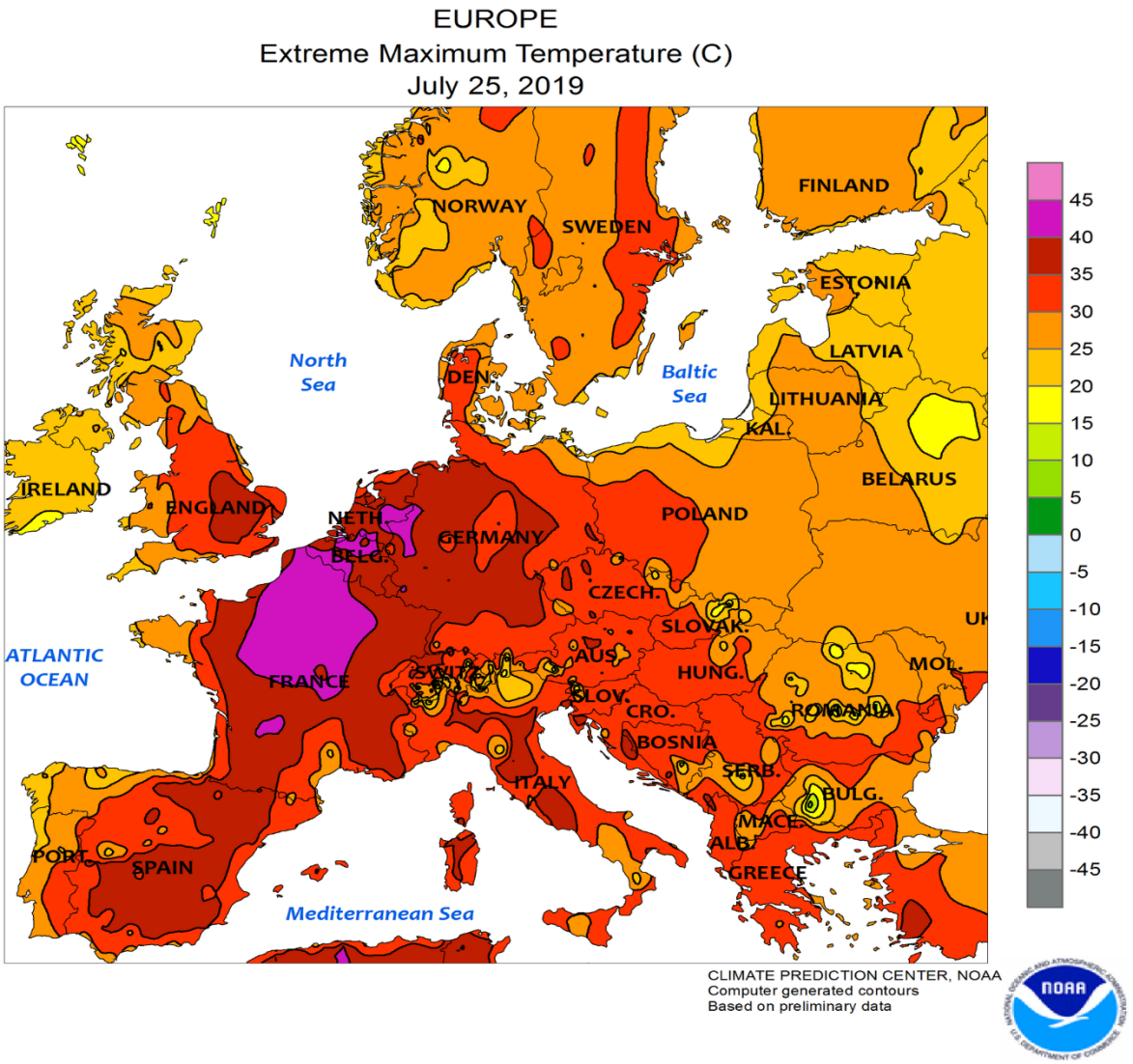

FIG. 4.9. Maximum temperatures (°C) over Europe on 25 July 2019. Image source: Climate Prediction Center, NOAA; https://www.cpc.ncep.noaa.gov/.

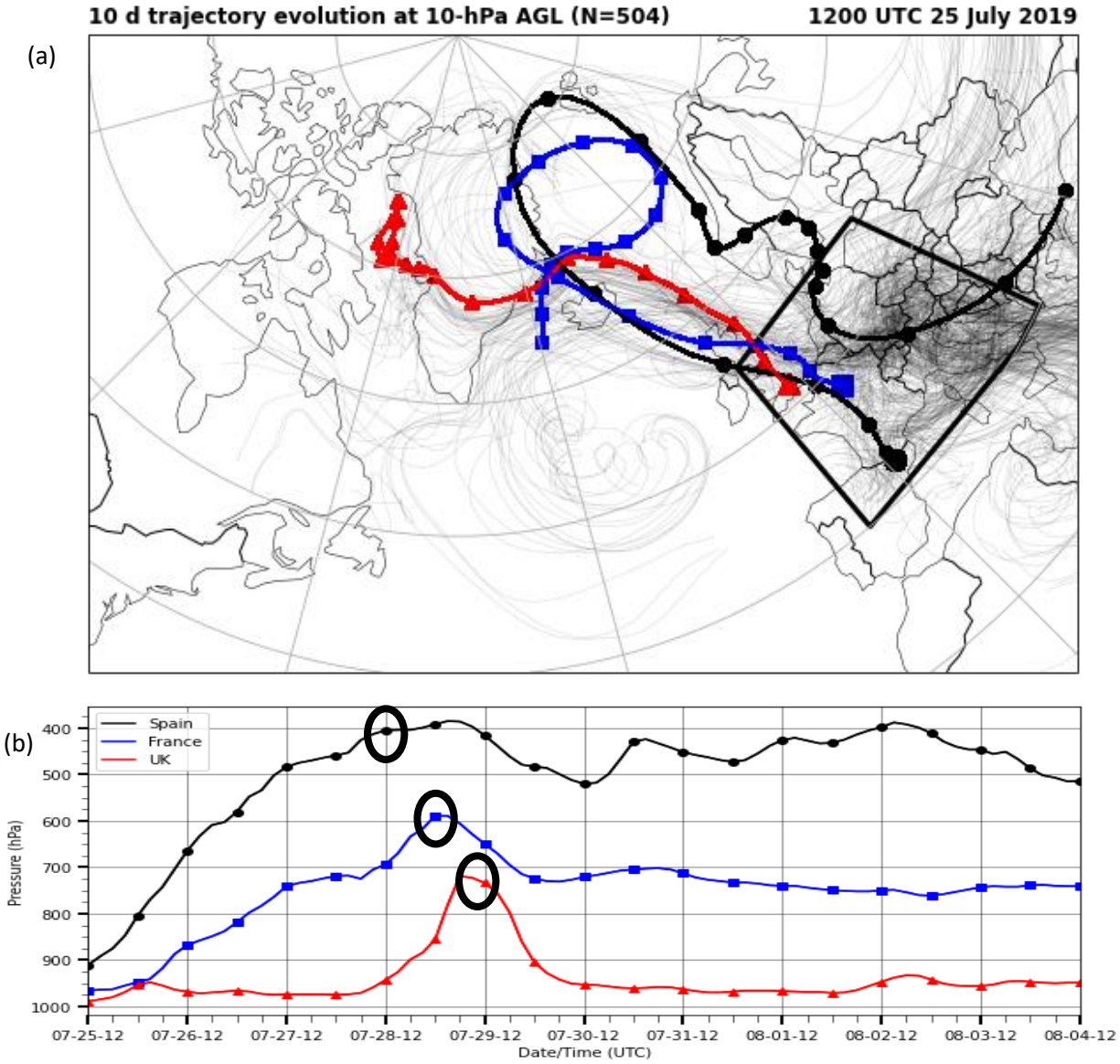

FIG. 4.10. (a) 10-d forward air parcel trajectories (thin black lines) for the European domain (black polygon) initialized at 10-hPa AGL and at 1200 UTC 25 July 2019. Forward air parcel trajectories of interest are initialized at 1200 UTC 25 July 2019 from Spain (black line and circles), France (blue line and squares), and the United Kingdom (red line and triangles). Each symbol (i.e., circle, square, triangle) delineates the forward air parcel trajectories of interest at 12-h intervals. (b) Time series of pressure (hPa) for the three forward air parcel trajectories of interest initialized from Spain (black line and circles), France (blue line and squares), and United Kingdom (red line and triangles). The large black circles denote the approximate time the air parcels approximately first reached Greenland.

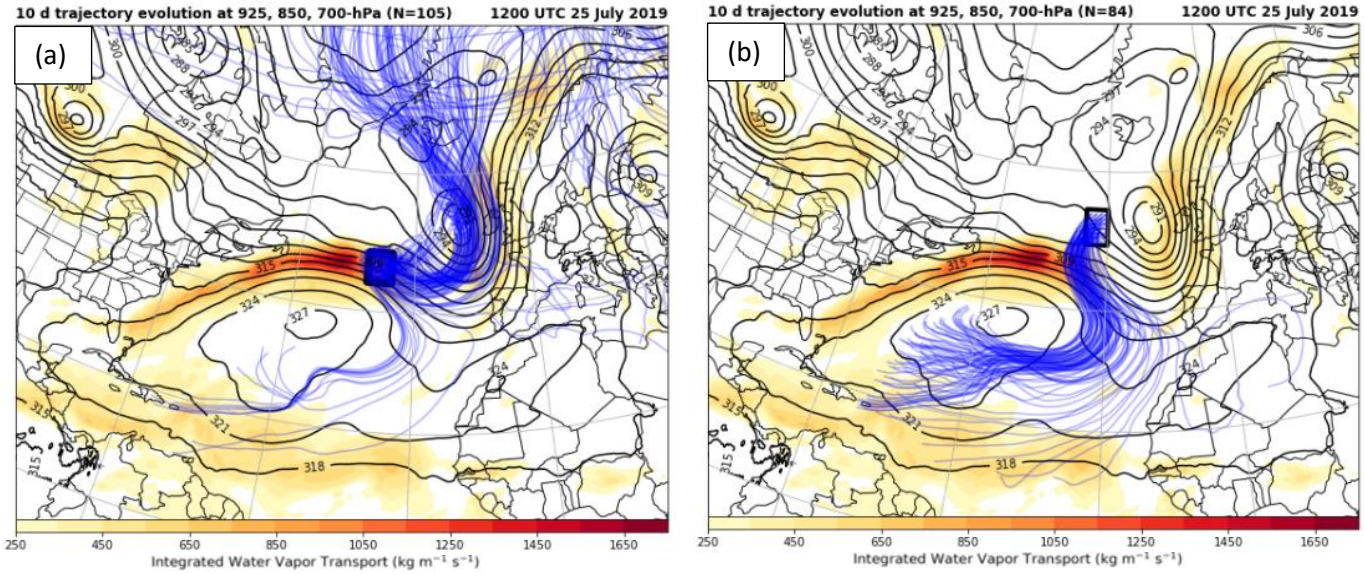

FIG. 4.11. (a) 10-d forward air parcel trajectories (blue lines) for the North Atlantic Ocean domain (black polygon) initialized at 925, 850, and 700 hPa and at 1200 UTC 25 July 2019 over an AR and south of a jet core at 500 hPa. 700-hPa geopotential height (dam; black) and IVT (kg $m^{-1} s^{-1}$; shaded) are overlaid and are valid at 1200 UTC 25 July. (b) As in (a), except the 10-d forward air parcel trajectories are initialized north of the AR and the jet core at 500 hPa.

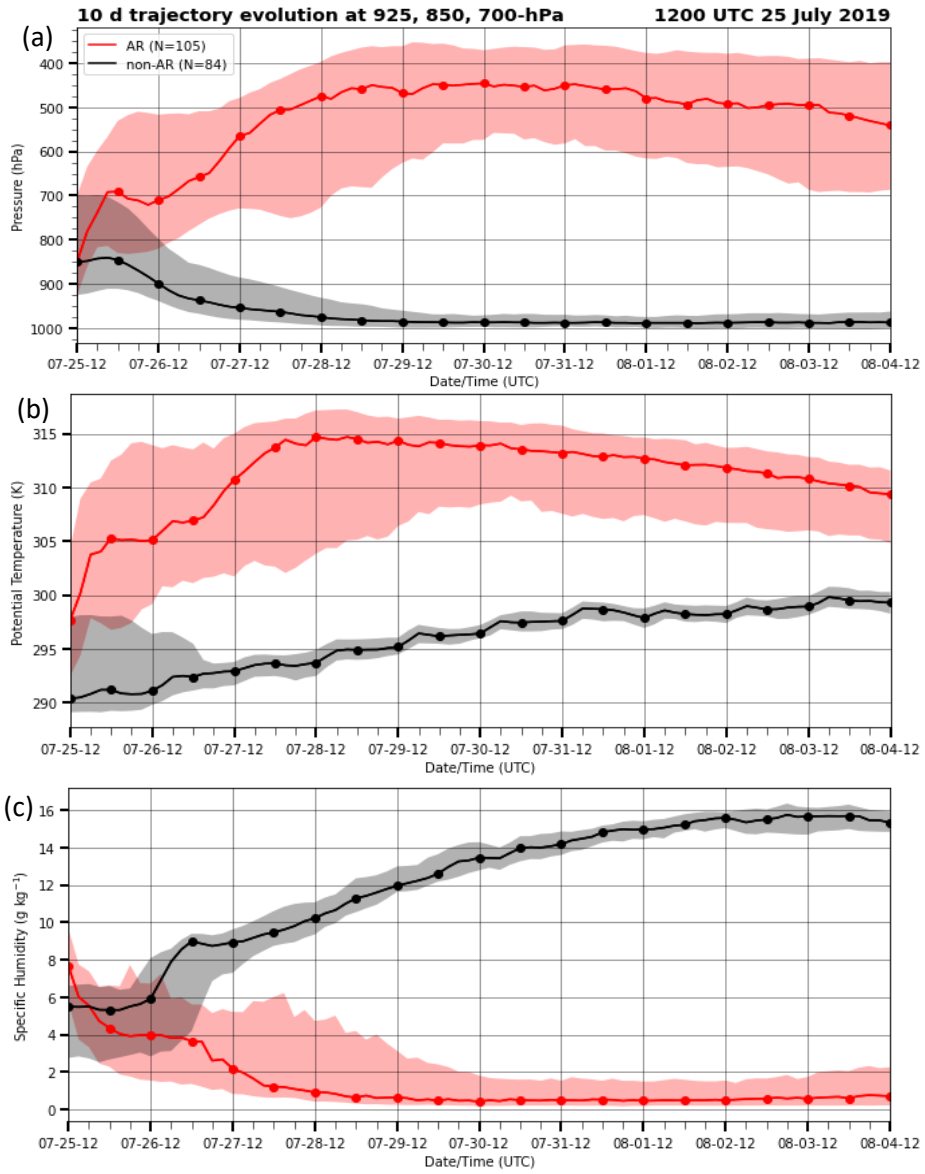

FIG. 4.12. Time series of (a) pressure (hPa), (b) potential temperature (K), and specific humidity (g kg^{-1}) for the 10-d forward air parcel trajectories for the North Atlantic Ocean domain initialized at 925, 850, and 700 hPa and at 1200 UTC 25 July 2019. The red lines represent the median of each variable for the forward air parcel trajectories initialized over the AR and south of the jet core at 500 hPa from Fig. 4.11a, and the black lines represent the median of each variable for the forward air parcel trajectories initialized north of the AR and the jet core at 500 hPa from Fig. 4.11b. The black and red dots represent the median of each variable for the forward air parcel trajectories at 12-h intervals. The red shading indicates the interquartile range of each variable for the forward air parcel trajectories over the AR and south of the jet core at 500 hPa, and the gray shading indicates the interquartile range of each variable for the forward air parcel trajectories initialized north of the AR and the jet core at 500 hPa.

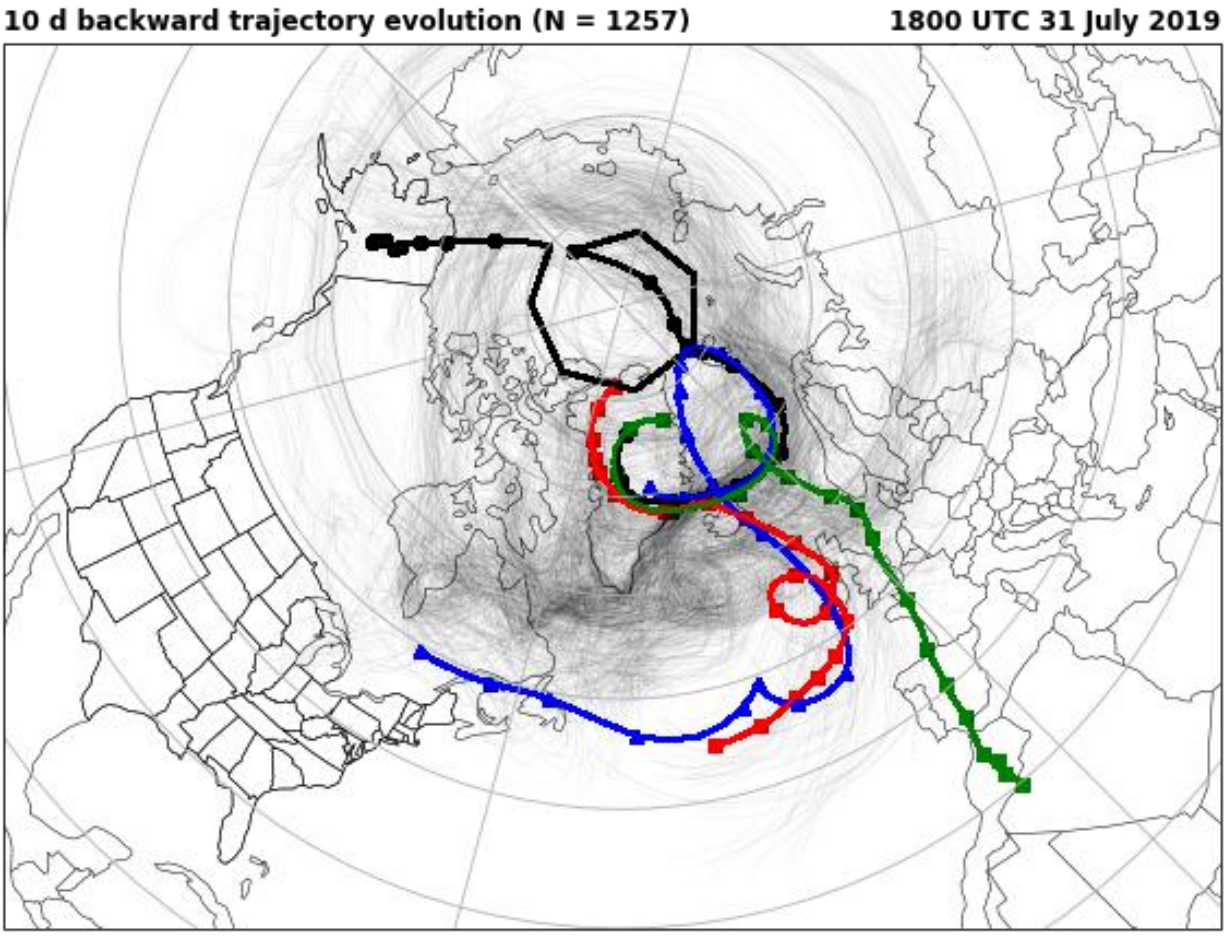

FIG. 4.13. 10-d backward air parcel trajectories (light black lines) for the Greenland domain initialized at 925, 850, 700, 600, and 500 hPa and at 1800 UTC 31 July 2019. Backward air parcel trajectories of interest are initialized at 1800 UTC 31 July 2019 and originate from Alaska (black line and circles), Quebec (blue line and triangles), the eastern North Atlantic Ocean (red line and squares), and northwest Africa (green line and squares), respectively. Each symbol (i.e., circle, square, triangle) delineates the backward air parcel trajectories of interest at 12-h intervals.

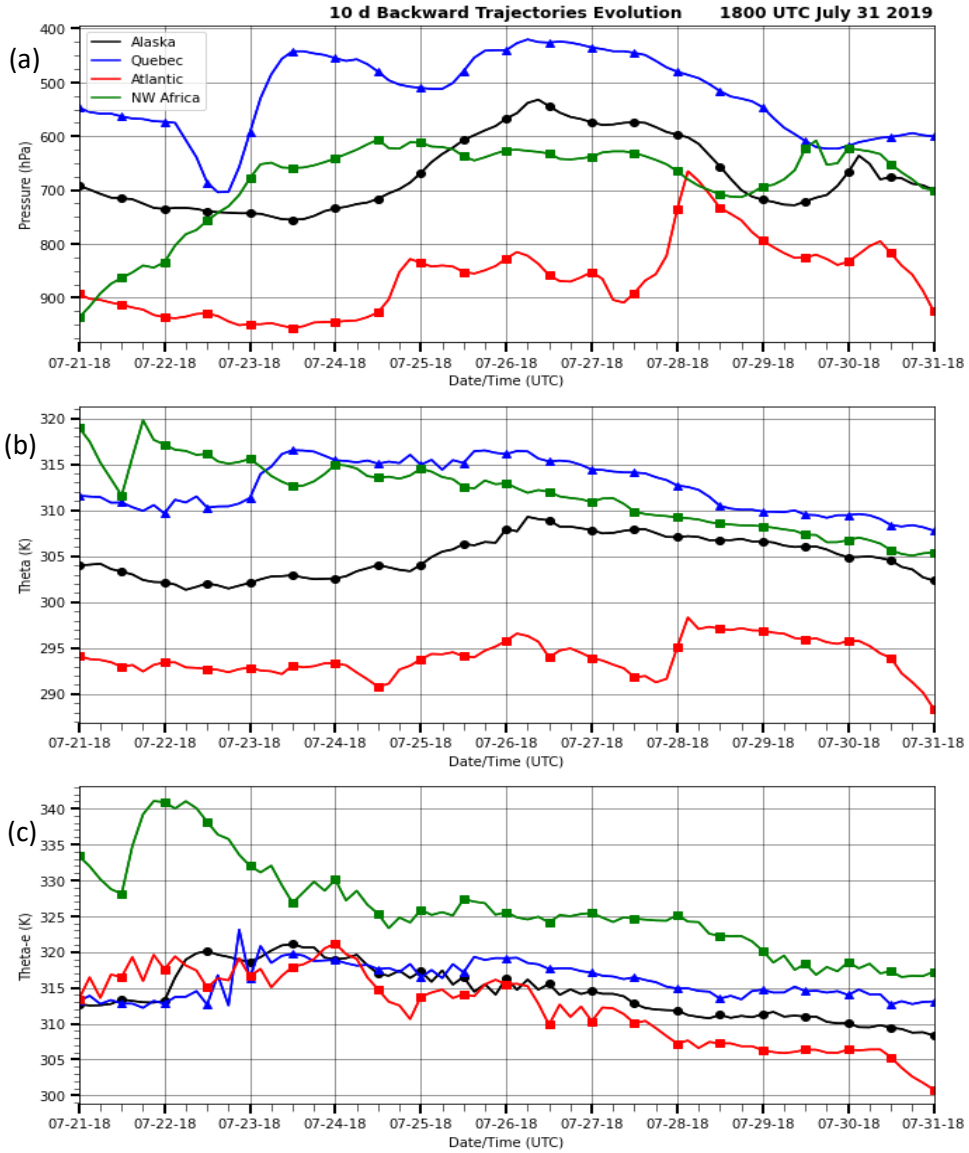

FIG. 4.14. Time series of (a) pressure (hPa), (b) potential temperature (K), and equivalent potential temperature (K) for the 10-d backward air parcel trajectories of interest from Fig. 4.13 for the Greenland domain initialized at 1800 UTC 31 July 2019. The black lines represent the backward air parcel trajectory originating from Alaska, the blue lines represent the backward air parcel trajectory originating from Quebec, the red lines represent the backward air parcel trajectory originating from the eastern North Atlantic Ocean, and the green lines represent the backward air parcel trajectory originating from northwest Africa. Each symbol (i.e., circle, square, triangle) delineates the backward parcel trajectories of interest at 12-h intervals.

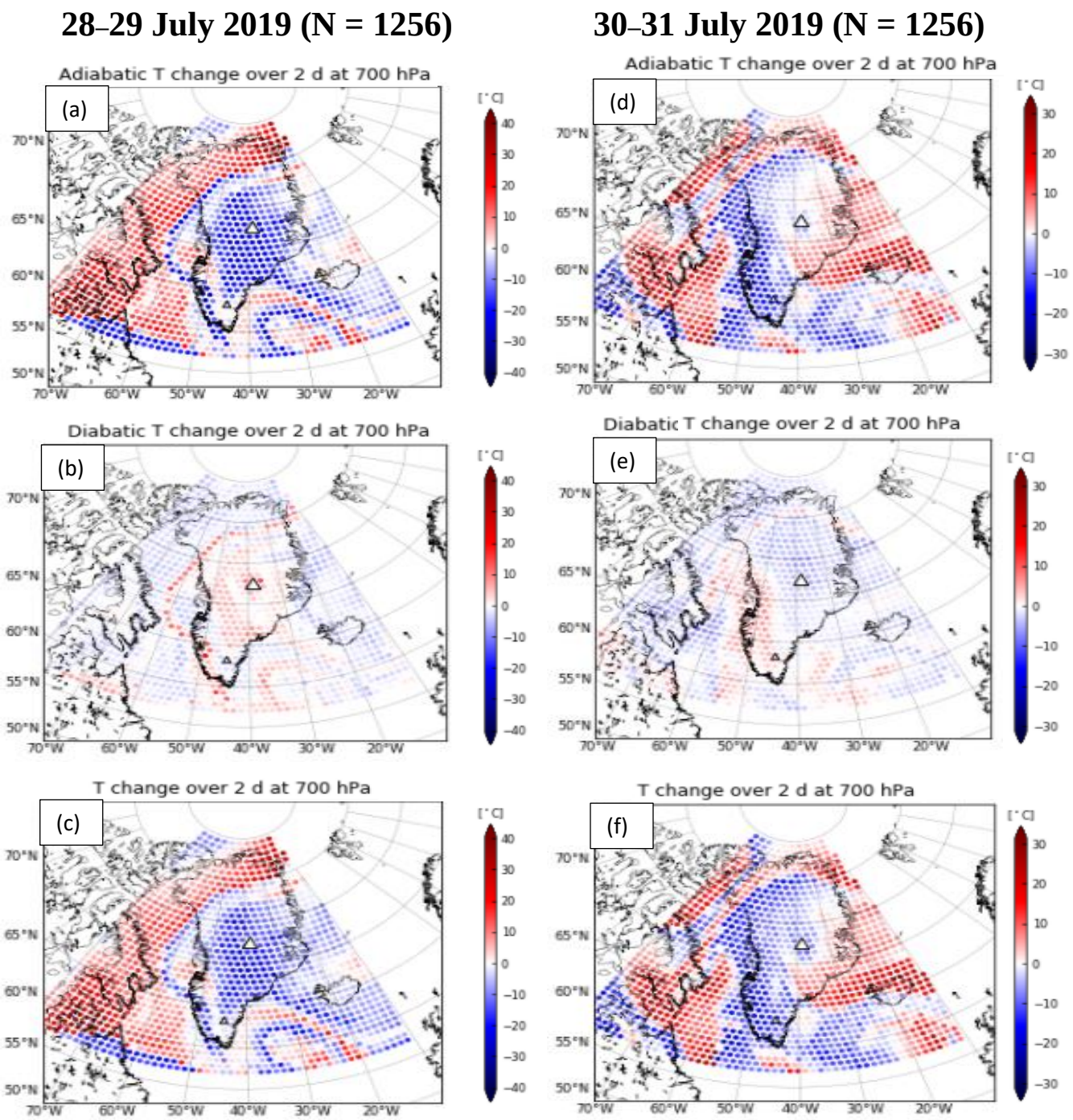

FIG. 4.15. The sum of the (a) adiabatic temperature change (°C), (b) diabatic temperature change (°C), and (c) temperature change (°C) for every backward air parcel trajectory arriving every 6 h over 2 d at 700 hPa over the Greenland domain during 0000 UTC 28–1800 UTC 29 July 2019. Summit Station and the South Dome are denoted by large and small triangles, respectively. Panels (d), (e), and (f) are the same as (a), (b), and (c) except during 0000 UTC 30–1800 UTC 31 July 2019.

5. Summary and Suggestions for Future Work

The goals of this research were to: 1) identify and analyze the synoptic flow patterns that may contribute to anomalous ice melt over Greenland on daily to weekly time scales by creating a climatology of Greenland ice-melt events during April–October 1979–2019 using SOMs; 2) explore seasonal variations in the synoptic flow patterns that may contribute to anomalous ice melt by comparing summer and fall/spring Greenland ice-melt events using SOMs; 3) improve understanding of how extratropical cyclones and/or short-wave disturbances can reinforce Greenland blocking through upper-level flow amplification using a representative case study; 4) identify and analyze the source of air masses that may contribute to Greenland ice-melt events using air parcel trajectory analysis; 5) quantify the contribution of adiabatic warming due to synoptic-scale descent associated with Greenland blocking in facilitating ice melt using air parcel trajectory analysis; and 6) quantify the contribution of diabatic warming due to condensation and latent heating over Greenland in facilitating ice melt using air parcel trajectory analysis. Although numerous studies have constructed synoptic climatologies of Greenland ice-melt events during the summer months, very few studies have constructed synoptic climatologies of Greenland ice-melt events that includes the spring, summer, and fall months. This thesis set out to better understand the underlying dynamical and diabatic processes that may contribute to Greenland ice melt by investigating Greenland ice-melt events from both climatological and case-study perspectives.

5.1 Climatology

In order to classify synoptic flow patterns that contribute to Greenland ice melt, this thesis utilized SOMs, a type of artificial neural network that clusters data points into various nodes according to the similarity between the synoptic flow patterns. A synoptic climatology of Greenland ice-melt events was constructed using ERA5 reanalysis data at 0.25° resolution for the April–October 1979–2019 time period. The ERA5 reanalysis data was re-gridded to 1° resolution to render the data compatible with the SOMs algorithm used in this thesis. Greenland ice-melt events were defined as days during the April–October 1979–2019 time period where the

Greenland ice-melt extent was at or above the 90th percentile compared to the climatology developed by the NSIDC. 500-hPa geopotential height and SLP data were entered into the SOMs algorithm separately where the Greenland ice-melt event criterion was met to construct single-variable SOMs analyses. 700-hPa geopotential height and IVT data, as well as SLP and 1000–500-hPa thickness data, were entered into the SOMs algorithm together where the Greenland ice-melt criterion was met to construct multivariate SOMs analyses. A 4 × 3 (i.e., 4 columns × 3 rows) SOMs size was chosen with the expectation that the selected size displays the full range of variability in the synoptic flow patterns. The average of the aforementioned variables was computed for the Greenland ice-melt events and placed into each node produced by the SOMs algorithm over a Greenland domain.

The SOM-based analysis procedure identified 966 Greenland ice-melt events that occurred during the April–October 1979–2019 time period, which were broken down by year and month. A total of 930 Greenland ice-melt events were identified during the April–October 1979–2018 time period. These 930 Greenland ice-melt events were broken down into a histogram by decade. As discussed in section 3.1, Greenland ice-melt events are becoming more frequent with time. For example, there were 42 Greenland ice-melt events during 1979–1988, while there were 439 Greenland ice-melt events during 2010–2019. The increase in frequency of Greenland ice-melt events with time may be due to strong blocking patterns and poleward moisture transport over Greenland becoming more frequent (e.g., Fettweis et al. 2011, 2013; Overland et al. 2012; Neff et al. 2014; Mattingly et al. 2016). The top 3 months with the highest frequency of Greenland ice-melt events (i.e., July had 170 ice-melt events, June had 163 ice-melt events, and August had 132 ice-melt events) all occurred during the summer ice-melt season.

As discussed in section 3.2, the SOMs algorithm showed that a common flow pattern during Greenland ice-melt events was an upper-level ridge axis that can be located west of, over, or east of Greenland. A large percentage of Greenland ice-melt events occurred with a strong ridge over Greenland that was part of an omega block irrespective of whether the upstream or downstream troughs were strong or weak. Summer Greenland ice-melt events often occurred in conjunction with a strong blocking pattern over Greenland with strong positive standardized 500-hPa geopotential height anomalies as high as 1.5–2σ compared to climatology. The previous finding is consistent with that of Mioduszewski et al. (2016), who concluded that positive 500-

hPa geopotential height anomalies near Greenland coincide with large positive ice-melt anomalies over Greenland during the summer months. Spring and fall Greenland ice-melt events often occurred in conjunction with a negatively tilted trough upstream of Greenland, with negative standardized 500-hPa geopotential height anomalies over western Greenland. Negatively tilted troughs allow for the substantial poleward transport of warm and moist air masses from lower latitudes. Warm and moist air masses from lower latitudes can help facilitate Greenland ice melt during the spring and fall months, which tend to be colder months climatologically than the summer months.

Greenland ice-melt events were associated with both positive and negative standardized SLP anomalies over Greenland, as well as semipermanent climatological standardized SLP anomalies that were located west (e.g., the Beaufort high) and east (e.g., the Icelandic low and Azores high) of Greenland. Greenland ice-melt events were associated with strong blocking anticyclones and low IVT over Greenland, and with deep troughs upstream of Greenland and high IVT over Greenland. The eastern flanks of strong blocking anticyclones over Greenland can induce Greenland ice melt due to warm and dry air over Greenland that undergoes synoptic-scale descent. Deep troughs upstream of Greenland can induce Greenland ice melt due to the advection of warm and moist air over Greenland by southerly flow downstream of the trough axis. Summer Greenland ice-melt events often occurred in conjunction with a strong blocking anticyclone over Greenland with low IVT over Greenland. Spring and fall Greenland ice-melt events often occurred in conjunction with a negatively tilted trough over eastern North America and the western North Atlantic Ocean with high IVT over southern Greenland.

Greenland ice-melt events were associated with thickness troughs upstream and downstream of Greenland, and with varying standardized SLP anomalies over Greenland. The 540-dam thickness contour can be used as a proxy to distinguish between where snow or rain is more likely at lower elevations along the boundaries of the Greenland ice sheet. Summer Greenland ice-melt events occurred in conjunction with positive and negative standardized SLP anomalies over Greenland, with the 540-dam thickness contour located north of Greenland in the warmest nodes. Spring and fall Greenland ice-melt events occurred in conjunction with positive and negative standardized SLP anomalies over Greenland, with the 540-dam thickness contour

over southern Greenland, as well as eastern North America and extending eastward over the North Atlantic Ocean, in the coldest nodes.

5.2 Case Study

The late July–early August 2019 Greenland ice-melt event was chosen for analysis in order to investigate a record-breaking summer Greenland ice-melt event that was associated with an AR over the North Atlantic Ocean, a record-breaking heat wave over Europe, and a strong blocking anticyclone over Scandinavia that moved westward toward Greenland. As discussed in section 4.1.1, gridded 0.5° CFSR analyses were used to construct analyses of the synoptic flow patterns for this Greenland ice-melt event. During late July–early August 2019, 60% (i.e., ~984,000 km^2) of the Greenland ice sheet experienced melting, which is the largest ice melt over Greenland since at least 2012. Ice melt over Greenland was associated with a blocking anticyclone over Scandinavia that subsequently shifted westward toward Greenland and permitted anomalously warm air of Saharan origin to reach Greenland. Upper-level flow amplification from eastern North America to western Europe resulted in ridge amplification over northwest Africa, which occurred in conjunction with the formation of an AR over the North Atlantic Ocean that was associated with a large poleward-directed moisture transport. Anomalously warm air of Saharan origin was able to reach western Europe and Scandinavia, resulting in a record-breaking heat wave over Europe as the ridge over northwest Africa extended poleward and subsequently evolved into the blocking anticyclone over Scandinavia. The AR subsequently transitioned into a westward-directed moisture transport toward Greenland in conjunction with a westward shift of the blocking anticyclone over Scandinavia toward Greenland.

Air parcel trajectories were computed to analyze the modifications of the air masses that contributed to the late July–early August 2019 Greenland ice-melt event and to identify their respective source origins. Forward air parcel trajectories were calculated for 10 days every 3 h from a European, North Atlantic Ocean, and African domain starting at 10, 30 and 50 hPa AGL and separated equidistantly every 80 km horizontally. Backward air parcel trajectories were calculated from a Greenland domain for 10 days every 3 h starting at 925, 850, 700, 600, and 500

hPa and separated equidistantly every 80 km horizontally. There were 986 backward air parcel trajectories starting at 925 hPa and 1060 backward air parcel trajectories starting at 850 hPa over the Greenland domain, while there were 1275 backward air parcel trajectories for each pressure level starting at 700, 600, and 500 hPa over the Greenland domain. The differences in the number of air parcel trajectories at the respective pressure levels was determined by what percentage of the area of each grid box was below ground. Backward air parcel trajectories starting at 925 and 850 hPa were used to analyze air parcels that started over coastal Greenland and offshore of Greenland, while backward air parcel trajectories starting at 700, 600, and 500 hPa were used to analyze air parcels that started over inland regions of Greenland. Selected ERA-Interim variables (i.e., pressure, temperature, potential temperature, and specific humidity) were traced along the air parcel trajectories.

As discussed in section 4.1.2, forward air parcel trajectories were initialized in an African domain to determine whether anomalously warm air over northwest Africa during 21–24 July 2019 subsequently reached Greenland. Air parcels initialized during 1200 UTC 22–24 July 2019 over the northwest African domain moved northward in conjunction with the poleward extension of the ridge over northwest Africa toward Scandinavia. Forward air parcel trajectories were initialized in a European domain in order to investigate the connection between the late July–early August 2019 Greenland ice-melt event and a preceding late July 2019 European heat wave. Anomalously warm air over Europe during the peak of the late July 2019 European heat wave (i.e., when maximum temperatures over Europe exceeded 40°C) on 25 July 2019 was able to reach Greenland during the subsequent days. For example, an air parcel initialized near Paris, France, at 10 hPa AGL at 1200 UTC 25 July 2019 during the record-breaking European heat wave (e.g., Paris recorded an all-time maximum temperature of 42.6°C on 25 July) ascended from ~960 hPa to ~600 hPa as it first reached Greenland at approximately 0000 UTC 29 July 2019.

Forward air parcel trajectories were initialized at 1200 UTC 25 July 2019 in a North Atlantic Ocean domain in order to trace the pathways of air parcels moving through the AR over the North Atlantic Ocean and to quantify the contribution of diabatic warming due to condensation and latent heat release within this AR. Air parcels initialized in this AR first moved poleward in conjunction with the poleward extension of the ridge over northwest Africa toward

Scandinavia and then moved westward toward Greenland in conjunction with the westward shift of the blocking anticyclone over Scandinavia toward Greenland. Moist ascending air parcels initialized in the AR over the North Atlantic Ocean experienced a median specific humidity decrease from ~8 g kg^{-1} to ~1 g kg^{-1} and a median potential temperature increase from ~298 K to ~315 K as these air parcels ascended from ~850 hPa to ~480 hPa during the 72-h period ending on 1200 UTC 28 July 2019. These respective changes in median specific humidity and median potential temperature are indicative of condensation and latent heat release over Greenland, such that the associated diabatic warming may have contributed to Greenland ice melt during this event.

A Lagrangian evaluation of the thermodynamic energy equation (as described in section 2.2) was utilized in order to quantify the respective contributions of adiabatic and diabatic processes to temperature changes along every backward air parcel trajectory arriving every 6 h at 925, 850, 700, 600, and 500 hPa over the Greenland domain (i.e., inland and coastal regions of Greenland, and offshore of Greenland). The temperature changes, along with their adiabatic and diabatic contributions, were summed up during the 0000 UTC 28–1800 UTC 29 July 2019 time period and during the 0000 UTC 30–1800 UTC 31 July 2019 time period at 700 hPa. During 0000 UTC 28–1800 UTC 29 July 2019, there was diabatic warming over central Greenland that was maximized near Summit Station, and there was diabatic cooling over northern Greenland. The diabatic warming over central Greenland occurred in conjunction with the westward-directed moisture transport toward Greenland. It may be hypothesized that the diabatic warming over central Greenland during 0000 UTC 28–1800 UTC 29 July 2019 may be due to condensation and latent heating within the AR that originated over the North Atlantic Ocean on 25 July 2019, such that the associated diabatic warming may have contributed to Greenland ice melt during this time period. During 0000 UTC 30–1800 UTC 31 July 2019, there was strong adiabatic cooling over western and southern Greenland that was maximized near South Dome, and weak-to-moderate adiabatic warming over eastern Greenland. The weak-to-moderate adiabatic warming over eastern Greenland occurred in conjunction with the westward shift of the blocking anticyclone over Scandinavia toward Greenland. It may be hypothesized that the weak-to-moderate adiabatic warming over eastern Greenland may be indicative of synoptic-scale descent occurring on the eastern flank of this blocking anticyclone, such that the associated adiabatic warming may have contributed to Greenland ice melt during this time period.

5.3 Suggestions for Future Work

Greenland ice-melt events were shown to be most common (i.e., the nodes with the highest number of Greenland ice-melt events for each of the SOMs), when the patterns of 500-hPa geopotential height, SLP, 700-hPa geopotential height and IVT, as well as SLP and 1000–500-hPa thickness favored a strong blocking pattern over Greenland, low SLP over Baffin Bay and Greenland, a strong blocking anticyclone and low IVT over Greenland, and low SLP and a thickness trough upstream and downstream of Greenland with the 540-dam thickness contour over northern Greenland. These synoptic flow patterns that govern Greenland ice-melt events may be the most common because they allow for the transport of anomalously warm and moist air from lower latitudes toward Greenland. Future studies could consist of representative analyses of additional synoptic flow patterns that govern Greenland ice-melt events not explored in this thesis. For example, strong cyclones that track poleward and west of Greenland can transport anomalously warm and moist air on their eastern flanks toward Greenland. Analyses of events with poleward-moving cyclones that track poleward and west of Greenland are needed to better understand the synoptic-dynamic linkages between cyclones and Greenland ice-melt events.

Future studies could also further explore the similarities and differences between spring and fall, and summer Greenland ice-melt events. Summer Greenland ice-melt events may be more common and longer-lasting than Greenland ice-melt events during spring and fall because it is climatologically warmer during the summer than during spring and fall. During spring and fall, the upper-level flow in middle latitudes tends to be more amplified than during the summer, which may be associated with a higher occurrence of strong poleward heat and moisture transport toward Greenland. Additional analyses of both spring and fall, and summer Greenland ice-melt events are needed to explore the seasonality of the synoptic-scale flow evolution preceding and during Greenland ice-melt events.

REFERENCES

Baggett, C., S. Lee, and S. Feldstein, 2016: An investigation of the presence of atmospheric rivers over the North Pacific during planetary-scale wave life cycles and their role in Arctic warming. *J. Atmos. Sci.*, **73**, 4329–4347, https://doi.org/10.1175/JAS-D-16-0033.1.

Barnes, E. A., and D. L. Hartmann, 2012: Detection of Rossby wave breaking and its response to shifts of the midlatitude jet with climate change. *J. Geophys. Res.*, **117**, D09117, https://doi.org/10.1029/2012JD017469.

Ding, Q., A. Schweiger, M. L'Heureux, D. S. Battisti, S. Po-Chedley, N. C. Johnson, E. Blanchard-Wrigglesworth, K. Harnos, Q. Zhang, R. Eastman, and E. J. Steig, 2017: Influence of high-latitude atmospheric circulation changes on summertime Arctic sea ice. *Nat. Clim. Change*, **7**, 289–295, https://doi.org/10.1038/nclimate3241.

El Riachy M., 2021: Diagnosing high sinuosity regimes associated with anomalous Greenland ice-melt events using self-organizing maps. M.S. thesis, University at Albany, State University of New York, 110 pp.

Fausto, R. S., D. van As, J. E. Box, W. Colgan, P. L. Lange, and R. H. Mottram, 2016: The implication of nonradiative energy fluxes dominating Greenland ice sheet exceptional ablation area surface melt in 2012. *Geophys. Res. Lett.*, **43**, 2649– 2658, https://doi.org/10.1002/2016GL067720.

Fettweis, X., G. Mabille, M. Erpicum, S. Nicolay, M. van den Broeke, 2011: The 1958–2009 Greenland ice sheet surface melt and the mid-tropospheric atmospheric circulation. *Clim. Dyn.*, **36,** 139–159, https://doi.org/10.1007/s00382-010-0772-8.

——, Hanna, C. Lang, A. Belleflamme, M. Erpicum, and H. Gallée, 2013: *Brief communication* "Important role of the mid-tropospheric atmospheric circulation in the recent surface melt increase over the Greenland ice sheet." *The Cryosphere*, **7,** 241–248, https://doi.org/10.5194/tc-7-241-2013.

Fitzpatrick, A. A. W., A. L. Hubbard, J. E. Box, D. J. Quincey, D. van As, A. P. B. Mikkelsen, S. H. Doyle, C. F. Dow, B. Hasholt, and G. A. Jones, 2014: A decade (2002–2012) of supraglacial lake volume estimates across Russell Glacier, West Greenland. *The Cryosphere.*, **8**, 107–121, https://doi.org/10.5194/tc-8-107-2014.

Hermann, M., L. Papritz, and H. Wernli, 2020: A Lagrangian analysis of the dynamical and thermodynamic drivers of large-scale Greenland melt events during 1979–2017. *Wea. Clim. Dyn.*, **1**, 497–518, https://doi.org/10.5194/wcd-1-191-2020.

Kohonen, T., 1995: Self-Organizing Maps. *The Original Incremental SOM Algorithm*, T. Kohonen., Springer., 106–109.

Liu, C., and E. A. Barnes, 2015: Extreme moisture transport into the Arctic linked to Rossby wave breaking. *J. Geophys. Res. Atmos.*, **120**, 3774 3788, https://doi.org/10.1002/2014JD022796.

Mattingly, K. S., C. A. Ramseyer, J. J. Rosen, T. L. Mote, and R. Muthyala, 2016: Increasing water vapor transport to the Greenland ice sheet revealed using self-organizing maps. *Geophys. Res. Lett.*, **43**, 9250–9258, https://doi.org/10.1002/2016GL070424.

——, T. L. Mote, X. Fettweis, D. van As, K. van Tricht, S. Lhermitte, and R. S. Fausto, 2020: Strong summer atmospheric rivers trigger Greenland ice sheet melt through spatially varying surface energy balance and cloud regimes. *J. Climate*, **33**, 6809–6832, https://doi.org/10.1175/JCLI-D-19-0835.1.

McLeod, J. T., and T. L. Mote, 2015: Assessing the role of precursor cyclones on the formation of extreme Greenland blocking episodes and their impact on summer melting across the Greenland ice sheet. *J. Geophys. Res. Atmos.*, **120**, 12357–12377, https://doi.org/10.1002/2015JD023945.

Mernild, S. H., T. L. Mote, and G. E. Liston, 2011: Greenland ice sheet surface melt extent and trends: 1960–2010. *J. Glaciol.*, **57**, 621–628, https://doi.org/10.3189/002214311797409712.

Mioduszewski, J. R., A. K. Rennermalm, A. Hammann, M. Tedesco, E. U. Noble, J. C. Stroeve, and T. L. Mote, 2016: Atmospheric drivers of Greenland surface melt revealed by self-organizing maps. *J. Geophys. Res. Atmos.*, **121**, 5095–5114, https://doi.org/10.1002/2015JD024550.

Mote, T. L., 1998: Mid-tropospheric circulation and surface melt on the Greenland ice sheet. Part II: Synoptic climatology. *Int. J. Climatol.*, **18**, 131–145, https://doi.org/10.1002/(SICI)1097-0088(199802)18:2<131::AID-JOC228>3.0.CO;2-S.

——, 2007: Greenland surface melt trends 1973–2007: Evidence of a large increase in 2007. *Geophys. Res. Lett.*, **34**, L22507, https://doi.org/10.1029/2007GL031976.

Neff, W., G. Compo, F. M. Ralph, and M. D. Shupe, 2014: Continental heat anomalies and the extreme melting of the Greenland ice surface in 2012 and 1889. *J. Geophys. Res. Atmos.*, **119**, 6520– 6536, https://doi.org/10.1002/2014JD021470.

Overland, J. E., J. A. Francis, E. Hanna, and M. Wang, 2012: The recent shift in early summer Arctic atmospheric circulation. *Geophys. Res. Lett.*, **39**, L19804, https://doi.org/10.1029/2012GL053268.

——, ——, R. Hall, E. Hanna, S.-J. Kim, and T. Vihma, 2015: The melting Arctic and midlatitude weather patterns: Are they connected? *J. Climate*, **28**, 7917–7932, https://doi.org/10.1175/JCLI-D-14-00822.1.

Papritz, L., 2020: Arctic lower tropospheric warm and cold extremes: horizontal and vertical transport, diabatic processes, and linkage to synoptic circulation features. *J. Climate*, **33**, 993–1016, https://doi.org/10.1175/JCLI-D-19-0638.1.

Price, F., S., A. J. Payne, I. M. Howat, B. E. Smith, 2011: Committed sea-level rise for the next century from Greenland ice sheet dynamics during the past decade. *Nat. Acad. of Sciences,* **108,** 8978–8983, https://doi.org/10.1073/pnas.1017313108.

Rignot, E., I. Velicogna, M. R. van den Broeke, A. Monaghan, and J. T. M. Lenaerts, 2011: Acceleration of the contribution of the Greenland and Antarctic ice sheets to sea level rise. *Geophys. Res. Lett.*, **38**, L05503, https://doi.org/10.1029/2011GL046583.

Rivière, G., 2011: A dynamical interpretation of the poleward shift of the jet streams in global warming scenarios. *J. Atmos. Sci.*, **68**, 1253–1272, https://doi.org/10.1175/2011JAS3641.1.

Peters, D., and D. W. Waugh, 1996: Influence of barotropic shear on the poleward advection of upper-tropospheric air. *J. Atmos. Sci.*, **53**, 3013–3031, https://doi.org/10.1175/1520-0469(1996)053<3013:IOBSOT>2.0.CO;2.

Sasgen, I., B. Wouters, A. S. Gardner, M. D. King, M. Tedesco, F. W. Landerer, C. Dahle, H. Save, and X. Fettweis, 2020: Return to rapid ice loss in Greenland and record loss in 2019 detected by the GRACE-FO satellites. *Commun. Earth Environ.*, **1**, https://doi.org/10.1038/s43247-020-0010-1.

Seo, K.-W., D. E. Waliser, C.-K. Lee, B. Tian, T. Scambos, B.-M. Kim, J. H. van Angelen, and M. R. van den Broeke, 2015: Accelerated mass loss from Greenland ice sheet: Links to atmospheric circulation in the North Atlantic. *Global Planet. Change*, **128**, 61–71, https://doi.org/10.1016/j.gloplacha.2015.02.006.

Sprenger, M., and H. Wernli, 2015: The LAGRANTO Lagrangian analysis tool – version 2.0. *Geosci. Model Dev.*, **8**, 2569–2586, https://doi.org/10.5194/gmd-8-2569-2015.

——, G. Fragkoulidis, H. Binder, M. Croci-Maspoli, P. Graf, C. M. Grams, P. Knippertz, E. Madonna, S. Schemm, B. Škerlak, and H. Wernli, 2017: Global climatologies of Eulerian and Lagrangian flow features based on ERA-Interim. *Bull. Amer. Meteor. Soc.*, **98**, 1739–1748, https://doi.org/10.1175/BAMS-D-15-00299.1.

Stohl, A., 1998: Computation, accuracy and applications of trajectories—A review and bibliography. *Atmos. Environ.*, **32**, 947–966, https://doi.org/10.1016/S1352-2310(97)00457-3.

Thorncroft, C. D., B. J. Hoskins, and M. E. McIntyre, 1993: Two paradigms of baroclinic-wave life-cycle behaviour. *Quart. J. Roy. Meteor. Soc.*, **119**, 17–55, https://doi.org/10.1002/qj.49711950903.

van den Broeke, M. R., E. M. Enderlin, I. M. Howat, P. Kuipers Munneke, B. P. Y. Noël, W. J. van de Berg, E. van Meijgaard, and B. Wouters, 2016: On the recent contribution of the Greenland ice sheet to sea level change. *The Cryosphere*, **10**, 1933–1946, https://doi.org/10.5194/tc-10-1933-2016.

Wernli, H., and H. C. Davies, 1997a: A Lagrangian-based analysis of extratropical cyclones. I: The method and some applications. *Quart. J. Roy. Meteor. Soc.*, **123**, 467–489, https://doi.org/10.1002/qj.49712353811.

——, 1997b: A Lagrangian-based analysis of extratropical cyclones. II: A detailed case-study. *Quart. J. Roy. Meteor. Soc.*, **123**, 1677–1706, https://doi.org/10.1002/qj.49712354211.

Zschenderlein, P., S. Pfahl, H. Wernli, and A. H. Fink, 2020: A Lagrangian analysis of upper-tropospheric anticyclones associated with heat waves in Europe. *Wea. Clim. Dynam.*, **1**, 191–206, https://doi.org/10.5194/wcd-1-191-2020.